



ALMA MATER STUDIORUM  
UNIVERSITÀ DI BOLOGNA

DOTTORATO DI RICERCA IN

INGEGNERIA ELETTRONICA, TELECOMUNICAZIONI E  
TECNOLOGIE DELL'INFORMAZIONE

Ciclo 37

**Settore Concorsuale:** 09/F1 – CAMPI ELETTROMAGENTICI

**Settore Scientifico Disciplinare:** ING-INF/02 - CAMPI ELETTROMAGNETICI

ADVANCED ANTENNA SYSTEMS FOR WIRELESS POWER TRANSFER,  
LOCALIZATION AND TRAIN INTEGRITY MONITORING

**Presentata da:** Enrico Fazzini

**Coordinatore Dottorato**

Davide Dardari

**Supervisore**

Diego Masotti

**Co-supervisore**

Alessandra Costanzo

Esame finale anno 2025

# Index

<b>Abstract</b> .....	3
<b>List of acronyms</b> .....	5
<b>Introduction</b> .....	7
<b>1.1 Smart Radiating Architectures for Wireless Power Transfer</b> .....	9
<b>1.2 Advances in Train Integrity and Positioning</b> .....	14
<b>2. Frequency diverse arrays</b> .....	16
<b>2.1 State of art</b> .....	18
<b>2.2 Uniform FDA</b> .....	20
<b>2.3 Directivity improvements for FDAs</b> .....	24
<b>2.4 Time controlled frequency diverse arrays</b> .....	36
<b>2.5 Multi-spot WPT via TCFDA</b> .....	53
<b>3. Time modulated arrays</b> .....	61
<b>3.1 State of art</b> .....	61
<b>3.2 Optimum Feeding Strategy for Agile Wireless Powering by Large, High-Directivity TMAs</b> .....	63
<b>3.3 Agile Target Localization Via Time-modulation</b> .....	68
<b>4. Railway Signaling and Positioning System</b> .....	80
<b>3.4 Introduction</b> .....	80
<b>4.2 An Innovative Multi-Port LoRa-Based Wireless Node for Railway Signaling and Positioning</b> .....	82
<b>Conclusion</b> .....	100
<b>References</b> .....	103

# Abstract

This thesis explores two distinct yet complementary research areas: Wireless Power Transfer (WPT) antenna systems and compact antenna solutions for Train Integrity Monitoring.

The primary focus is on WPT, a transformative technology enabling the efficient wireless transmission of power. This work investigates two radiating architectures, Frequency Diverse Arrays (FDAs) and Time-Modulated Arrays (TMAs), that are highly reconfigurable in real time, offering enhanced power transfer performance with reduced costs.

FDAs, traditionally used in radar due to their intrinsic scanning capabilities, are applied here for WPT for the first time. The radiation properties have been analysed and for the first time practical solutions have been proposed, trying to adapt the system for powering application. A novel scheme, Time-Controlled Frequency Diverse Arrays (TCFDAs), addresses FDA limitations by delivering precise power transmission to desired locations, outperforming conventional Phased Arrays (PAs) in medium- and high-power ranges, electing itself as one of the most interesting solution able to replace modern and expensive architectures with its multi-beam and highly reconfigurable radiation properties.

TMAs, first explored in the 1960s, offer dynamic control over the radiation pattern using time-varying signals. While previous studies primarily focus on theoretical optimizations, this thesis addresses practical challenges in TMA design, proposing innovative 2D solutions with circular symmetry for highly directive, reconfigurable power transfer and localization applications.

As a side activity, research on compact antenna systems for Train Integrity with the goal of providing a practical and efficient solution for co-locating multiple antennas without sacrificing performance is proposed. This work presents the design and validation of a compact wireless system with three co-located antennas operating in the 2.4 GHz band, intended for positioning purposes on

secondary railway lines where the European Railway Traffic Management System (ERTMS) is unavailable. Using LoRa technology, the system enables low-power, long-range communication with acceptable latency.

This work provides significant contributions to the fields of WPT and antenna system design, with applications in both wireless power transfer and railway safety.

# List of acronyms

Abbreviation	Explanation
WPT	Wireless Power Transfer
ICT	Information and Communication Technologies
IoT	Internet of Things
EH	Energy Harvesting
FF-WPT	Far-field Wireless Power Transfer
NF-WPT	Near-field Wireless Power Transfer
RF	Radiofrequency
mm-wave	Millimeter-wave
PAs	Phased Arrays
RAs	Retrodirective Arrays
RFID	Radiofrequency Identification
LWAs	Leaky Wave Arrays
TMA	Time Modulated Arrays
FDA	Frequency Diverse Arrays
SDR	Software Defined Radio
TC-FDA	Time-Controlled Frequency Diverse Arrays
CW	Continuous Wave
SINR	Signal-to-Interference-plus-Noise Ration
AF	Array Factor
BP	Beam Pattern
HPBW	Half Power Beam Width
CCFDA	Circular Concentric Frequency Diverse Arrays
RFDA	Radial Frequency Diverse Arrays
RECTENNA	Rectifying Antenna
PAPR	Peak-to-Average Power Ratio
WuR	Wake-up Radio

VAS	Variable Aperture Size
BOTS	Binary Optimized Time Sequences
PS	Pulse Shifting
SOTS	Sub-Sectional Optimized Time Steps
ERTMS	European Rail Traffic Management System
GNSS	Global Navigation Satellite System
RTK	Real-Time Kinematic
LoRa	Long Range
ISM	Industrial, Scientific and Medical band
SNR	Signal-to-Noise Ratio
RSSI	Received Signal Strength Indicator
PER	Packet Error Rate
BER	Bit error Rate

# Introduction

This chapter is based on the following publications:

*A. Costanzo, D. Masotti and E. Fazzini, "RF/microwave energy-autonomous systems," 2022 International Workshop on Antenna Technology (iWAT), Dublin, Ireland, 2022, pp. 142-145. © 2022 IEEE*

*V. Palazzi et al., "Radiative Wireless Power Transfer: Where We Are and Where We Want to Go," in IEEE Microwave Magazine, vol. 24, no. 2, pp. 57-79, Feb. 2023. © 2023 IEEE*

*G. Paolini, E. Fazzini, S. Trovarello, D. Amato, D. Masotti and A. Costanzo, "A 2.4 GHz Modular Antenna System for Train Integrity and Localization Purposes," 2023 IEEE 13th International Conference on RFID Technology and Applications (RFID-TA), Aveiro, Portugal, 2023, pp. 221-224. © 2023 IEEE*

The evolution of advanced technologies in the field of telecommunications and wireless energy transmission has led to a growing interest in the development of innovative, high-performance antenna systems. This thesis focuses on two distinct yet complementary areas of research: on the one hand, the study of antenna systems for Wireless Power Transfer (WPT), and on the other, the design of compact solutions for the co-location of antennas intended for Train Integrity monitoring applications.

In the first area, which was the primary focus of this PhD research, WPT represents a technology with the potential to revolutionize various sectors by enabling the efficient transmission of power without the need for cables. This research focuses on the design of advanced antenna systems to optimize transfer efficiency and overall performance, while minimizing power losses. Specifically, this work investigates two radiating architecture, Frequency Diverse Arrays (FDAs) and Time-Modulated Arrays (TMAs), which are highly reconfigurable in real time, offering excellent power transfer performance while keeping equipment costs low by directing energy only where it is needed.

FDAs, the more recent of the two, have demonstrated remarkable capabilities in radar applications due to their intrinsic scanning abilities. Building on the state of the art, this research aims to extend the application of FDAs to WPT systems, addressing their limitations in focusing power on specific target locations. Based on the conducted analysis, in the author's opinion, these limitations have been successfully overcome. The proposed solution, Time-Controlled Frequency Diverse Arrays (TCFDAs), offers an efficient, reconfigurable, and low-cost approach to precisely transmit power to desired locations. The system also supports almost simultaneous multi-beam capabilities and utilizes simple and affordable hardware. In terms of rectified power, the TCFDA outperforms traditional systems such as Phased Arrays (PAs), particularly in the medium- and high-power ranges.

TMAAs, on the other hand, represent a radiating technology investigated from 1960, that leverage time-varying signals to control and shape the radiation pattern of the array. This approach allows for dynamic control over the distribution of radiated energy, enabling features such as sidelobe suppression, beam scanning, and improved efficiency. TMAAs are particularly attractive for applications requiring flexible, real-time reconfigurability, and can be implemented with relatively simple hardware. The use of TMAAs for WPT applications has not been fully explored, as most of the existing literature focuses on various optimization algorithms designed to determine the best control sequence for enabling multi-beam operations or sidelobe suppression, particularly in simple array configurations. This work aims to address this gap by focusing on the practical challenges of TMA design and developing realizable and innovative 2D solutions. A novel and efficient approach has been discovered using a circular symmetry organized in a radial geometry, offering a highly directive and reconfigurable architecture for directive power transfer applications. Additionally, this same topology has been investigated for localization purposes, demonstrating advanced scanning capabilities with lower hardware costs compared to modern systems.

In the second area, research on innovative solutions for the co-location of multiple antennas in constrained spaces, which is critical for applications like train integrity monitoring, has been provided. These systems require the integration of multiple antennas without compromising performance, while ensuring signal reliability and system



compactness. A practical and efficient solution has been developed, proposing a compact wireless system to be installed for positioning purposes in secondary railways exploiting LoRa protocol, offering a solution for tracks where the modern systems are not available.

## ***1.1 Smart Radiating Architectures for Wireless Power Transfer***

The human being finds himself invested by the new revolution scenario where the technology is such pervasive that, soon, he will experience billions of devices interconnected one to each other. This increasing demand has moved the attention of companies and researchers to an important aspect: the energization of these devices. With millions of sensors distributed all over the space, it is unthinkable having a battery for each of them, most of all for practical impairments, as its replacement. In this scenario, particular interest is given to wireless power transfer (WPT) technologies, due to the necessity to charge these devices considering the gradual disappearing of wires, for obvious reasons. Consequently, WPT became a leading technology such that several information and communication technologies (ICT) companies have moved their interest on it.

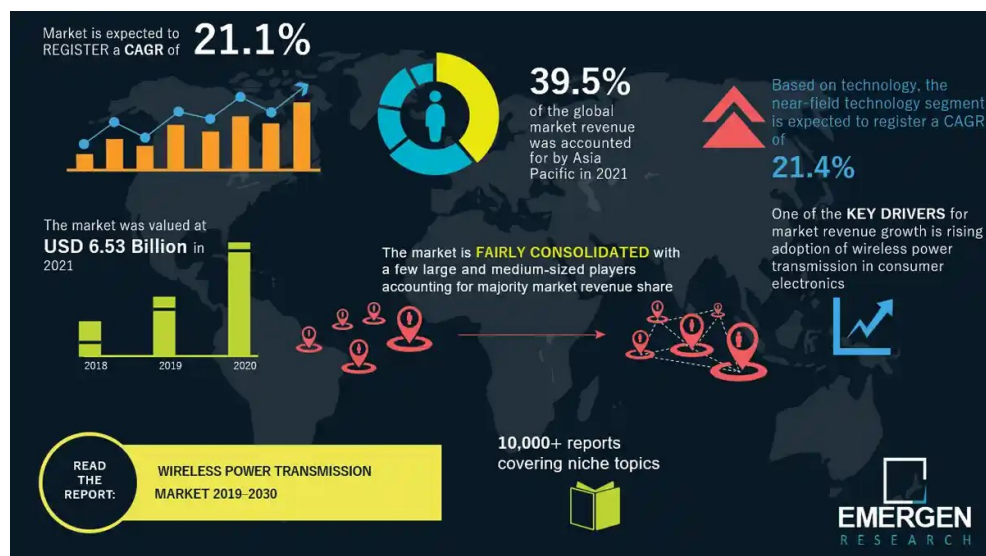


Fig. 1. Wireless Power Transfer market overview [1]

Consequently, in the last years, the WPT market has witnessed substantial growth, as illustrated in Fig. 1, and the trend shows an increasing behaviour for the current decade. The key drivers include the increasing popularity of electric vehicles, Industry 4.0 initiatives, and advancements in resonant inductive coupling technologies.

There is an increasing need of wireless systems combining antennas, low-power circuits and energy harvesting capabilities, for the effective exploitation of the internet of things (IoT) paradigm [2]. Various application scenarios are foreseen, such as industrial plants, e-health, crowd monitoring, smart ambient. These scenarios are generally characterized by harsh EM conditions demanding for many challenges to be overcome, from networking solutions, to the connection of many devices, to energy sustainability of each individual system with no need for maintenance (e.g., batteries replacement). Energy harvesting (EH) or scavenging approaches [3] have been demonstrated valid options for ultra-low power applications, where the frequencies, power density, polarization, and direction of incident waves are unknown and may be highly variable in terms of power density availability. A more deterministic approach is currently considered based on the deployment of smart energy transmission spots in environments pervaded by battery-less sensors, to ensure a more systematic and reliable operation of remotely charged battery-less devices [4]. Such systems are required to be compact, low-cost, low profile, and to operate with the lowest possible energy requirements.

In [5] the most promising approaches to comply with this kind of design needs, for both transmitters and receivers, are analysed and a systematic approach to compute the most relevant figures of merit are provided.

In this thesis work the attention will be devoted to the far-field wireless power transfer (FF-WPT) applications where the power is exchanged by radiative electromagnetic far-field between radiating elements: differently from the near-field wireless power transfer (NF-WPT), it allows to cover long-distance links and typically involves low levels of power in the radiofrequency (RF) spectrum. The main building blocks and the total efficiency of FF-WPT link is presented in Fig. 2

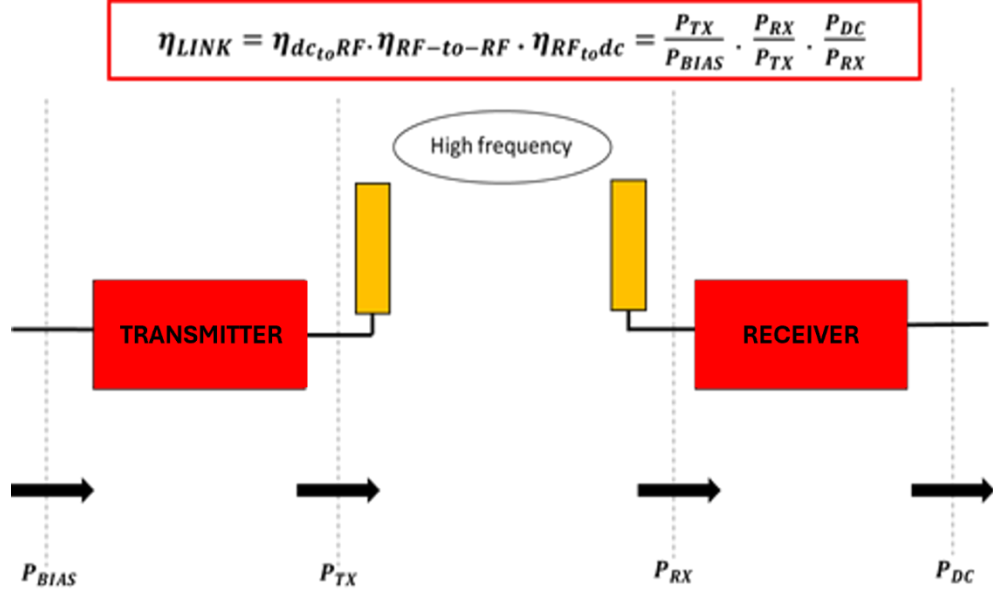


Fig. 2. Block scheme and efficiency factors of a far-field WPT link

In the recent years, many research efforts have been made to make the FF-WPT a feasible application. The research activity has followed three main directions to maximize the overall wireless link efficiency  $\eta_{LINK}$ :

- I. the optimization of the power amplifier efficiency ( $\eta_{dc \rightarrow to \rightarrow RF}$ ) on the transmitter side
- II. the optimization of the receiving rectifying antenna (or rectenna) efficiency ( $\eta_{RF \rightarrow to \rightarrow dc}$ )
- III. the study of smart transmitting architectures for the maximization of the link efficiency ( $\eta_{RF \rightarrow to \rightarrow RF}$ ).

As regards the first two research directions, it can be stated that results very close to the optimum have been already achieved: over 80% drain efficiency amplifiers are available in the microwave range [6],[7], as well as highly efficient rectennas (with  $\eta_{RF \rightarrow to \rightarrow dc} > 60\%$ ) working in the -10 dBm ÷ 10 dBm RF available power range, typical of WPT applications, can be considered a reality [8],[9]. A great deal of activity has been also devoted to the third branch, but this can be considered the main bottleneck in FF-WPT: despite the high radiation efficiency of the involved antennas, a few amount of the transmitted power actually reaches the receiver location and this causes the drop of the overall system performance, not only because the attenuation makes the power rapidly decrease after few meters, especially in the

millimeter-wave (mm-wave) spectrum, but mostly because the power captured by the receiver is a small fraction of the available one and because in-between obstacles can impact on the overall transfer. It needs to be stated that the exploitation of WPT technologies will be a reality only if transmitting systems will reach an elevated level of reconfiguration in real-time together with the more demanding power focusing capability.

A possible solution can be identified by the so-called ‘smart RF showers’, i.e., illuminators able to satisfy such requirements. They must share the capability of selecting the best available channel to reach the target, having a simple and cheap feeding network and sending the energy only where it is needed. A collection of the main architectures is presented in Fig. 3, where the comparison among different features is highlighted.



















	RECONFIGURABILITY	EASE OF DESIGN	BEAM-STEERING
PHASED-ARRAYs			
RETRODIRECTIVE ARRAYs			
LEAKY-WAVE ARRAYs			
TIME-MODULATED ARRAYs			
FREQUENCY-DIVERSE ARRAYs			
TIME-CONTROLLED FREQUENCY DIVERSE ARRAYs			

Fig. 3. Smart RF showers

Phased arrays (PAs) represent a computer-controlled array of antennas that creates a beam of radio waves that can be electronically steered to point in different directions without moving the radiating elements [10], resulting particularly efficient in modern systems for localization [11] and communication purposes [12]. They make use of phase-shifters to obtain their beam-steering capability that results in extremely expensive devices that drastically increase the cost of the entire transmitter and require a delicate calibration procedure. Despite the great advantages in terms of performance, their expensive hardware makes this solution unfeasible for low-cost powering applications, forcing them to investigate new revolutionary designs.

Retrodirective arrays (RAs) are passive radiating architectures able to reflect the incoming signal towards the arrival direction, finding implementation in radio frequency identification (RFID) applications [13]. They are limited in terms of beam-steering and don't offer reconfigurability features, resulting in unfeasible real-time and adaptive solutions.

Leaky wave arrays (LWAs) use a guiding structure that allows electromagnetic radiation to "leak" some of its energy along the structure, creating a radiating wave that propagates outward [14]. LWAs can be designed to radiate in specific directions by changing the signal frequency (thus with a limited reconfigurability) and can be constructed with relatively simple structures, but suffer from the efficiency point of view.

Time modulated arrays (TMAs) are smart radiating architectures able to profitably exploit the harmonic contributions generated by the modulation of the input signal, entering each radiating element, through a lower frequency user-defined pulse [15]. They offer unparalleled features in terms of beam-steering with respect to PAs because of the multi-harmonic radiation, and also involve a cheaper hardware, implementing low-cost switches instead of expensive phase-shifters. Controlling the parameters of the pulsed waveform a highly reconfigurability of the radiation is obtained, highlighting the TMAs as one of the best candidates as smart transmitters for powering application. On the other hand, given the pulsed and multi-harmonic nature of the radiation, TMAs shows a disadvantage in terms of efficiency.

Frequency diverse arrays (FDAs) are smart radiating architecture in which each element radiates a frequency that is slightly different with respect to the one radiated by the neighbors [16]. The intermodulation between different tones can create a range-angle-time dependent radiation, which can be profitably exploited for radar applications [17],[18], with a highly reconfigurable behavior by setting the frequency spacing among the elements. The required hardware to manage the multi-frequency excitation represents the main drawback in terms of complexity and cost, since it will exploit different oscillators that must share a common clock signal. In this sense, software defined radio (SDR) technologies become fundamental to handle the complex signal generation system.

Time-controlled frequency diverse arrays (TCFDAs) have been one of the contributions of the research activity described in this thesis work and represent the evolution of standard

FDAs for which the principle of time modulation (the same applied for TMAs) is applied for obtaining beam-steering, the most significant limit offered by the standard FDA solution. By controlling each radiating signal with a pulsed waveform, the system can radiate in predefined directions that can be controlled in real-time, offering a highly reconfigurable transmission system.

This work will focus on the last three configurations, investigating the FDAs/ TCFDAs and novel TMA architectures in chapter 2 and 3, respectively. This investigation will provide the mathematical basis able to describe in detail the peculiar characteristics of their radiation and their exploitation for WPT applications.

## ***1.2 Advances in Train Integrity and Positioning***

In recent years, the topics of train integrity and positioning have attracted much attention in the global transport industry, as there is an ever-increasing need for more efficient, safer, and reliable railway systems. One of the major initiatives in this respect is the European Rail Traffic Management System (ERTMS), which has become the standardized framework that has emerged for railway signaling across Europe. ERTMS is a highly advanced system to increase interoperability between European countries, enabling a high degree of safety and the possibility of increasing the capacity and speed of services. Within the ERTMS framework, Level 3 is particularly notable because it requires all trains to continuously monitor their own status and integrity in real time [19]. This monitoring ensures that the trains will be able to transmit critical data regarding positioning and operational integrity with reliability, without having to depend on fixed-trackside infrastructure, like the traditional systems of signaling.

To meet these stringent requirements, a variety of advanced technologies have been developed and implemented over the past few years. One such innovation is the Global Navigation Satellite System (GNSS), a satellite-based technology that allows for precise geolocation of moving objects, including trains. GNSS has been particularly useful in railway applications with respect to the detection of virtual balises, i.e. electronic markers, along the railway lines. Contrary to physical ones, these virtual counterparts send signals to the train

via satellites, and this represents a far more flexible and cost-effective solution. GNSS systems work in coordination with onboard kinematic sensors that monitor critical data related to train speed, acceleration, and orientation. This kind of satellite communication, including real-time sensor data, forms a basis for an accurate and seamless flow of information to help improve control and management of rail operations [20].

Moreover, as the demand for higher precision in train localization grows, especially in densely populated areas and high-speed rail corridors, additional technologies are being integrated to supplement GNSS. The technology proposed is LoRa, a wireless communication system for low-power, long-range signals. The LoRa solution will be particularly suitable for railway applications since it will enable reliable data delivery with very low energy consumption over very long distances. This is quite crucial for train systems that must be in constant communication with various devices and several infrastructures along the route. LoRa can also support integration with Real-Time Kinematic (RTK) positioning systems that let it broadcast RTK messages across a network of connected devices such as base stations or control centers to improve the accuracy of train localization. RTK technology uses satellite signals in addition to ground-based reference stations and can achieve centimeter-level accuracy; thus, it is very suitable for critical applications where even slight deviations in positioning could lead to safety risks or inefficiencies [21].

In summary, the increasing focus on train integrity and localization within the transport industry is driving the adoption of advanced technologies such as GNSS, kinematic sensors, LoRa, and RTK. These systems are helping railways meet the demands of modern train management systems, where continuous, reliable, and self-sustained monitoring of train integrity and positioning is essential. As the rail industry continues to evolve, these technologies will play a key role in ensuring safer, more efficient, and more sustainable train operations across Europe and beyond.

In this work, in chapter 4, the design of an original, compact wireless system to be installed for positioning purposes in secondary railways exploiting LoRa protocol will be provided, offering a solution for tracks where the ERTMS is not available.

## 2. Frequency diverse arrays

This chapter is based on the following publications:

*E. Fazzini, M. Shanawani, A. Costanzo and D. Masotti, "Focusing RF-on demand by Logarithmic Frequency-Diverse Arrays," 2020 IEEE Wireless Power Transfer Conference (WPTC), Seoul, Korea (South), 2020, pp. 76-79. © 2020, IEEE*

*E. Fazzini, M. Shanawani, A. Costanzo and D. Masotti, "A Logarithmic Frequency-Diverse Array System for Precise Wireless Power Transfer," 2020 50th European Microwave Conference (EuMC), Utrecht, Netherlands, 2021, pp. 646-649. © 2020, EuMA*

*E. Fazzini, A. Costanzo and D. Masotti, "Ranging On-Demand Microwave Power Transfer in Real-Time," in IEEE Microwave and Wireless Components Letters, vol. 31, no. 6, pp. 791-793, June 2021. © 2021, IEEE*

*E. Fazzini, A. Costanzo and D. Masotti, "Range Selective Power Focusing with Time-controlled Bi-dimensional Frequency Diverse Arrays," 2021 IEEE Wireless Power Transfer Conference (WPTC), San Diego, CA, USA, 2021, pp. 1-4. © 2021, IEEE*

*D. Masotti, E. Fazzini and A. Costanzo, "On the Use of Frequency-diversity for Efficient Wireless Power Transmission," 2021 XXXIVth General Assembly and Scientific Symposium of the International Union of Radio Science (URSI GASS), Rome, Italy, 2021, pp. 1-3. © 2021, IEEE*

*E. Fazzini, A. B. Gok, A. Costanzo and D. Masotti, "Accurate Ranging Exploiting a 32-patch Frequency Diverse Array with Circular Symmetry," 2022 16th European Conference on Antennas and Propagation (EuCAP), Madrid, Spain, 2022, pp. 1-5. © 2022, EurAAP.*



*E. Fazzini, A. Costanzo and D. Masotti, "Wireless Power Transfer Procedure via Hybrid Frequency Diversity," 2021 51st European Microwave Conference (EuMC), London, United Kingdom, 2022, pp. 757-760. © 2022, EuMA*

*E. Fazzini, A. Costanzo and D. Masotti, "Ad-hoc WPT Exploiting Multi-sine Excitation of Linear Frequency Diverse Arrays," 2022 Wireless Power Week (WPW), Bordeaux, France, 2022, pp. 563-566. © 2022, IEEE*

*E. Fazzini, A. Costanzo and D. Masotti, "A New Wheel-Spoke Transmitter for Efficient WPT Based on Frequency Diversity," 2022 52nd European Microwave Conference (EuMC), Milan, Italy, 2022, pp. 576-579. © 2022, EuMA*

*E. Fazzini, T. Tiberi, A. Costanzo and D. Masotti, "Advanced Reconfigurability of Frequency-diverse Radiators for both Localization and Powering," 2023 17th European Conference on Antennas and Propagation (EuCAP), Florence, Italy, 2023, pp. 1-4. © 2023, EurAAP*

*T. Tiberi, E. Fazzini, A. Costanzo and D. Masotti, "Realistic Performance Analysis of Frequency-Diverse Arrays Radiation," 2023 IEEE 13th International Conference on RFID Technology and Applications (RFID-TA), Aveiro, Portugal, 2023, pp. 217-220. © 2023, IEEE*

*E. Fazzini, T. Tiberi, L. Bastia, A. Costanzo and D. Masotti, "Simplified Frequency-Diverse Array Architecture for Surveillance Purposes," 2024 18th European Conference on Antennas and Propagation (EuCAP), Glasgow, United Kingdom, 2024, pp. 1-5. © 2024, EurAAP*

*T. Tiberi, E. Fazzini, A. Costanzo and D. Masotti, "Exploitation of Harmonic Generation in Time-Controlled Frequency-Diverse Arrays for WPT," in IEEE Transactions on Antennas and Propagation, vol. 72, no. 1, pp. 497-505, Jan. 2024. © 2024, IEEE.*

## **2.1 State of art**

In a traditional PA composed of ideal isotropic radiators, all the waveforms radiated from each of the radiating elements are identical. If all radiated signals are continuous wave (CW) signals with identical phase, the array beam will point in broadside direction; by controlling the phase of each radiator (usually implementing phase shifters) beam-steering capability can be obtained. The signals that impinge on a far-field target with a certain angle of incidence will be identical, except for a phase shift due to a path length difference for each element, and the phase difference between the elements results only function of angular coordinate. If the CW signal radiated by a single element presents a frequency that is slightly different with respect to the frequency of the neighbours, the phase difference between adjacent elements presents a range dependency, in addition to the angle one [22]. The presence of this new term shows that the scan angle of the antenna now depends on range. This range-dependent quality suggests that, differently from the case of PAs, the beam changes direction as the distance from the transmitter changes. The exploitation of such diversity technique leads to FDAs, firstly introduced in [16]. This array concept can provide more flexible beam scan options, as well as serve to mitigate the effects of multipath interference, and results particularly feasible for radar applications. The FDA's pattern can be used to suppress range ambiguous clutter and improve detection performance [23], to reject the range-dependent interferences [24] and to increase the received signal-to-interference-plus-noise ratio (SINR) consequently. After these first characterizations, in [25] the range-time-angle periodicity of the FDAs radiation has been analysed, revealing that the peculiar characteristic of having many different range-angle pairs where the field reaches its maximum happens for a fixed time instant, therefore resulting an instantaneous property. Observing the radiation in time, it has been provided that the array beam rotates and scans all angles periodically, with a periodicity function of the frequency offset. In this way, each point of the space is invested by the maximum of the FDA's radiation. This unique property provides an

auto-scanning feature [26], but at the same time due to this multiple-maxima of the radiation, several potential interferers, located at any of the maxima, can come into the radar scene and deteriorate the resulting signal-to-noise ratio (SINR).

A possible solution to the multiple-maxima presence problem has been identified in the definition of a more directive radiation that, instead of periodically scanning all angles in time, can confine its action in a specified set of angles. Configurations based on the manipulation of either the frequency offset or the array topology have been proposed. For the first case, exploiting logarithmic increasing frequency offset [27] a nonperiodic beam pattern can be obtained, with a maximum that can be steered in space by selecting appropriate excitation weights of the antennas. A step forward is provided in [28] where a symmetrical FDA beam pattern synthesis approach using multicarrier frequency increments and convex optimization to generate dot-shaped range-angle beam pattern is provided: this solution significantly outperforms the existing previous configuration in decoupling the range-angle beam pattern for radiation focusing. In the second case, solutions for improving the directivity of the radiating system have been proposed restoring planar topologies, involving rectangular [29] or circular geometries [30]. Finally, another interesting solution for radar applications is represented by the pulsed-FDA [31], where for the first-time pulsed signals are used as FDAs inputs for obtaining a quasi-static characteristic able to scan predefined space sectors.

Researchers have investigated on other possible applications where the FDAs can be exploited, identifying WPT as one of the most promising among them. Given the range focusing ability, this technology can be effectively applied for energizing battery-less devices increasing the wireless link efficiency, sending the power only where it is needed. Possible implementations have been presented in [32],[33], where a highly efficient solutions based on nonlinear frequency offsets and time-modulated weights across the array elements allow to focus the transmitted power in a specific angular-range sector (i.e., target area). In [34], the Laboratory of Campi Elettromagnetici of the University of Bologna, the author's research group, has presented an additional study on FDA's radiation, offering a more rigorous analysis of the radiation properties for WPT applications. Based on the literature, FDAs represent an intriguing architecture for powering applications, but they required a deep analysis in terms of ranging, beam-steering and time-dependent properties. To develop a

solution suitable for smart energization, it is necessary to address the limitations and open challenges associated with FDAs. There is currently no efficient, low-cost method to focus power on a specific region of space, nor has an ideal configuration been identified in terms of power transfer performance, including the generation system and radiating topology. This chapter aims to bridge this gap by reviewing the solutions proposed so far and introducing new approaches, ultimately presenting a system that stands as one of the most promising for WPT applications from a practical perspective.

## 2.2 Uniform FDA

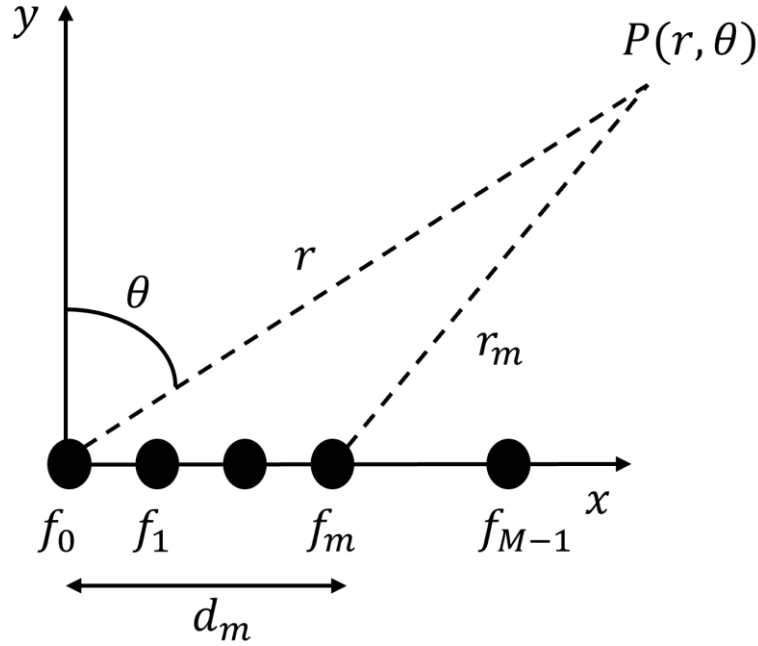


Fig. 4. Linear frequency diverse array.

Let's consider a linear array composed of  $M$  isotropic radiators aligned along the  $x$ -axis, as depicted in Fig. 4. Each element, at a distance  $d_m$  from the origin, radiates a CW signal at frequency  $f_m$  and is at a distance  $r_m$  from the generic far-field point, represented for simplicity by the point  $P(r, \theta)$  on the scanning plane  $(r, \theta)$ . The reference frequency is defined as  $f_0 = \frac{c}{\lambda}$ , where  $c$  is the speed of light and  $\lambda$  is the wavelength in vacuum.

The signal radiated in far-field by the  $m - th$  element can be cast in the following form:

$$x_m(t) = \text{real}\{A_m e^{j2\pi f_m t}\} \quad \text{with } m = 0, \dots, M - 1 \quad (1)$$

where  $\text{real}\{\}$  stands for real part operator,  $A_m$  is the complex weight of the  $m - th$  element. In the standard configuration of FDAs [16], a linear increasing frequency offset ( $f_m = f_0 + m\Delta f$ , with  $f_0 \gg \Delta f$ ) and a uniform element distribution ( $d_m = md_0$ ) are considered. Restoring the far-field approximation ( $r_m = r - md_0 \sin(\theta)$ , with  $d_0 = \frac{\lambda}{2}$ ), the total signal transmitted in  $P(r, \theta)$  can be computed as the sum of all the radiated signals and can be written as:

$$x(r, \theta, t) = e^{j2\pi f_0(t - \frac{r}{c})} \sum_{m=0}^{M-1} A_m e^{j2\pi f_0(\frac{md_0 \sin(\theta)}{c})} e^{j2\pi(m\Delta f)(t - \frac{r}{c})} \quad (2)$$

As can be stated from equation (2), the introduction of the frequency diversity allows to obtain a transmitted signal function of the range ( $r$ ), the elevation angle ( $\theta$ ) and time ( $t$ ). In this first analysis, for the sake of simplicity, the complex weights  $A_m$  will be considered unitary and their role will be specified later.

Simulations of the normalized beam pattern ( $BP = |x|^2$ ) are presented in Fig. 5, considering  $f_0 = 2.45 \text{ GHz}$ ,  $M = 8$  and  $\Delta f = 5 \text{ MHz}$ .

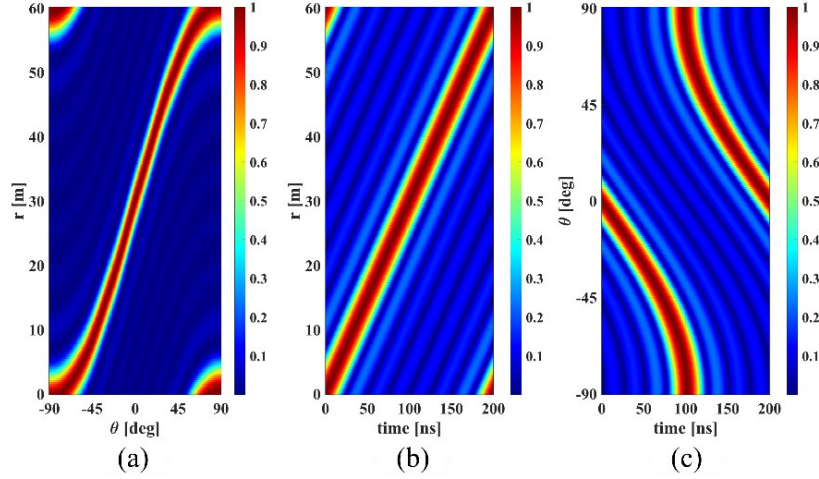


Fig. 5. BP of a uniform FDA with linear increasing frequency offset as a function of: (a) range-elevation for  $t = 100 \text{ ns}$ , (b) range-time for  $\theta = 0^\circ$  and (c) angle-time for  $r = 0 \text{ m}$ .

Given the dependency on three variables, the radiation should be analyzed considering each pair of them to deeply understand its nature and properties. In Fig. 5(a) the time has been fixed to  $100 \text{ ns}$ . It can be noted that, differently from PAs, different pairs  $(r, \theta)$  receive the maximum of radiation describing the so-called ‘S-shape’. In principle, a ranging capability is retrieved allowing to distribute the power at certain distances from the source. In Fig. 5(b) the time evolution of the broadside radiation ( $\theta = 0^\circ$ ) is observed. This analysis suggests that the distribution of the power in each  $(r, \theta)$  pairs is purely instantaneous and each point of the S-shape radially moves far away from the source passing the time. Finally, in Fig. 5(c) the time evolution of the power received at a given distance from the source ( $r = 0 \text{ m}$ ) is considered, suggesting that, as the time elapses, every angle is invested by the radiation. This effect provides the system with an auto-scanning property: this is the reason why FDAs can be profitably exploited for localization purposes.

An important analysis for correctly defining the properties of the radiation is related to its periodicity [25]. By fixing two of the three variables, it is possible to recognize a periodic behavior with respect to range, time and angle, as shown in Fig. 6.

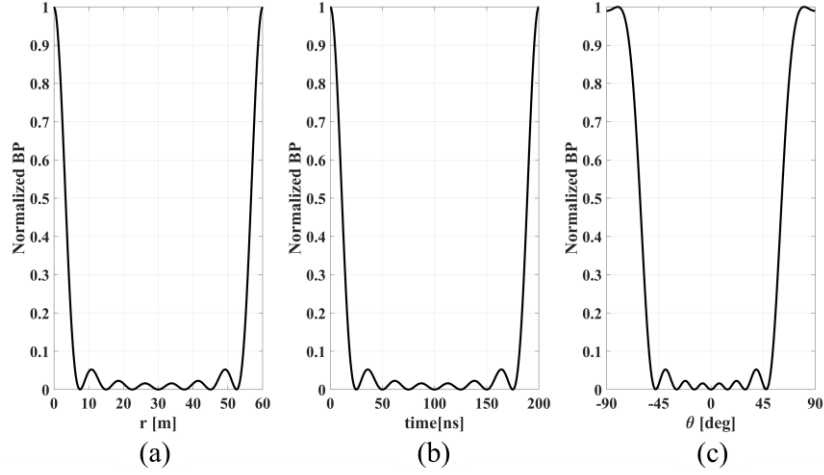


Fig. 6. BP of uniform FDA with linear increasing frequency offset as function of: (a) range for  $\theta = 0^\circ$ ,  $t = 100 \text{ ns}$ , (b) time for  $\theta = 0^\circ$ ,  $r = 0 \text{ m}$  and (c) angle for  $r = 30 \text{ m}$ ,  $t = 0 \text{ s}$ .

From Fig. 6(a), the BP as a function of range for  $\theta = 0^\circ$ ,  $t = 100 \text{ ns}$  provides a spatial periodicity of  $\frac{c}{\Delta f}$ . Fig. 6(b) shows that a specific location in the  $(r, \theta)$  space is periodically illuminated every  $\frac{1}{\Delta f}$ , indicating a single maximum point for each instant of time. Finally, an angle periodicity of  $\pi$  is highlighted in Fig. 6(c).

An interesting aspect is related to the choice of the  $\Delta f$  value: it is evident how this influences the range of applications. If values in the  $\text{kHz}$  range are chosen, the maximum distance that can be reached in one scanning period is in the  $\text{km}$  range and the system can be profitably exploited for localization purposes. Increasing these values in the  $\text{MHz}$  range, the maximum distance results reduced to hundreds of meters (as visible in Fig. 5(a) and Fig. 6(a)) and the FDAs can be used for other applications, such as WPT as proposed in the literature for the first time by the author's research group in [34].

From the characterization of the FDA's radiation, it is evident the reason why these have been exploited for radar applications, i.e., the auto-scanning feature. In fact, in one period  $\frac{1}{\Delta f}$  the system can scan all angles at certain distance from the source and all distances in a certain direction, without involving complex and expensive phase-shifters or mechanically rotating the antenna. On the contrary, if FDAs are implied for WPT applications, the infinite number of couples  $(r, \theta)$  where the power is instantaneously sent, and the time evolution of the beam

makes the system unfeasible for precise powering. In fact, the power is transmitted in multiple locations due to the ‘S-shape’ and is not fixed as the time passes. In the last decades researchers have investigated the possibility to improve the directivity of the system to exploit the system for WPT by identifying several methods based on the frequency distribution rule and the topology of the transmitter. Compared to the solutions already presented in the literature, which have mostly been explored from a theoretical standpoint, this thesis work provides the first in-depth analysis of the design of these radiating structures, offering a comprehensive and practical guide for the use of FDAs in both power transfer and localization applications.

## 2.3 *Directivity improvements for FDAs*

Working on the frequency distribution rule for uniformly spaced FDAs or on the topology of transmitter restoring planar bidimensional architectures are methods used to improve the directivity of the FDA’s radiation,

In the first case, an example is provided in [27] where a logarithmic increasing frequency offset is applied to a uniformly spaced linear array. In this way the frequency  $f_m$  of the  $m - th$  element can be expressed as:

$$f_m = f_0 + \Delta f \log(m + 1) \quad (3)$$

Simulations of the BP with  $M = 8$ ,  $f_0 = 2.45 \text{ GHz}$  and  $\Delta f = 20 \text{ MHz}$  are provided in Fig. 7.



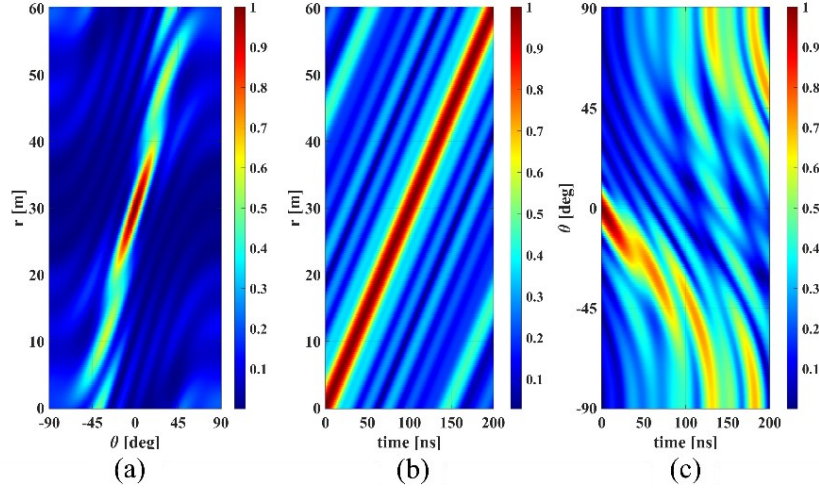


Fig. 7. BP of uniform FDA with logarithmic increasing frequency offset as function of: (a) range-elevation for  $t = 100 \text{ ns}$ , (b) range-time for  $\theta = 0^\circ$  and (c) angle-time for  $r = 0 \text{ m}$ .

As can be seen from Fig. 7(a), the ‘S-shape’ has been replaced by a more confined spot that can be profitably exploited for powering applications, just exploiting logarithmic increasing frequency offset. Additionally, the choice of a different offset for consecutive elements reduces drastically the time periodicity of the range and the angle, since it is function of the greatest common factor between all the excited frequencies. In this case, the periodic appearance of the power in a  $(r, \theta)$  spot is almost eliminated. In this context, the role of the complex weight  $A_m$  becomes crucial to steer the maximum in a predefined  $(r_t, \theta_t)$  spot for  $t = 0 \text{ s}$ , following the expression:

$$A_m = e^{j2\pi\left\{\frac{\log(m+1)\Delta f r_t}{c} - \frac{f_0 m d \sin\theta_t}{c}\right\}} \quad (4)$$

but the adoption of a complex feeding strategy (acting on the radiating elements phase, as for PAs) is needed.

The logarithmic relationship is not the only one that can improve the directivity. Other methods have been investigated in literature, in particular the use of optimization algorithms as [35],[36] to define the optimized offsets to further reduce the instantaneous covered region. Despite the advantages in terms of focusing provided by these configurations, the main limit is given by the complex excitation circuit required, i.e. the creation of specific tones at specific

frequencies. Additionally, if phase-shifters are not implied it is impossible to steer the maximum in other direction different from the broadside one, increasing the cost of entire system.

Without modifying the frequency distribution rule and maintaining the linear increasing frequency offset for simplicity in terms of hardware complexity, a possible solution could be resorting to bi-dimensional topologies. If such a structure is adopted, the 2D characteristic of the FDA's radiation needs to be considered, inserting the azimuthal variable in the equation (2). Two different architectures have been analyzed from the theoretical point of view: the rectangular FDA and the circular FDA, whose schematics are provided in Fig. 8.

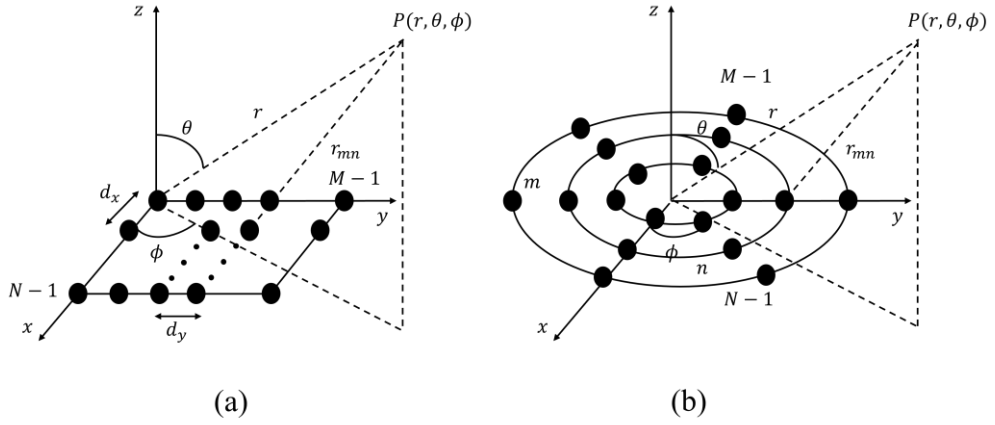


Fig. 8. (a) Rectangular FDA and (b) Circular FDA

In rectangular FDAs  $M \times N$  elements lay on  $xy$ -plane, organized in  $M$  rows equally spaced by  $d_y$  and  $N$  columns equally spaced by  $d_x$ , as shown in Fig. 8(a). Each  $mn$ -th element has distance  $r_{mn}$  from the generic far-field point  $P(r, \theta, \phi)$  that can be written as:

$$r_{mn} = \sqrt{(nd_x - r\sin\theta\sin\phi)^2 + (md_y - r\sin\theta\cos\phi)^2 + (r\cos\theta)^2} \quad (5)$$

Given the high number of elements, exciting  $M \times N$  signals each one at different frequency would result unfeasible. A solution, firstly proposed by the author, is applying frequency diversity just along rows, having elements belonging to the same column that radiate the same signal. In this way, an improved directivity is obtained in the plane where

the diversity is not applied ( $xz$ -plane in Fig. 8(a)), while in the diversity plane ( $yz$ -plane in Fig. 8(a)) the same characteristic retrieved for uniform FDAs (the ‘S-shape’) is retrieved if  $d_x = d_y = \frac{\lambda}{2}$ . Simulations of the BP with  $M = 4$ ,  $N = 8$  and  $\Delta f = 5 \text{ MHz}$  are provided in Fig. 9, for  $t = 100 \text{ ns}$  in the  $(r, \theta)$  plane for  $xz$ -plane and  $yz$ -plane.

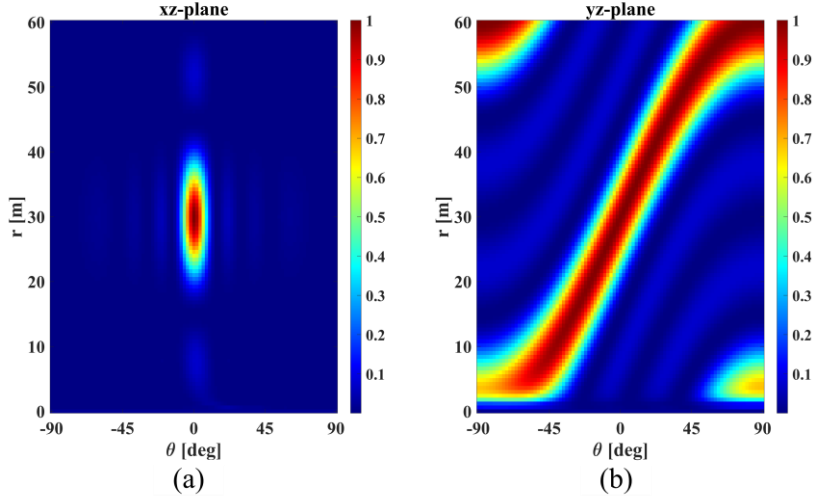


Fig. 9. Uniform rectangular FDA BP in (a)  $xz$ -plane and (b)  $yz$ -plane

This solution can exploit the auto-scanning feature of the linear FDA with an improved directivity in the plane orthogonal to the one where the diversity is applied and be profitably exploited for precise sectorial localization purposes, but it is not suitable for powering applications, showing the same limitations of the linear case.

A practical implementation, realized by the author for the first time, is represented by a planar series-fed operating at  $1.95 \text{ GHz}$  presented in Fig. 10. The topology consists of a 4-finger transmitter whose single radiating element is a series-fed array [37] composed by 3 patch antennas, realized on 1 mm thick ISOLA DE104 substrate ( $\epsilon_r = 4.37$  and  $\tan\delta = 0.022$ ).

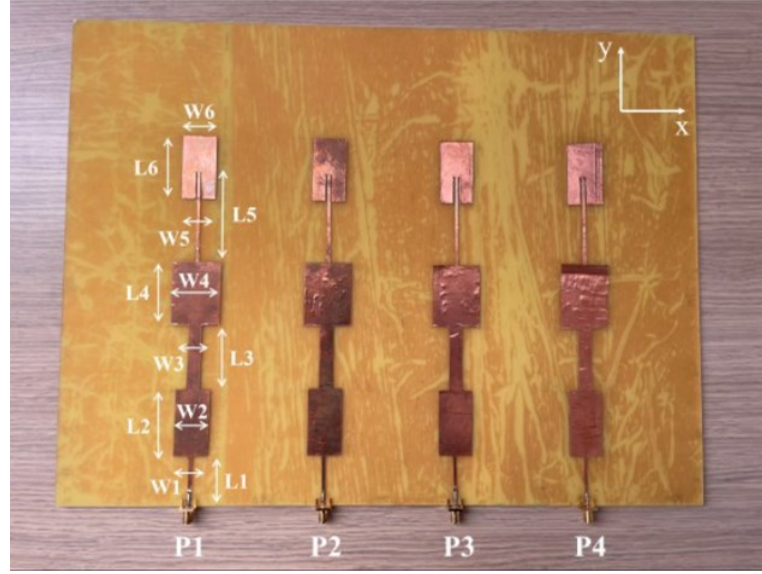


Fig. 10. Prototype of the planar series-fed frequency diverse array. © 2023, EurAAP

The initial value for the inter-element distance in a finger (in the  $y$ -direction) has been set to  $L = \lambda$ , to ensure that all the elements radiate the signals in phase ( $\beta L = 2\pi$ ). Moreover, the width of the first microstrip line is set to ensure an input impedance of  $50 \Omega$ . The tuning of the design parameters, especially the width and length of the patches, the inter-element distance, the width of the microstrip lines and the inset have allowed to double the 10 dB bandwidth with respect to standard series-fed array. Adjacent fingers are spaced by  $d_0 = \lambda_0/2 = 83.3 \text{ mm}$  in the  $x$ -direction. All the parameters presented in Fig. 10 are listed (in  $\text{mm}$ ) in Table 1.

Table 1 © 2023, EurAAP

$L_1$	$L_2$	$L_3$	$L_4$	$L_5$	$L_6$
30	40	40.57	39.5	57.5	40
$W_1$	$W_2$	$W_3$	$W_4$	$W_5$	$W_6$
2	21	8	30	2	21

Even though the enlargement of the operating bandwidth of this prototype doesn't have a direct impact in the analysis presented at this point, vice versa it represents a crucial requirement when WPT purposes are envisaged and will be explained in the next sections.

The near-field characterization has been performed by measuring the reflection coefficient of each port and their mutual coupling with Agilent FieldFox Vector Network Analyzer N992A. For the sake of clarity of the figure, the sole parameters related to port 2 are presented in Fig. 11. Those referring to the other ports are almost overlapped.

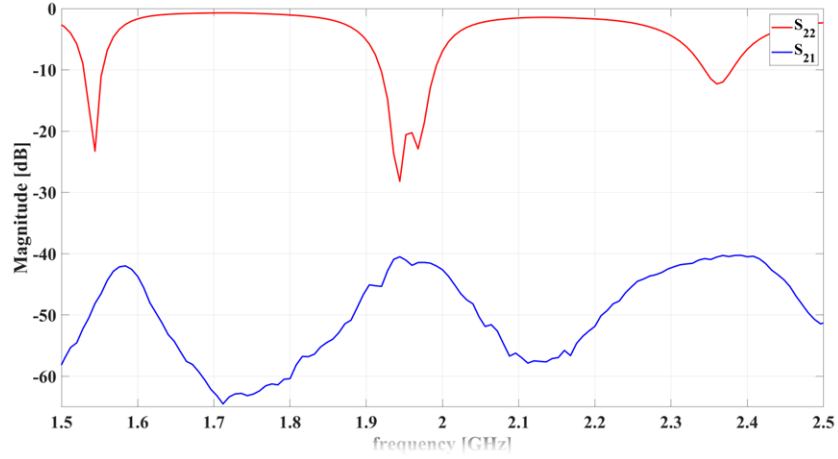


Fig. 11. Measured  $S_{22}$  and  $S_{21}$ . © 2023, EurAAP

As can be evinced from the Fig. 11, the working frequency is around  $1.95\text{ GHz}$  with an operating bandwidth of approximately  $90\text{ MHz}$ , where the isolation is below  $-40\text{ dB}$ . The radiation properties have been retrieved by measuring the radiation diagrams in the xz- and yz-plane, exciting each port once at a time, with a signal of frequency  $1.95\text{ GHz}$  with the Hittite HMC-T2100 signal generator. The normalized radiation pattern (again for the case of port 2 excitation), is shown in Fig. 12.

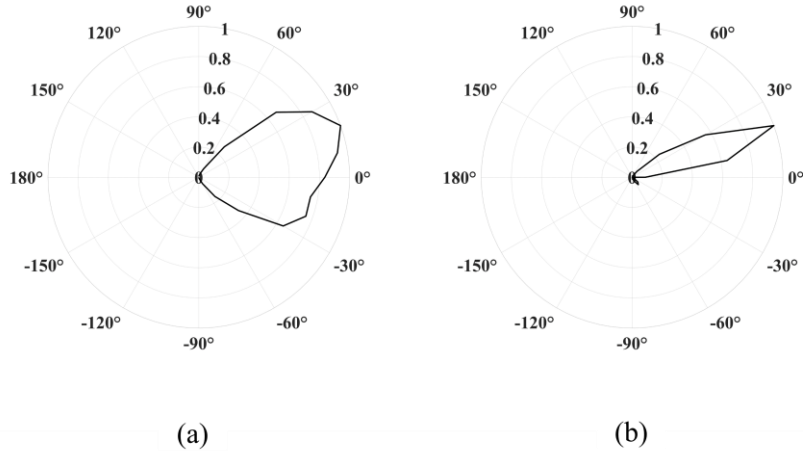


Fig. 12. (a) Measured normalized radiation pattern for  $\phi = 0^\circ$  (b) and measured normalized radiation pattern for  $\phi = 90^\circ$ . © 2023, EurAAP

In Fig. 12(a), for the plane  $\phi = 0^\circ$  (the diversity plane) a quite large half-power beam width (HPBW) has been obtained (approximately  $70^\circ$ ), while the desired increased directivity has been obtained in the plane  $\phi = 90^\circ$ , confining the radiation in a sector of approximately  $20^\circ$ , with a maximum for  $\theta = 20^\circ$ . This tilt is also present in the full-wave simulation of the finger, due to a non perfect in-phase excitation of the 3 elements in series.

In circular FDAs, introduced in [30], the elements laying on  $xy$ -plane are arranged in  $N$  concentric rings of  $M$  elements each, as shown in Fig. 8 (b). Depending on how the frequency diversity is applied, two solutions can be identified: the circular concentric FDA (CCFDA) and the radial FDA (RFDA). In the first case [30], the diversity is applied by ring, i.e. all the elements belonging to the same ring radiates signals at the same frequency  $f_n = f_0 + n\Delta f$ . In the second one, an innovative solution firstly proposed by the author where the diversity is applied by radii, i.e. elements belonging to the same radius radiates signals at the same frequency  $f_m = f_0 + m\Delta f$ , is provided. Each  $m$ -th radiator in  $xy$ -plane can be identified by a radius  $\rho_{mn}$  and an angle  $\phi_{mn}$ , therefore the distance  $r_{mn}$  from the generic far-field point  $P(r, \theta, \phi)$  can be expressed as  $\sqrt{D}$ , where  $D$  is:

$$D = (\rho_{mn}\sin\phi_{mn} - r\sin\theta\sin\phi)^2 + (\rho_{mn}\cos\phi_{mn} - r\sin\theta\cos\phi)^2 + (r\cos\theta)^2 \quad (6)$$

Based on the adopted solution, the value of  $\rho_{mn}$  needs to reflect the uniformity condition, i.e. elements or groups of them that radiate different frequencies should be placed multiple integers of  $d_0 = \frac{\lambda}{2}$  apart. This constraint requires to carefully select the radius of each ring and practical details will be provided in the following.

Simulations with  $M = 8$ ,  $N = 3$ ,  $f_0 = 2.45 \text{ GHz}$  and  $\Delta f = 5 \text{ MHz}$  at  $t = 100 \text{ ns}$  are provided in Fig. 13 and 14 for the CCFDA and RFDA, respectively.

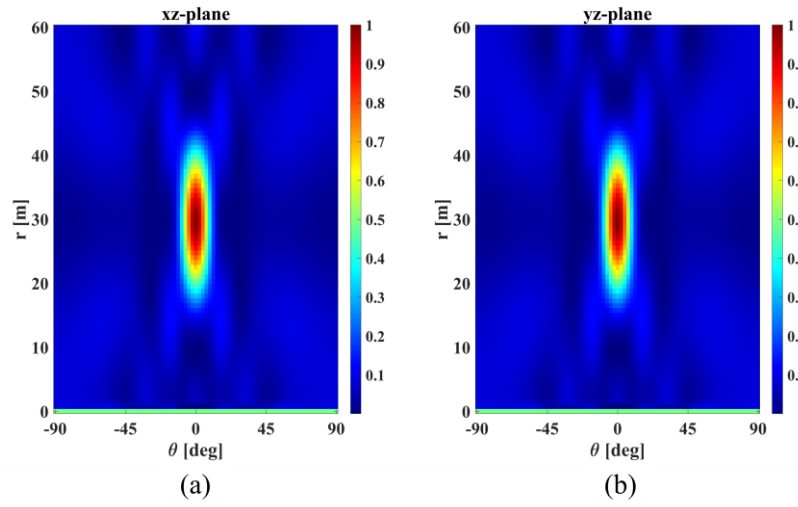


Fig. 13. Uniform CCFDA BP in (a)  $xz$ -plane and (b)  $yz$ -plane

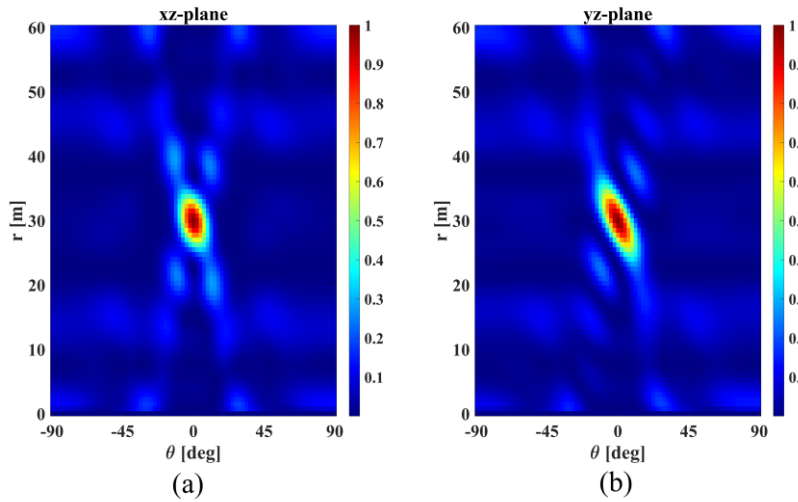


Fig. 14. Uniform RFDA BP in (a)  $xz$ -plane and (b)  $yz$ -plane

As can be evinced, circular symmetry allows to define a more defined region where to concentrate the maximum intensity of the transmitted signal, to be exploited for future systems dedicated to powering on demand applications. Indeed, in Fig. 13 and Fig. 14 the improved radiation properties of the CCFDA and RFDA are highlighted, showing a snapshot at  $t = 100$  ns: the energy can be focused on an elliptical spot for the first solution and on a quasi-elliptical for the second one, whose dimensions obviously depend on the number of rings and of elements per ring, respectively. The RFDA results more precise in terms of focusing since it implies a higher number of frequencies, that generally increase the directivity in the radial direction. To steer the beam in a predefined direction the complex weights of each group of radiators should be controlled, with a relationship that can be retrieved in the same manner as (4).

Both solutions represent a step-forward with respect to more traditional FDA architectures, where the well-known ‘S-shape’ of the BP cannot be avoided. For the above reasons, circularly symmetric layouts are the most promising architectures for WPT purposes adopting FDAs as the radiating front-end.

Within circular configurations, the RFDA represents a relatively simple solution. Even considering the inherent complexity of the RFDA feeding network, it needs a simpler design than the CCFDA. Due to the frequency diversity in the CCFDA, each ring needs to have a separate feeding network to get an in-phase excitation of all antennas, which complicates the design considerably. For this reason, two versions of RFDA, one operating at  $24\text{ GHz}$  and the other at  $2.45\text{ GHz}$ , were fully designed and experimentally characterized for the first time in this work

For the  $24\text{ GHz}$  version, a multilayer stack-up shown in Fig. 15(c) was employed, by placing the array elements on the top layer. An octagonal shape, as shown in Fig. 15(a), has been chosen to fulfill symmetry requirements and to easily place external millimeter-wave connectors for signal excitation. Such an antenna consists of 32 radiating patches placed in 4 concentric rings and aligned along 8 spokes, with 4 series-fed patch antennas each, radiating the same frequency. Indeed, all the patches are oriented in the same direction and appropriately fed in such a way that good polarization properties are maintained.



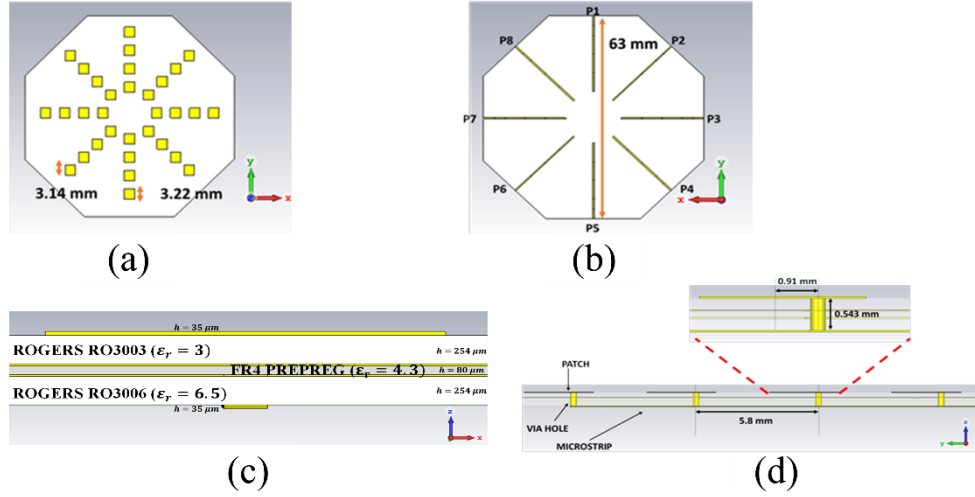


Fig. 15. (a) Front view of the octagonal-shaped RFDA with 32 patches arranged with circular symmetry. (b) Back view of the octagonal-shaped RFDA with the feeding network composed by 8 radii in microstrip technology. (c) Stack-up of the RFDA transmitter. (d) Side view of the feeding technique implementing direct connection between microstrip line and patch through a metallized via hole operating at 24 GHz. © 2022, EUMA

The bottom layer's feeding network consists of 8 microstrip lines, each with a characteristic impedance of  $50 \Omega$ , 0.35 mm wide, on 254 mm thick RO3006 substrate. Every microstrip line feeds in series the 4 patches belonging to the same spoke. The spacing between the patches is carefully arranged for the excitation to be in-phase, leading to broadside radiation. These patches are fed by the microstrip line through metallized via holes using the well-known Substrate Integrated Waveguide (SIW) technology [38]. The proposed method allows a simpler feeding strategy with respect to standard antenna feeding techniques, such as edge or aperture coupling, when applied to circularly arranged patches.

Via holes allow for easy and effective excitation of patches for any direction of incoming feeding lines and greatly simplify the feeding network design. If the via hole is placed along the vertical symmetry axis of the patch, a vertically polarized radiated field is produced, and its position along that axis helps to achieve impedance matching. A side view of one spoke is shown in Fig. 15(d).

For each spoke, the position of the via hole and the dimensions of the patch were adjusted carefully to enforce resonance. The various layers were bonded using a prepreg layer,

as depicted in Fig. 15(c). The thinnest prepreg available, 80  $\mu$ m, was used to make the via holes as short as possible to avoid becoming unwanted radiators. A prototype was built, shown in Fig. 16, and a preliminary characterization confirmed the effectiveness of such an unconventional feeding strategy.

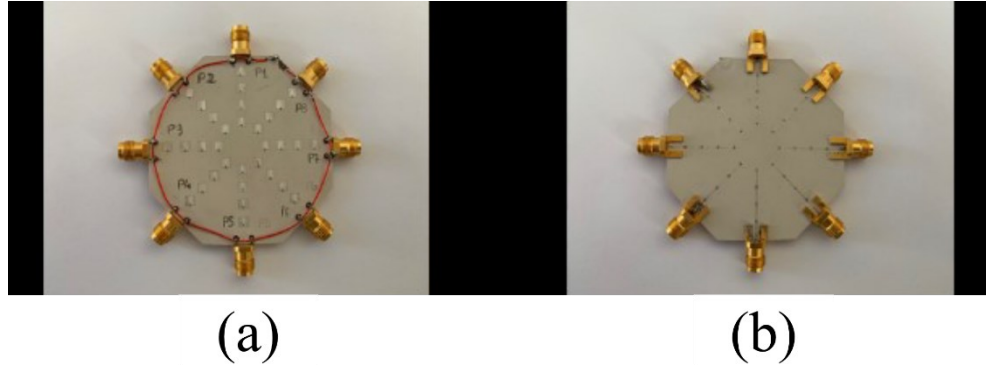


Fig. 16. (a) Front and (b) back view of the realized RFDA. © 2022, EUMA

Fig. 17 reports the comparison between experimental and simulation results in terms of input reflection coefficient at one of the 8 ports, for the present case the 5th one (similar results occur at the other ports). An acceptable down-shifting of the spoke resonance (about 5%) is observed around 23 GHz and a sufficiently wide operating bandwidth needed for frequency-diversity purposes has been ensured.

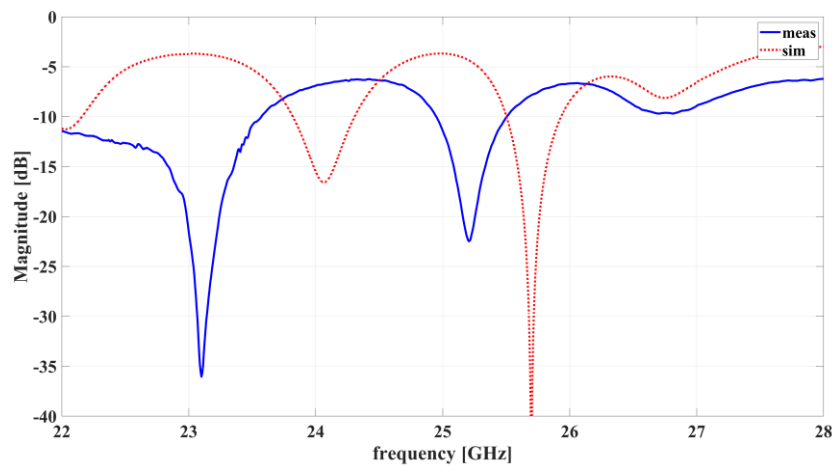


Fig. 17. Comparison between numerical and experimental reflection coefficient magnitude at port no. 5. © 2022, EUMA

Full wave simulation of the combined far-field radiation pattern shows a broadside radiation with a total radiation efficiency of 78 %, which is a satisfying value considered the complexity of the architecture, with a 18.9 *dBi* gain.

For the 2.45 GHz case, designed for performing characterization and laboratory measurements with microwave instrumentation, the same approach has been adopted, obviously adapting the stack-up for the lower frequency range, as shown in Fig. 18(c), involving a 1.524 mm ROGERS RO4350B ( $\epsilon_r = 3.66$ ,  $\tan\delta = 0.0037$ ) for the upper layer and a 0.610 mm ROGERS RO4360G2 ( $\epsilon_r = 6.4$ ,  $\tan\delta = 0.0038$ ) for the bottom one.

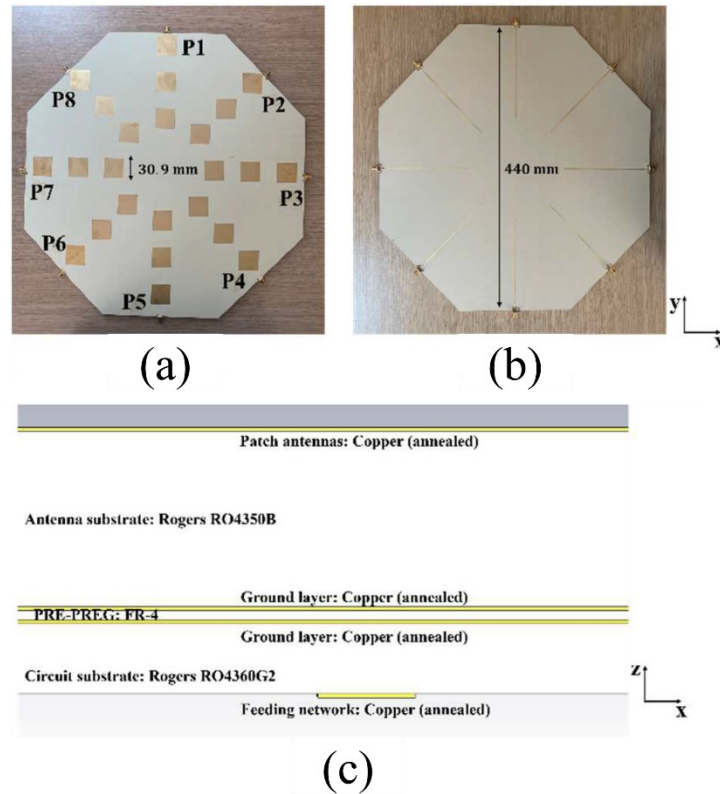


Fig. 18. (a) Front view of the octagonal-shaped RFDA with 24 patches arranged with circular symmetry. (b) Back view of the octagonal-shaped RFDA with the feeding network composed by 8 radii in microstrip technology. (c) Stack-up of the RFDA transmitter operating at 2.45 GHz. © 2024, IEEE

Due to the transmitter's dimensions, only 24 patches are arranged in the  $xy$ -plane, organized into 8 spokes with 3 elements each, as shown in Figs. 18(a) and 18(b). Fig. 19(a) presents the preliminary measurements of the prototype, showing the magnitude of the reflection coefficient at port 1. There is a good match between the simulation and experimental results, with favorable matching around the target frequency. Similar results were observed at the other ports as well. The radiation efficiency was measured at approximately 73%, with a gain of 9  $dBi$  per spoke. Finally, the far-field radiation pattern of the 8 spokes embedded in the full array is depicted in Fig. 19(b), confirming broadside radiation for all spokes, which indicates that the in-phase condition for the series-fed patch antennas is successfully achieved.

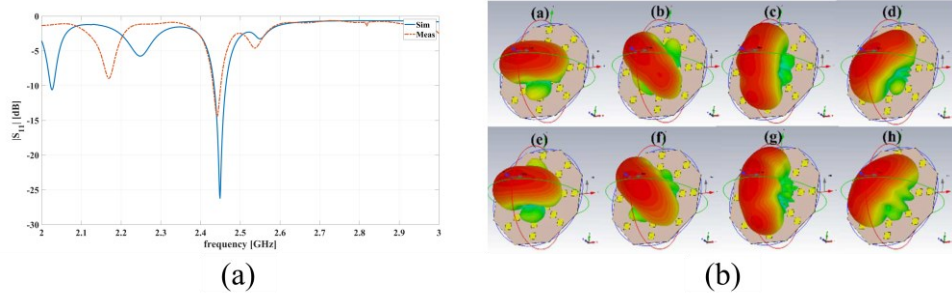


Fig. 19. (a) Measured and simulated magnitude of the reflection coefficient at port 1 of the RFDA operating at 2.45  $GHz$ . (b) Full-wave simulations of the RFDA far fields from port 1 (a) to port 8 (h) at 2.45  $GHz$ . © 2024, IEEE

## 2.4 Time controlled frequency diverse arrays

In the previous chapter the attention has been focused on the analysis of the frequency rule and the topology of the transmitter for enhancing the directivity of the FDA radiation to make this technology feasible for WPT applications. Despite the several advantages provided by these solutions, a sophisticated signal generation system with expensive phase shifters is required to steer the beam towards the desired targets, drastically increasing the costs of the entire system. Additionally, the time dependency of the radiation, responsible for the movement of the beam, introduces additional challenges for powering applications.

A practical solution to these problems can be individuated in the so-called time-controlled frequency diverse arrays (TCFDA), also named pulsed-FDA [31]. With this technique consisting in the duty-cycling of the radiation of each diverse-in-frequency element through a rectangular pulse, beam steering capability can be obtained using the simplest array configuration. By inserting low-cost RF switches, TCFDA allows one to constrain the S-shape typical pattern in a confined angular sector; furthermore, beam steering on demand can be performed by varying the pulse delay. This radiating system, proposed in the literature by the University of Bologna research group and by the authors of [31], but practically demonstrated by the research activity presented in this thesis work, operates as an advanced phased array, but with a simpler architecture since the phase shifter is replaced by a basic switch. As already remarked, the S-shaped beam pattern of uniform FDAs is characterized by strong coupling between the range and angle of the radiation pattern. This is a dynamic feature with many uses in radar and localization; however, in WPT it is desired to precisely control the radiation to direct power only towards specific target locations. To this end, a uniform FDA excitation is combined with a pulse modulation time-control strategy to suppress the S-shape in favor of angle-confined radiation and, at the same time, to solve the challenging mutual dependency between range and direction, as illustrated in Fig. 20.

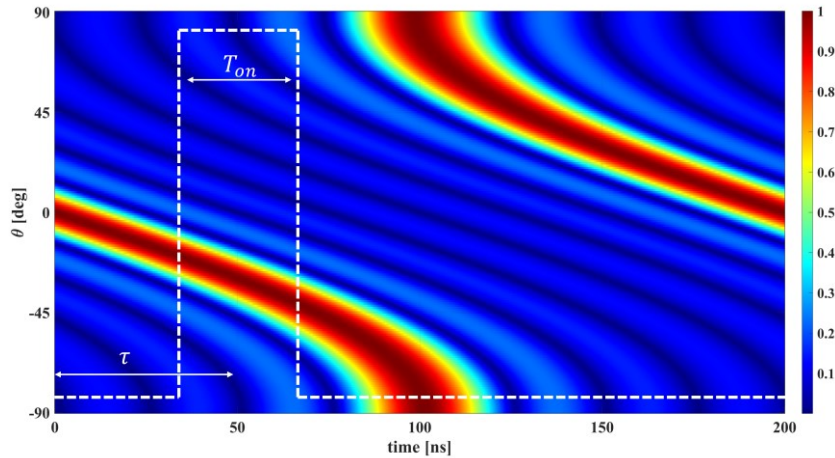


Fig. 20. Normalized uniform FDA beam pattern: (a) time-varying behavior and superimposed pulse (dashed line) with on-time  $T_{on} = 20 \text{ ns}$  and delay  $\tau = 50 \text{ ns}$ .

In this scenario, the overall signal transmitted by the array can be cast in the following form (by skipping the  $\text{real}\{\}$  operator for simplicity):

$$x(t) = x_{\text{pulse}}(t - \tau) \sum_{m=0}^{M-1} e^{j2\pi f_m t} \quad \text{with } m = 0, \dots, M - 1 \quad (7)$$

Here,  $x_{\text{pulse}}(t)$  represents the pulse waveform. The design of the rectangular pulse shape involves setting key parameters, such as the period  $T$ , the on-time  $T_{\text{on}}$  and the delay  $\tau$ . These variables provide essential flexibility in selecting specific time slots for radiation, allowing for the dual objective of maximizing power transmission in targeted directions and eliminating radiation in undesired areas, as shown in Fig. 20.

For the sake of simplicity, let's consider a scenario where the target is in the broadside direction for which the correct delay that needs to be set is 0 s. The effect of the time-based technique on the FDA radiation is clearly visible in Fig. 21, where multiple snapshots of the beam pattern have been collected at different distances, with  $M = 8$ ,  $f_0 = 2.45 \text{ GHz}$ ,  $\Delta f = 5 \text{ MHz}$ ,  $T = 200 \text{ ns}$ ,  $T_{\text{on}} = 20 \text{ ns}$  and  $\tau = 0 \text{ s}$ .

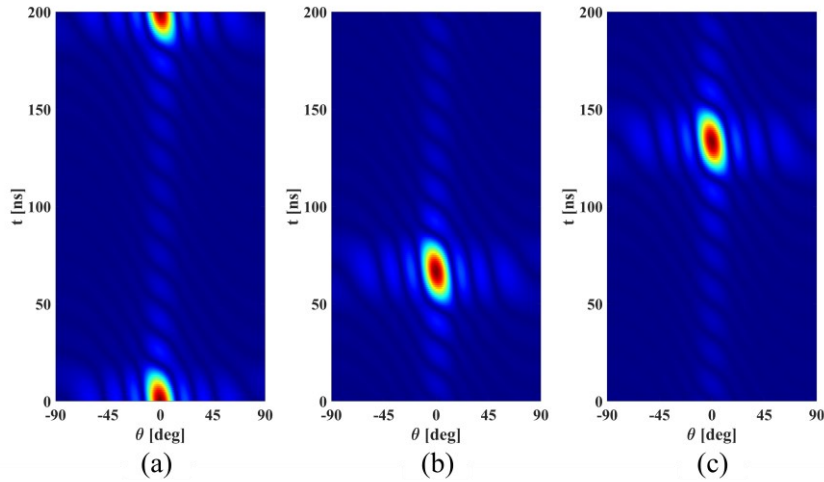


Fig. 21. Normalized TCFDA beam pattern (with rectangular pulse effect) at: (a)  $r = 0 \text{ m}$ , (b)  $r = 20 \text{ m}$ , (c)  $r = 40 \text{ m}$ .

The movement of the radiation over time is clearly noticeable, although pulse modulation enables the restriction of transmission to a specific direction. This provides a

significant advantage compared to the standard approach when precise and intentional power transfer is required.

In literature this technique has been analysed respect to the time domain only [31]; however when powering applications are involved, the frequency analysis results mandatory to correctly evaluate the transmitted power.

Let's consider the same scenario represented in Fig. 4, with  $M = 4$  radiating elements aligned along the  $x$ -axis. If compared to the uniform case previously presented where CW signals were radiated, the introduction of the pulse signal creates a spectrum that contains infinite harmonic components associated to each fundamental signal, as schematically represented in Fig. 22, where  $f_p = \frac{1}{T}$  is the pulse frequency, that defines the spacing between adjacent harmonic tones.

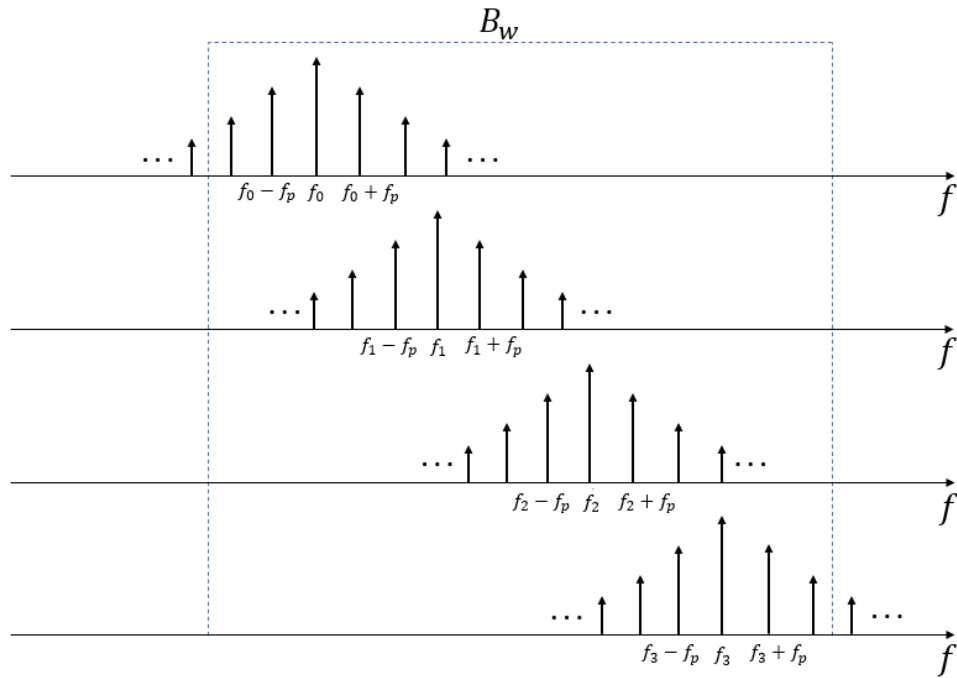


Fig. 22. Spectrum of a pulsed FDA (M=4). © 2023, IEEE

Harmonic analysis can be conducted with a focus on either information transmission or power transmission. In terms of communication, the harmonic terms generated by pulse modulation pose a significant risk to the quality and reliability of the link. Therefore, the following strict condition must be met:

$$(M - 1)\Delta f < f_p \quad (8)$$

The left-hand side term of (4) defines the frequency distance between the lowest and the highest fundamental tones of a M-elements FDA. If condition (4) is satisfied, the first sidebands (i.e. harmonic order equal to 1) of  $f_m$  satisfy the following inequalities:

$$f_m + f_p > f_{M-1} \text{ with } m = 0, \dots, M - 1 \quad (9)$$

$$f_m - f_p < f_0 \text{ with } m = 0, \dots, M - 1 \quad (10)$$

In this way, co-channel interference is avoided by distributing the harmonic terms outside the channel bandwidth  $Bw$ , which is an essential requirement for proper data communication. Another key point to be noted here is that a pass-band filter must be used to reduce adjacent channel interference with other users. However, due to the large number of harmonics, much of the radiated power gets dispersed at those frequencies, and there are massive power losses in the sideband harmonics. This is a big challenge to the feasibility of TCFDA, hence making the technique unreliable for communication purposes.

However, this thesis work offers another perspective that better suits WPT applications. If TCFDAs are applied to power transmission, condition (8) may be ignored to allow harmonic terms in the bandwidth to contribute with additional power delivery in the frequency range of interest. In this case, the implicit harmonics contents from pulses are profitably utilized to deliver power, which intrinsically reduces the power lost, as will be shown in the following analysis.

Another reason for neglecting condition (8) in WPT applications is dictated by a hardware constraint about the generation of multi-frequency signals. Indeed, the CW generated signal is usually post-processed by a PWM and the resulting pulsed signal is radiated by the antenna. In particular, the pulse design parameters  $\tau$  and  $T_{ON}$  are key parameters that rule the FDA radiation performance. The first consideration involves the relationship between the time periodicities of the pulse and the FDA pattern. The second one sets the maximum time window of interest to  $\frac{1}{\Delta f}$ . If  $f_p$  exceeds  $\Delta f$ , the pulse signal will repeat



multiple times within a single FDA period, causing the unique correspondence between  $(\tau, T_{ON})$  and the angle, shown in Figure 20, to be lost. This implies that the system will radiate in various directions within one period, whereas the focus of this work is to analyze the harmonic contributions of a single pulsed FDA beam, where the direction of transmission is fixed. Therefore, the frequency offset  $\Delta f$  represents an upper limit for the pulse periodicity, necessitating the following additional condition:

$$f_p \leq \Delta f \quad (11)$$

On the other hand, a lower bound for  $f_p$  cannot be determined. However, the designer should be aware that increasing the pulse's time periodicity, while keeping the  $T_{ON}$  and  $\tau$  parameters (and thus the steering direction and focusing area size) fixed, will result in less power being delivered to the target (e.g., a rectenna) due to the extended silent period. This issue will be addressed further in the subsequent analysis by defining an appropriate figure of merit related to power transfer.

To effectively proceed with the power analysis of TCFDA the definition of the generic pulse modulating the CW signal is mandatory:

$$x_{pulse}(t) = \sum_{n=-N_h}^{N_h} C_n e^{j2\pi n f_p t} \quad (12)$$

Where  $N_h$  is the number of harmonic terms characterizing the pulse and  $C_n$  are its Fourier coefficients, that can be expressed as:

$$C_n = \frac{1}{T} \int x_{pulse}(t) e^{-j2\pi n f_p t} dt, \text{ with } n = -N_h, \dots, N_h \quad (13)$$

The generic signal transmitted by the  $m - th$  can be expressed as:

$$x_m(t) = e^{j2\pi f_m t} x_{pulse}(t) = e^{j2\pi f_m t} \sum_{n=-N_h}^{N_h} C_n e^{j2\pi n f_p t} \quad (14)$$

Due to the periodic nature of  $x_m(t)$ , the average power of the signal can be computed as:

$$P_{x_m} = \sum_{n=-N_h}^{N_h} |C_n e^{j2\pi(f_m+n f_p)t}|^2 \quad (15)$$

The total signal radiated in far field by the array is:

$$x(t) = \sum_{m=0}^{M-1} e^{j2\pi f_m(t-\frac{r_m}{c})} \sum_{n=-N_h}^{N_h} C_n e^{j2\pi n f_p(t-\frac{r_m}{c}-\tau)} \quad (16)$$

Since  $x(t)$  is a periodic signal as well, the total average radiated power can be cast as in the following:

$$P_x = \sum_{m=0}^{M-1} \sum_{n=-N_h}^{N_h} |C_n e^{j2\pi(f_m+n f_p)(t-\frac{r_m}{c}-\tau)}|^2 \quad (17)$$

Once the total power is defined, the Power Loss figure of merit can be derived as:

$$P_{loss}[\%] = \left(1 - \frac{P_{x_{Bw}}}{P_x}\right) 100 \quad (18)$$

where  $P_{x_{Bw}}$  represents the total average signal power within the interested bandwidth. It is evident how  $P_{loss}$  identifies the amount of power that the system loses on the sideband harmonics with respect the total available power and it is strictly related to the bandwidth  $Bw$  choice.

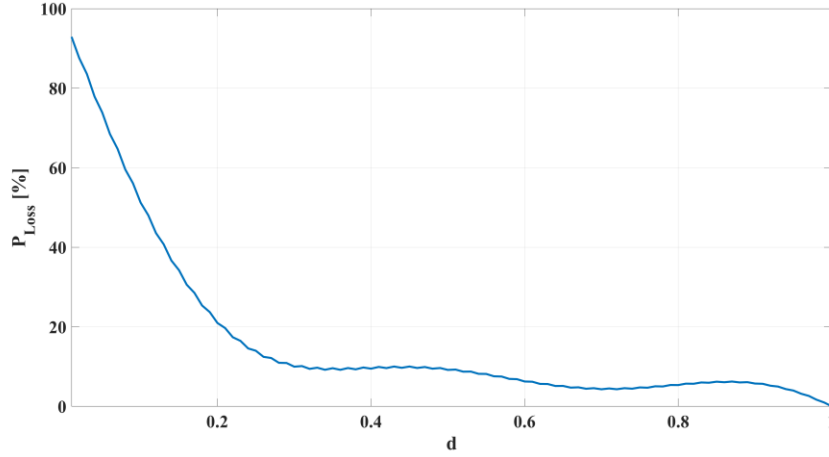


Fig. 23. Power Loss curve with a rectangular pulse,  $f_p=20\text{ MHz}$  and  $Bw=100\text{ MHz}$ .

A simulation example is reported in Fig. 23, considering  $M = 4$ ,  $f_0 = 1.8\text{ GHz}$  and  $\Delta f = 5\text{ MHz}$ , where the  $P_{loss}$  is given as a function of the duty-cycle (the ratio between the on-time period and periodicity  $T$ ). The value of the bandwidth  $Bw$  is set to  $100\text{ MHz}$  and  $f_p = 20\text{ MHz}$ . This value greater than  $\Delta f$  has been chosen following (8), in accordance with the communication scenario. Consequently, the system generates more than one maximum in the FDA period since equation (11) is violated. Due to this set-up, considering small duty-cycle values (e.g.,  $0.1 \div 0.2$ ), as envisaged for TCFDA systems because they directly impact on the size of the beam spot, an extremely high value of  $P_{loss}$  (between  $50\% - 60\%$ ) is retrieved, highlighting how the majority of the transmitted power is wasted on sideband harmonics.

It is evident that to effectively exploit TCFDA for powering application, a minimization of the  $P_{loss}$  figure must be pursued, and this can be obtained through the design of the modulating pulse that plays a fundamental role for system performance optimization with respect to power transmission.

An immediate improvement with respect to the previous case is given by the choice of  $f_p = \Delta f = 5\text{ MHz}$ , hence fulfilling (11). In this case, the lower order harmonics of each fundamental frequency  $f_m$  are superimposed to the adjacent fundamental. Since information distortion is no longer a concern, harmonic radiation can be effectively utilized to enhance

power distribution within  $Bw$ , thereby minimizing  $P_{loss}$ . Different modulating pulse have been adopted and the performance in terms of  $P_{loss}$  have been compared.

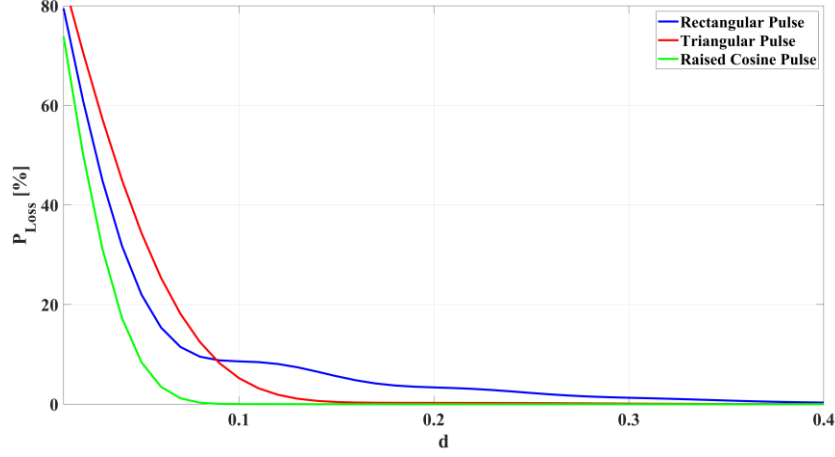


Fig. 24. Power Loss for various TCFDA configurations: (blue) rectangular pulse, (green) raised cosine pulse, (red) triangular pulse.

### ***Rectangular Pulse***

The first modulating pulse that has been analysed was the rectangular pulse with a unitary amplitude  $A = 1$  and a duty cycle  $d = \frac{T_{on}}{T}$  whose Fourier expression can be cast as:

$$x_{rect}(t - \tau_{rect}) = \sum_{n=-N_h}^{N_h} C_n^{rect} e^{j2\pi f_p(t-\tau_{rect})} \quad (19)$$

where  $C_n^{rect} = A \text{sinc}(nd)$ .

As can be evinced from the Power Loss behaviour presented in Fig. 24 (blue curve), a direct comparison with the previous case in Fig. 23 demonstrates that the dissipated power is significantly reduced, showcasing the effectiveness of TCFDA for WPT applications. By setting the duty cycle to 0.1 (i.e., 10% of  $T$ ), which corresponds to an illuminated region of approximately 24 degrees as shown in Fig. 21, the  $P_{loss}$  results around 9%.

### ***Raised Cosine Pulse***

A raised cosine waveform has been explored and tested for the first time within a TCFDA system. The roll-off factor  $\alpha$  is crucial for pulse design: at  $\alpha = 0$ , the pulse is a rectangular shape, whereas higher  $\alpha$  values result in a smoother transition between pulse states. As the duration of pulse transitions increases with  $\alpha$ , a consistent definition of the pulse duty cycle is established by setting the pulse on-time to the time window where the raised cosine pulse exceeds 0.5. This ensures that  $T_{on}$  remains constant regardless of  $\alpha$ , and the duty cycle is derived accordingly, as shown in Fig. 25.

Simulation results for the TCFDA with  $\alpha = 1$  (shown as the green curve in Fig. 24) compared to those with  $\alpha = 0$  reveal that the smoother waveform significantly reduces the spectral components, contributing to a decrease in  $P_{loss}$ . With a duty cycle of 0.1,  $P_{loss}$  falls below 1%.

### ***Triangular Pulse***

The accuracy of the time-control technique can be greatly enhanced by introducing a triangular pulse in place of the rectangular one. A triangular waveform is created by the convolution of two identical rectangular pulses.

$$x_{tri}(t - \tau_{tri}) = x_{rect}(t - \tau_{rect}) * x_{rect}(t - \tau_{rect}) \quad (20)$$

where  $*$  stands for the time domain convolution among signals.

The delays applied to the rectangular and triangular pulses are denoted as  $\tau_{rect}$  and  $\tau_{tri}$ , respectively. Due to the Fourier properties of convolution, the resulting triangular waveform has twice the delay of the original rectangular wave ( $\tau_{tri} = 2\tau_{rect}$ ), while maintaining the same periodicity. Although the definition of the duty cycle for this new waveform is not straightforward, the on-time is calculated as the interval where the triangular pulse is non-zero, consistent with the rectangular case. Consequently, the duty cycle definition remains unchanged, as visible in Fig. 25.

The time-control technique using triangular pulse modulation achieves exceptionally precise power focusing. A triangular signal peaks at a single time instant, resulting in a radiating spot that is confined in a specific and narrow region. By appropriately selecting  $\tau_{tri}$ ,

maximum power focusing can be ensured in the target direction, significantly minimizing energy loss in surrounding areas. The improved energy efficiency of this method, compared to the traditional square pulse approach, is illustrated in Fig. 26, where the enhanced selectivity of the power spot for TCFDA with the triangular pulse is evident. For this comparison, both pulses have a duration of 20 ns and a delay of 0 s to achieve maximum power in the broadside direction.

The triangular pulse features reduced harmonic content compared to the rectangular pulse, resulting in lower  $P_{loss}$  and thereby improving TCFDA performance. This improvement is depicted in Fig. 24 (red line), where a duty cycle of 0.1 corresponds to  $P_{loss} = 5.4\%$ .

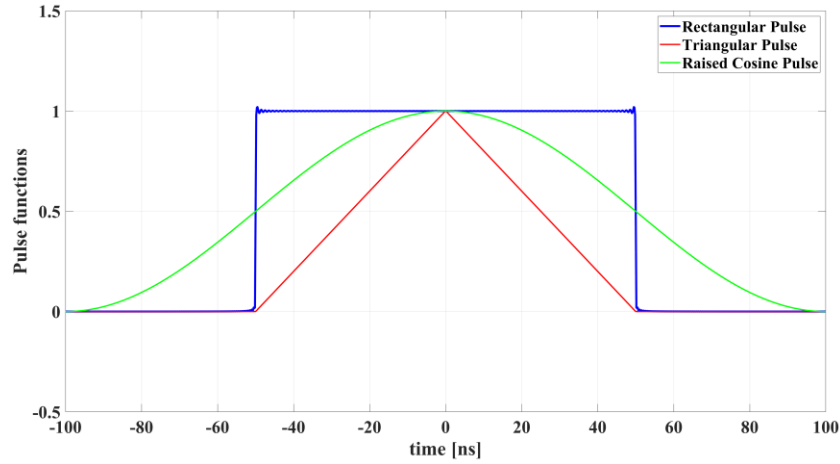


Fig. 25. Pulse functions.

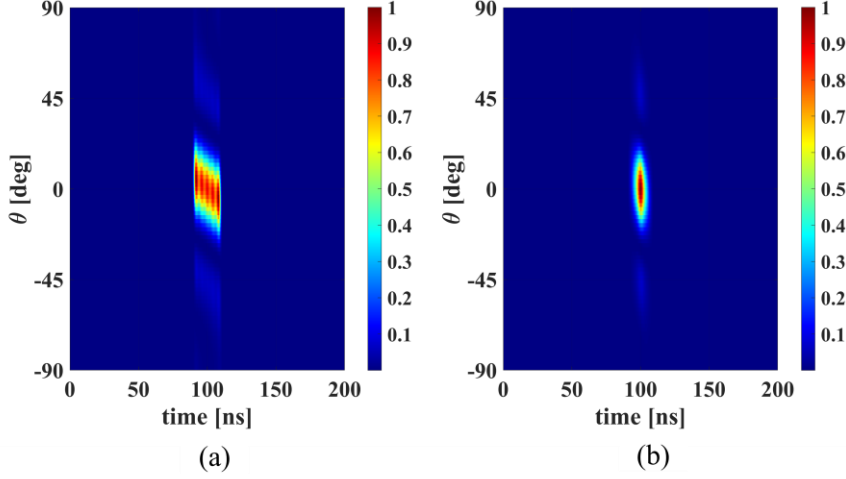


Fig. 26. Normalized TCFDA beam pattern: (a) rectangular pulse (b) triangular pulse, with time fixed at  $r = 30 \text{ m}$ ,  $T_{on} = 20 \text{ ns}$ , and  $\tau = 0 \text{ ns}$ .

By analysing the simulation results using different pulse shapes (Fig. 24), it is evident that the TCFDA system with a raised cosine pulse at  $\alpha = 1$  achieves the greatest reduction in  $P_{loss}$ . However, when considering beam spot precision, the triangular pulse offers the most accurate radiation mechanism. Additionally, for a fixed bandwidth of  $100 \text{ MHz}$ , the pulse duty cycle has the most significant impact on  $P_{loss}$ , while the pulse shape influences  $P_{loss}$  only marginally (e.g., 5.4% for the triangular pulse versus about 1% for the raised cosine). Overall, since  $P_{loss}$  values below 10% are acceptable for harmonic exploitation, the triangular pulse modulation is recommended for the TCFDA system, as it provides greater precision in radiating spot selection. If the primary system requirement is angular accuracy of the FDA radiation, selective waveforms like the triangular pulse are preferable. Conversely, if minimizing  $P_{loss}$  is the primary objective, smoother waveforms like the raised cosine pulse should be used. Naturally,  $P_{loss}$  decreases rapidly with an increasing duty cycle, as the system approaches continuous operation (achieved when  $d = 1$ ), causing harmonic terms to diminish. However, for effective control of the FDA radiation pattern, the pulse duty cycle must remain relatively low, typically around 0.1 when working with frequency spacing in the  $\text{MHz}$  range. Once this condition is satisfied, the resulting TCFDA system can be effectively used for accurate WPT.

Another way to analyse the behaviour of the TCFDA system is by changing the pulse periodicity  $T = \frac{1}{f_p}$ , while keeping the amplitude of the transmitted signals and the pulse's on-time constant (with the on-time set at 20 ns). This ensures that the TCFDA technique remains effective despite any time variations in the pattern. To assess the system's power transfer efficiency, a new metric called Powering Effectiveness  $PE$  is introduced:

$$PE = \frac{P_{x_{Bw}}}{P_{Bw}^{max}} \frac{T_{obs}}{T} \quad (21)$$

where  $T_{obs}$  is the observation time in which the powering process is analysed ( $T_{obs} \gg T$ ), and  $P_{Bw}^{max}$  is the maximum amount of power that can be transmitted, once the on-time and the delay of the pulse are fixed.

The results for different  $f_p$  values using a rectangular pulse shape, shown in Fig. 27, demonstrate that a higher pulse repetition frequency leads to greater power delivery, simply because the system stays active for a longer duration. The value of 5 MHz is identified as the optimal case, as it represents the maximum allowable  $f_p$  based on equation (11), thereby maximizing Powering Effectiveness. To illustrate this, Powering Effectiveness is normalized relative to its maximum value (which occurs at  $f_p = 5 \text{ MHz}$ ), and the resulting curve is presented in Fig. 27.

In this respect, resorting to a TCFDA system instead of standard phased arrays for WPT scenarios is relevant not only for the simpler and more flexible architecture, but also from the power delivery viewpoint, notwithstanding the pulsed nature of the radiation. Actually, the peak power of a TCFDA pulse can be increased even beyond the limit imposed for a phased array provided that the time average is below the regulatory limits. This procedure allows a battery-less sensor to effectively exploit the accurate and periodic delivery of RF power at its location.

For example, let's consider a rectifying antenna (rectenna) [36] powering the sensor, which consists of a voltage doubler loaded with a parallel combination of a 10 pF capacitor and a 1 kΩ resistor. In this case, the charging time constant for the load (representing either the optimal load for the rectenna or the equivalent impedance of a power management unit)



is  $10\text{ ns}$ . With the pulse duration set at  $20\text{ ns}$ , it ensures an effective charging process, reaching nearly 90% of the maximum charge, as supported by experimental data. Moreover, the pulsed nature of TCFDA signals, which differs from the continuous operation of phased arrays, provides a high peak-to-average power ratio (PAPR). This feature is highly beneficial for ultra-low power applications, such as wake-up radio (WuR) systems [40], as it can significantly improve the sensitivity of a WPT receiver device.

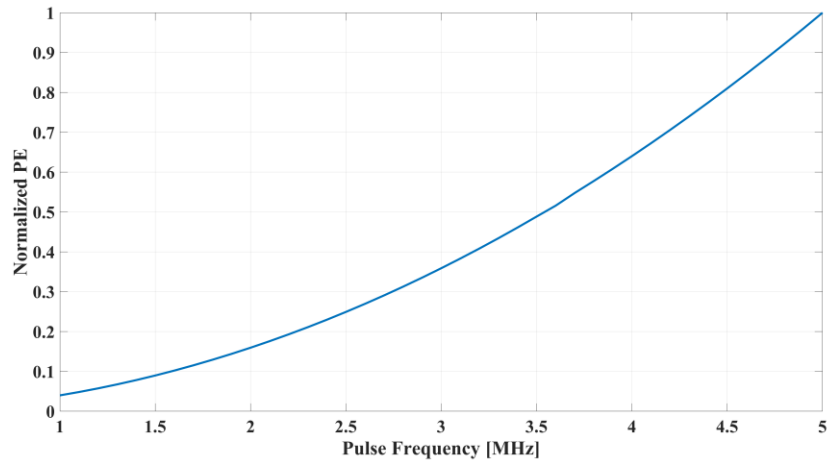


Fig. 27. Normalized Powering Effectiveness vs Pulse Frequency.

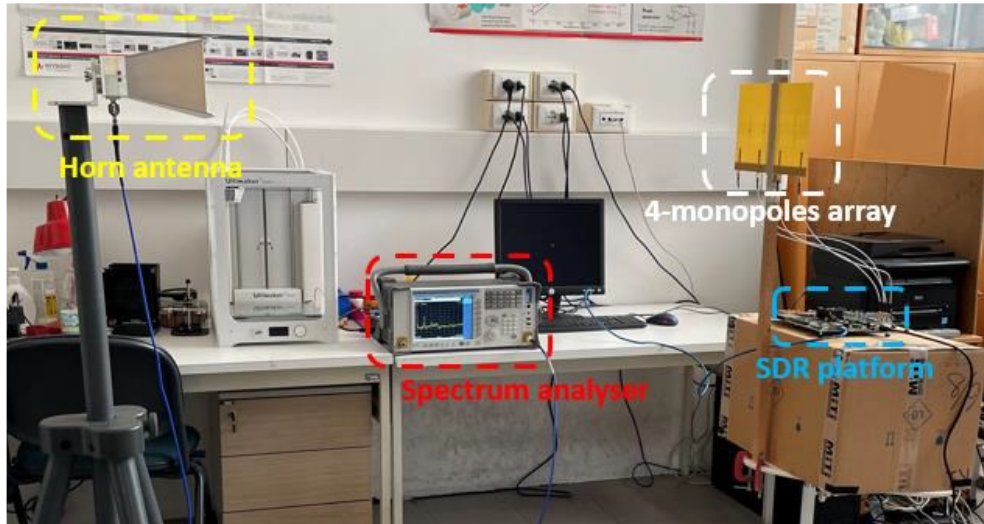


Fig. 28. Measurement set-up in an indoor environment. © 2023, IEEE

A measurement campaign was carried out to validate the simulation results. The power transmitter consisted of a 4-element monopole antenna array resonating at  $1.8\text{ GHz}$ , while the receiver used a horn antenna (TDK RF SOLUTIONS HRM-0118). A Software Defined Radio (SDR) platform (Xilinx Zynq RFSoC) was employed to simultaneously generate and control the signals transmitted by each antenna, in line with the FDA principle. A frequency offset of  $\Delta f = 5\text{ MHz}$  was applied between the array elements, resulting in transmitted frequencies of  $1.8\text{ GHz}$ ,  $1.805\text{ GHz}$ ,  $1.810\text{ GHz}$ , and  $1.815\text{ GHz}$ .

Measurements were conducted at  $1.5\text{ m}$ , limited by laboratory space, but still satisfying far-field conditions, with the receiving antenna positioned in the broadside direction relative to the transmitting array. The pulse signals were designed to appropriately excite the TCFDA system. A photograph of the experimental setup is shown in Fig. 28.

Before presenting the measurement results, it's important to consider the impact of non-ideal transmitting and receiving elements. Specifically, the bandwidth of real antenna arrays is limited, and the radiated power is directly related to this factor. In general, the radiation efficiency of the transmitting antenna system is defined as:

$$\eta_T = \frac{P_T}{P_A} \quad (22)$$

where  $P_A$  represents the total available input power, and  $P_T$  is the effective radiated power, which depends on the transmitting antenna's bandwidth. Consequently, power loss calculations account for the available bandwidth, as no radiation occurs outside this range. The total average signal power  $P_x$  was measured across a  $300\text{ MHz}$  band, corresponding to the bandwidth of the 4-monopole array prototype used as the transmitter. This value was used as the denominator in the  $P_{loss}$  equation (18), and multiple measurements were taken by varying  $Bw$  (i.e., measuring different levels of  $P_{Bw}$ ). Under the same operating conditions with the pulse duty cycle fixed at 0.1, a direct comparison of simulated and measured  $P_{loss}$  curves are presented in Fig. 29.

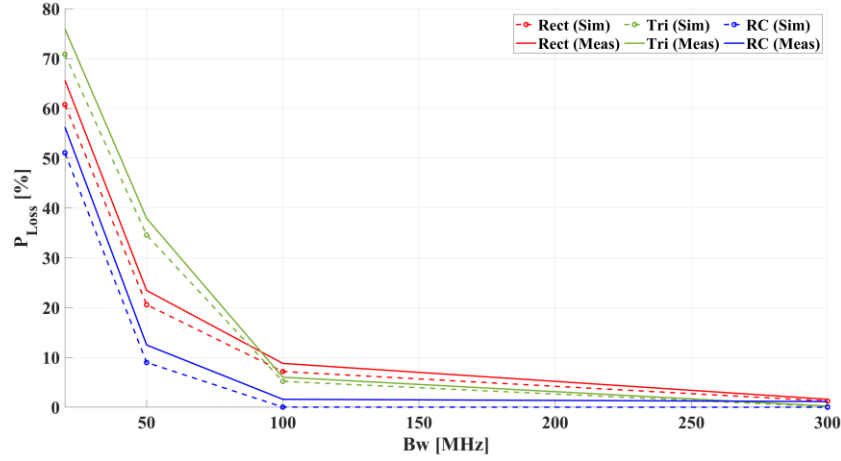


Fig. 29. Power Loss vs bandwidth: simulations and measurements results (rectangular pulse (red), triangular pulse (green), raised cosine pulse (blue)). © 2023, IEEE

As shown in the plots, both the simulated and measured curves exhibit similar trends and support theoretical predictions: as bandwidth increases,  $P_{loss}$  decreases due to the distribution of more harmonic power within  $Bw$ . Fig. 30 compares the measured  $P_{loss}$  (for clarity, only measured results are shown) based not only on different pulse shapes but also on pulse durations: increasing  $f_p$  (and thus reducing pulse duration) results in a greater power loss.

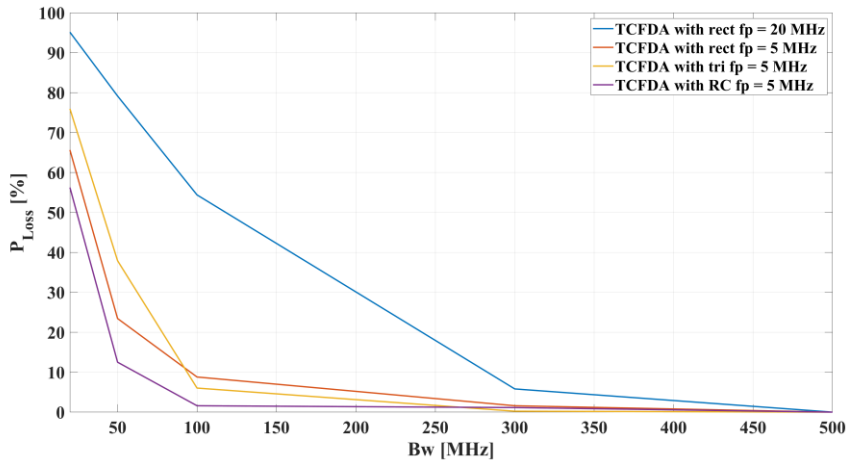


Fig. 30. Measured Power Loss vs bandwidth: (blue) rectangular pulse with  $f_p = 20$  MHz, (red) rectangular pulse with  $f_p = 5$  MHz, (yellow) triangular pulse with  $f_p = 5$  MHz, (purple) raised cosine pulse with  $f_p = 5$  MHz. © 2023, IEEE

From these comparisons, several conclusions can be drawn. First, by time-controlling using a rectangular pulse, a significant reduction in  $P_{loss}$  is achieved by lowering  $f_p$  from 20 MHz to 5 MHz. These findings confirm the novel concept of leveraging harmonic radiation to improve the efficiency of TCFDA systems for WPT applications. Second, when  $f_p = \Delta f = 5$  MHz is selected, the raised cosine pulse with  $\alpha = 1$  provides the best minimization of  $P_{loss}$ . For example, assuming  $Bw = 100$  MHz and  $d = 0.1$ , and considering various  $f_p$  values and pulse shapes, the simulated and measured  $P_{loss}$  levels are shown in Table 2.

Table 2 © 2023, IEEE

Pulse	Simulation	Measurement
<i>Rect</i> ( $f_p = 20$ MHz)	55,31 %	54,58 %
<i>Rect</i> ( $f_p = 5$ MHz)	9,09 %	10,32 %
<i>Tri</i> ( $f_p = 5$ MHz)	5,43 %	5,91 %
<i>RC</i> ( $f_p = 5$ MHz)	0,48 %	0,76 %

These results offer valuable guidance for designers when selecting TCFDA parameters: the frequency offset  $\Delta f$  determines the FDA pattern periodicity (equal to  $\frac{1}{\Delta f}$ ) and influences the focusing direction, which is defined by the pair  $(\tau, T_{on})$ . However,  $\Delta f$  does not affect the harmonic content, which depends on the choice of pulse frequency  $f_p$ , as illustrated by the first two rows of Table 2. To conclude, this analysis suggests that setting  $f_p = \Delta f$  is the best solution to meet the main performance requirements of TCFDA systems, specifically minimizing  $P_{loss}$  for advanced WPT applications.

## 2.5 Multi-spot WPT via TCFDA

In the previous chapter the radiation properties of TCFDA have been analysed, highlighting that the time-based technique allows to obtain an agile and low-cost beam steering capability by simply introducing RF switches, thus without recurring to expensive phase-shifters and complicated feeding networks. In this section, for the first time a practical description of the TCFDA exploited for powering applications will be provided. Firstly, an investigation on the single- and multi-beam properties will be verified from the theoretical and experimental point of view for multi-target energization. Successively, the effectiveness of the realized smart RF radiator will be verified through the comparison of the rectification performance at the receiver side under different excitation conditions.

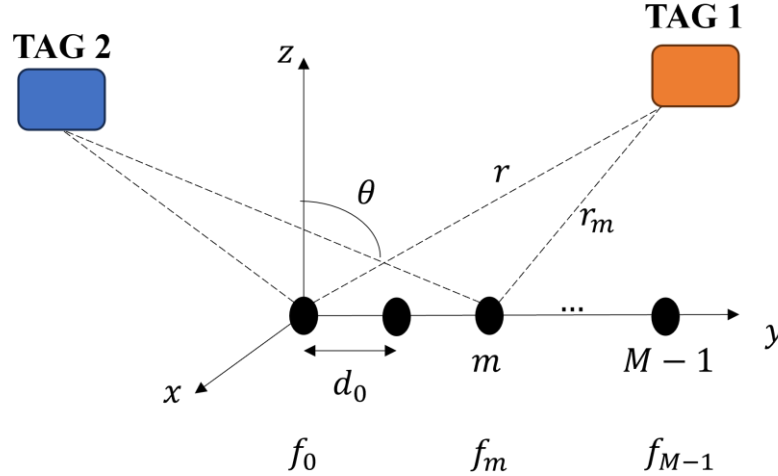


Fig. 31. Sketch of TCFDA for WPT applications. © 2024, IEEE

Let us consider a TCFDA of  $M$  isotropic elements aligned along the  $y$ -axis, equally spaced of  $d_0 = \frac{\lambda_0}{2}$  with a linear increasing frequency offset, as shown in Fig. 31, whose purpose is to illuminate randomly distributed battery-less tags. In the previous section the time-based technique has been analysed to set the characteristics of transmitting and receiving bandwidth to reduce the out-of-band power loss due to harmonic generation and the most suitable set-up in terms of pulse parameters. Here the attention will be devoted to the level of the reconfigurability of the TCFDA showing the achievable beamforming capabilities.

The aim is to illustrate the control of TCFDA achieving both single- and multi-beam configurations with standard rectangular pulses. A single beam is generated when a delayed pulse (with delay  $\tau$ ) is triggered once per period, while multiple beams are created by introducing multiple pulses (with delays  $\tau_i$ ) within the same period. The predefined  $(\tau, \theta)$  relationship enables the selection of specific pointing directions. By adjusting the pulse delay  $\tau$  based on the known FDA beam pattern (in continuous wave mode), as explained in Fig. 20, a targeted radiation direction can be achieved, producing a concentrated beam centered on a chosen  $\theta$  direction.

Differently from (12), the generic TCFDA control waveform can then be written as the sum of  $I$  pulses, each one composed of  $N_h$  harmonics, with the same pulse repetition frequency  $f_p = \frac{1}{T}$  and different delay  $\tau_i$ :

$$x_{pulse}(t) = \sum_{i=0}^{I-1} \sum_{n=-N_h}^{N_h} C_h^i \exp(j2\pi h f_p(t - \tau_i)) \quad (23)$$

where  $C_h^i$  are the complex harmonic coefficients of the  $i - th$  pulse. If a rectangular pulse is adopted, these coefficients are given by  $C_h^i = A_i d_i \text{sinc}(n d_i)$ , where  $A_i$  and  $d_i$  are the pulse amplitude and duty cycle, respectively.

To evaluate the capabilities of the modified TCFDA, the normalized behaviour of the multi-harmonic BP as a function of  $\theta$  has been provided. This is done in the plane where frequency diversity is applied (the  $yz$ -plane in Fig. 31, referred to as the diversity plane). In this case, the linear array consists of  $M = 8$  ideal isotropic elements, operating at a frequency of  $1.9 \text{ GHz}$  with a frequency step of  $\Delta f = 5 \text{ MHz}$ . The resulting patterns, shown in Fig. 32, correspond to different pulse numbers with a duty cycle of 0.1.

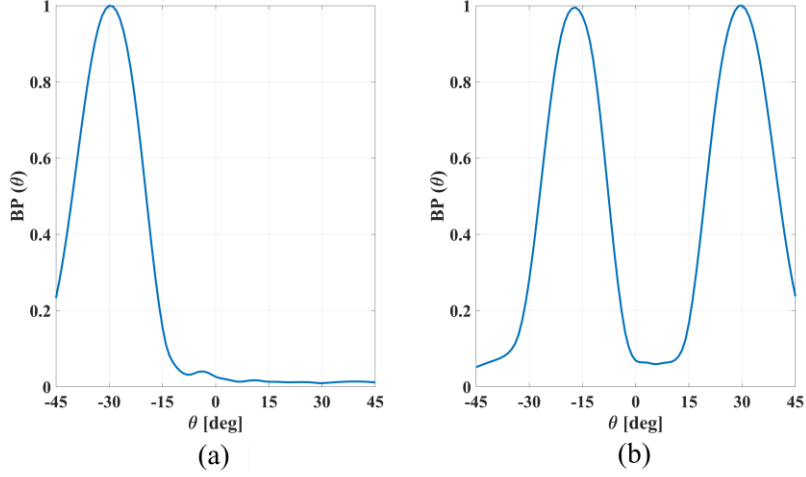


Fig. 32. Normalized multi-harmonic BP in the yz-plane (a) for  $I = 1$ , (b) for  $I = 2$ . © 2024, IEEE

In Fig. 32(a), with a delay of  $\tau = 50 \text{ ns}$ , the system periodically illuminates the area around  $\theta = -30^\circ$ , producing a beam shape influenced by both the number of array elements and the duty cycle. Meanwhile, Fig. 32(b) demonstrates the system's ability to nearly simultaneously illuminate two distinct regions around  $\theta = -20^\circ$  and  $\theta = 30^\circ$  by using two delayed pulses with delays of  $\tau_1 = 30 \text{ ns}$  and  $\tau_2 = 150 \text{ ns}$ , respectively. This behaviour highlights the advantages of TCFDA over other radiating technologies, such as PA or TMA. This can also be seen when considering the constraint imposed by the summation of two delayed pulses in the pulsed control method:

$$\tau_1 + \tau_2 \leq \frac{1}{\Delta f} \quad (24)$$

The two or more delays in the system can either be complementary or non-complementary in relation to the FDA's time periodicity, meaning that the sum of the delays may be less than or equal to  $\frac{1}{\Delta f}$ . In the second case, the combined pulsed signal behaves like a single pulse with halved periodicity, effectively doubling the repetition frequency. This causes variations in the harmonic distribution between the two cases; however, the spectral analysis previously illustrated shows no difference in power losses, and overall performance remains consistent. As a result, TCFDAs impose no restrictions on multi-beam pointing directions, allowing both symmetric and asymmetric configurations without issues. This

flexibility is a key advantage over other architectures, such as TMA, where symmetric radiation through sideband harmonics is typically achieved [38], unless complex feeding strategies are employed [42].

Additionally, TCFDAs offer significant benefits in terms of reduced hardware complexity and high reconfigurability, making them well-suited for WPT applications. This contrasts with solutions like the Butler Matrix or Rotman Lens, which, while enabling multi-beam capabilities and having simpler signal excitation (no higher harmonics to manage), require far more complex and expensive feeding networks with distributed hybrid couplers and phase shifters [43].

When realistic antenna configurations are used, the illuminated  $\theta$ -sector in the diversity plane becomes narrower due to practical limitations. This results in a reduced angular coverage, meaning that the full 180-degree span in front of the array is no longer accessible. To assess the actual angular range that can be covered, a figure of merit called the Scanning Region of the FDAs ( $SR_{FDA}$ ) can be defined as follows:

$$SR_{FDA} = \{\theta: [-90^\circ, 90^\circ] | BP(\theta) - BP_{MAX} \geq -3 \text{ dB}\} \quad (25)$$

This parameter defines the range of  $\theta$  that the FDA beam pattern can scan periodically, while maintaining a signal variation within 3 dB of its peak value ( $BP_{MAX}$ ). In an ideal TCFDA system composed of isotropic elements, the entire half-space in front of the transmitter can be scanned by following the S-shape of the beam pattern. However, in a realistic implementation, the  $SR_{FDA}$  is significantly reduced because real antennas, such as patch antennas, can only illuminate a limited angular sector. To address this limitation, the series-fed array presented in Fig. 10 was chosen as an effective topology, as it offers a relatively wide  $SR_{FDA}$ .

To validate the single-beam and multi-beam radiation capabilities of the TCFDA, measurements were conducted using a 4-finger series-fed FDA operating at 1.95 GHz, recalling that each finger composed by 3 patches series-connected presents an operating bandwidth of approximately 90 MHz, allowing efficient radiation of the harmonics generated by the pulsed excitation and minimizing power loss. The array achieves a scanning range



( $SR_{FDA}$ ) of approximately  $70^\circ$ . The measurement setup, depicted in Fig. 33, employs a software-defined radio (Xilinx ZCU111) to generate multi-channel pulsed RF excitations.

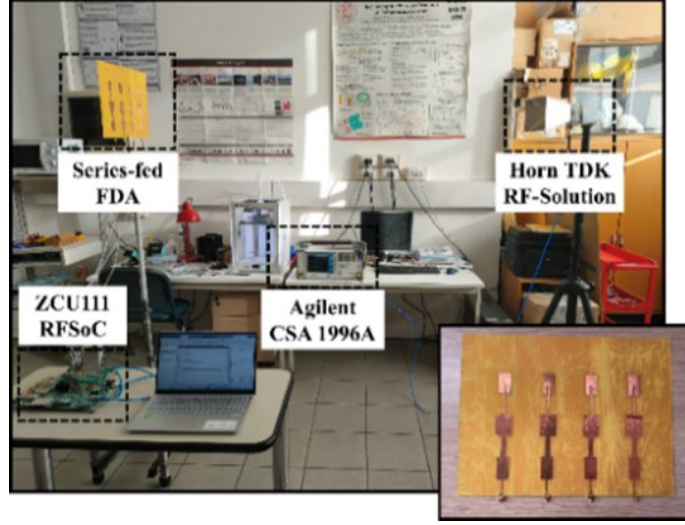


Fig. 33. Measurement set-up and zoomed view of the adopted multi-finger transmitting array. © 2024, IEEE

Fig. 34 reports predicted and experimental results for the single- and multi-beam configurations. Qualitatively these are in good agreement with those of Fig. 32: in order to have a fair comparison with simulations, the embedded radiation patterns of each finger (i.e., the EM simulated patterns of each finger taking into account the coupling with the neighboring fingers) have been considered, too. The comparison in Fig. 34(a,b) has been carried out by considering these data: the agreement is excellent. In Fig. 34(a), a  $\tau = 50 \text{ ns}$  shifts the maximum radiation to  $\theta = -30^\circ$  whereas Fig. 34(b) depicts the multi-beam capability for time-delays of  $30 \text{ ns}$  and  $150 \text{ ns}$ , resulting in the simultaneous radiation at both  $\theta = -20^\circ$  and  $\theta = 30^\circ$  within each time window. In fact, any desired pointing direction within the  $SR_{FDA}$  range is easily selected by adjusting the  $\tau_i$  parameters. Remarkably, this work represents the first experimental validation of single- and multi-beam radiation in a pulsed FDA, since most of the prior work done on FDA has been mainly theoretical.

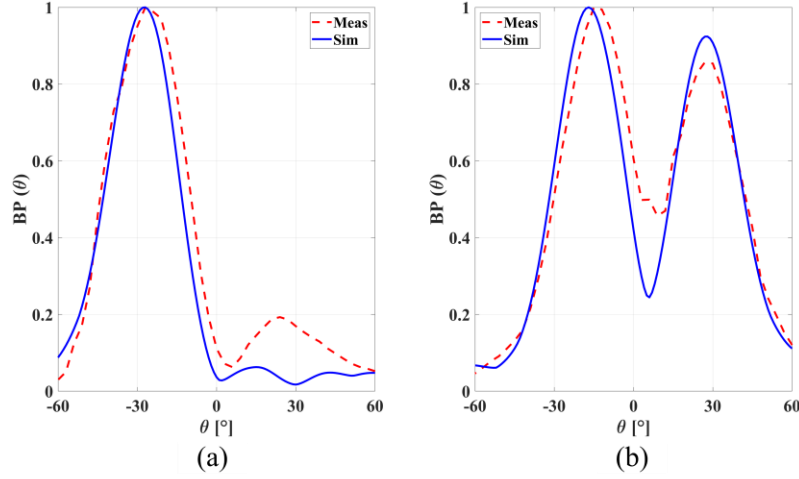


Fig. 34. Measurements vs simulations of the normalized multi-harmonic BP in the y-z plane for (a)  $I = 1$  and (b)  $I = 2$ . © 2024, IEEE

Once the peculiar dynamic radiation mechanism of the pulsed FDA has been demonstrated, its effectiveness in WPT applications should be verified by analysing the behaviour of a rectenna placed in the illuminated areas. To this end, an HB optimization of a rectenna, whose equivalent circuit is shown in Fig. 35, is carried out, by considering as input the actual multi-tone waveforms.

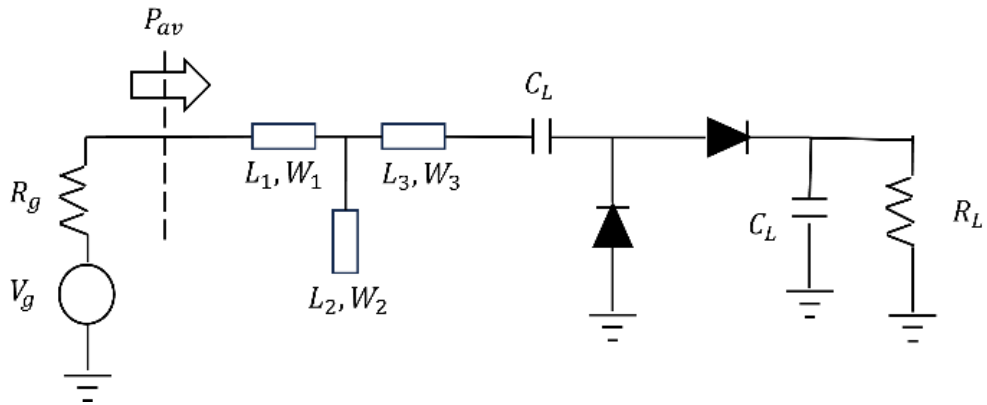


Fig. 35. Layout of the rectifier circuit of the receiving TAG. © 2024, IEEE

The circuit is realized on a 1.5-mm-thick ISOLA FR408HR ( $\epsilon_r = 3.68$ ,  $\tan\delta = 0.0092$ ). Such material revealed to be also suitable for the direct connection of the receiving antenna with the rectifier.

In particular, the HB optimization of the RF-to-dc efficiency ( $\eta_{RF-DC}$ ) of the nonlinear rectifier has been performed for an available power ( $P_{av}$ ) range of  $[-30 \div -5]$  dBm suitable for far-field WPT scenarios. To this purpose a single-tone CW, a 4-tone CW FDA, and a 4-tone TCFDA have been compared in a bandwidth of 100 MHz. In each case the optimum set of the design parameters is reported in Tab. 3. The input line is fixed ( $W_1 = 3.23$  mm and  $L_1 = 3W_1$ ) for matching the antenna impedance to 50  $\Omega$ , the capacitors are equal to 1 nF, and the diodes are Skyworks SMS7630-079LF.

Table 3

<b>Config.</b>	<b><math>L_2(mm)</math></b>	<b><math>W_2(mm)</math></b>	<b><math>L_3(mm)</math></b>	<b><math>W_3(mm)</math></b>	<b><math>R_L(k\Omega)</math></b>
<i>1-tone CW</i>	18.3	5	10.8	0.3	11.2
<i>4-tone CW FDA</i>	17.1	5	11	0.3	16.4
<i>4-tone TCFDA</i>	14.3	4.65	11.5	0.3	26.7

It is worth noting that, for a given average power  $P_{av}$ , the TCFDA yields the highest received PAPR because of the pulsed nature of the transmitted signal: this can be profitably exploited from the rectification point of view, as known from the literature [44]. From Fig. 36 one can see that at lower power levels the pulsed FDA rectifier excitation has slightly lower efficiency. For  $P_{av}$  above  $-14$  dBm, however, the performance of the TCFDA system surpasses both the 4-tone CW FDA and the single-tone CW cases. In addition, TCFDA enables flexibility in pulse waveform selection. Driven by the TCFDA HB analysis, various pulse shapes modulated with RF signals enable investigation into the rectifying performance. As can be seen in Fig. 37, there is a marginal but increasing improvement at higher power levels if triangular pulsed waveforms are used, contributing also to reduce transmission power loss and improving the definition of the spot illuminated, as has been mentioned in the previous section.

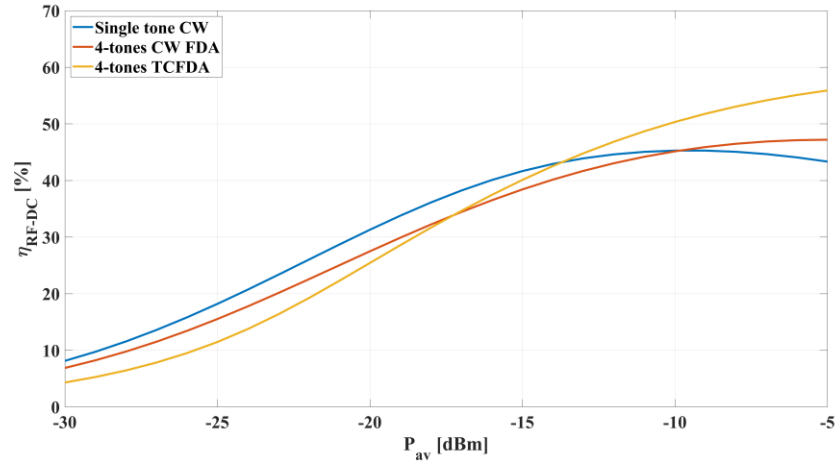


Fig. 36. RF-to-dc efficiency for different input excitations. © 2024, IEEE

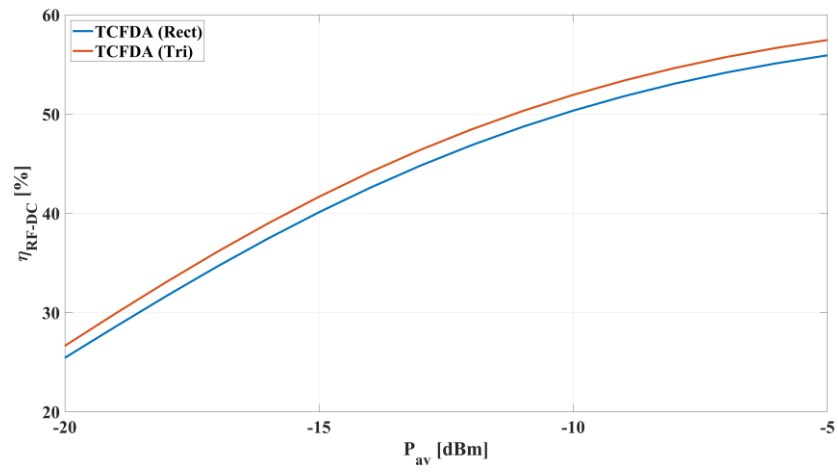


Fig. 37. RF-to-dc efficiency for different input pulse shapes for TCFDA. © 2024, IEEE

## 3. Time modulated arrays

This chapter is based on the following publications:

*E. Fazzini, T. Tiberi, A. Costanzo and D. Masotti, "Optimum Feeding Strategy for Agile Wireless Powering by Large, High-Directivity Time-Modulated Arrays," 2024 IEEE Wireless Power Technology Conference and Expo (WPTCE), Kyoto, Japan, 2024, pp. 142-145. © 2024, IEEE*

*T. Tiberi, L. Bastia, E. Fazzini, A. Costanzo and D. Masotti, "Agile Target Localization Via Time-modulation", submitted at 2025 19th European Conference on Antennas and Propagation (EuCAP), Stockholm, Sweden.*

### 3.1 State of art

Applications based on networks made up of low-cost and spatially distributed nodes or tags, such as logistics and industrial automation systems or wireless sensor networks, are innumerable in contemporary society. In this scenario, devices that are low-power and battery-free or rechargeable are increasingly under demand. Ambient RF energy harvesting represents one of the promising solutions to their energy autonomy challenge. However, the extremely low values of available RF power in real-world scenarios [45] determine, up to now, only a few microwatts for the collectable DC power [46], [47]. For this reason, WPT is becoming one of the pivotal technologies enabling an energy-aware world [48]; it will play a decisive role in the pervasive diffusion of the IoT paradigm [49],[50]. Within this context, the derivation of smart strategies aiming at intentionally feeding RF energy to many wireless nodes gains notable momentum [51]-[54]. Among the several available solutions the family of Time Modulated Arrays (TMAs) has been proposed for WPT applications by the research group of the University of Bologna and results one of the most promising.

The TMA belongs to a class of antenna arrays whose individual array element parameters are modulated with time. Such time-modulation provides a dynamic variation in the radiation pattern, which is desired for improving the performance of the array for specified applications. In a conventional antenna array, beam direction is controlled by adjusting the phase of the signals sent to every element. However, in TMAs, the ON/OFF timing of the array elements is modulated to adjust it without resorting to expensive phase shifters, but simply applying switching pulses to each element. The main concept is that by adjusting the activation time and duration of the pulses, the design of the radiation pattern of the array gains further degrees of freedom.

Time modulation was identified in the 1960s [56], [57] as an additional degree of freedom available in the design of ultra-low side lobe arrays. This technique is indeed more robust to errors when compared to traditional amplitude tapering but, unfortunately, it generates unwanted radiation in terms of additional sideband signals at integer multiples of the modulation frequency [58]. Indeed, several techniques have proved that time-modulated arrays can be designed for both side lobe reduction and sideband suppression by properly acting on switch modulation parameters. Additional degrees of freedom can also be exploited to take advantage of sideband radiation according to the following time-modulation schemes for harmonic beamforming [59], [60], direction finding [61], [62], adaptive nulling [63], [64], and beam steering [65], [66].

Most of the literature is concentrated on the creation, modification and optimization of the control sequences of the TMAs. It is noteworthy that four major types of time-sequences for switch control have been so far introduced: variable aperture size (VAS) [67], binary optimized time sequences (BOTS) [68], pulse shifting (PS) [69], and sub-sectional optimized time steps (SOTS) [70]. In the VAS method, "switch-on" time is common for all switches, and only the duration of excitation pulses for each array element is variable. A significant improvement in time-modulated array (TMA) performance comes from eliminating the common switch-on time constraint and introducing flexible switching strategies (BOTS, PS, SOTS), where the "switch-on" times of the elements can vary. In the BOTS approach, equal time intervals are considered in each modulation period of the switch. A binary genetic algorithm is employed to optimize the operation of the switches to derive their ON-OFF states

[68]. Techniques PS and SOTS further exploit extra design variables from pulse durations based on either single pulses (PS) or dividing each pulse into extra slots (SOTS). These latter approaches have also been extended by various optimization methods, including simulated annealing [71], particle swarm optimization [68], and differential evolution [70].

### ***3.2 Optimum Feeding Strategy for Agile Wireless Powering by Large, High-Directivity TMAs***

Numerous advanced optimization techniques have proven to be effective in designing TMAs radiation by utilizing the ON duration and the rise time of each switch as key design variables, as stated before.

However, the main limitation of the literature is that, despite the efficacy of the mentioned synthesis methods, little attention has been devoted so far to the real radiation patterns of the elements (typically considered as isotropic radiators during the synthesis), but mostly to the practical implementation of the control network. The latter problem becomes more difficult to solve when the number of radiating elements increases, especially in applications requiring high directivity values, such as highly selective WPT operations [72]. While the problem is still tractable in one-dimensional TMAs, no practical guidelines nor any implementation exists for time-controlled 2D-arrays.

In this work, to fill this gap, the radial topology previously presented in chapter 2.3 for FDA applications is exploited defining a simple multi-spoke planar TMA. For such a large number of antennas (24 in the proof-of-concept operating at 2.45 GHz) few switches at the spokes' input ports are needed (8 in this case) to easily control the time-based architecture. Finally, a basic optimization process using the MATLAB Optimization Tool is performed to verify the proposed layout for TMA. It is important to note that the goal of this research is only to test the effectiveness of the proposed layout as an agile TMA architecture, despite the low number of control variables, not to propose an optimization process, since there are many more advanced synthesis methods proposed in the literature, as previously written. The main

goal of this design is the first realization of the highly-directive and easily controllable 2D TMA.

Referring to Fig. 8(b) an array of ideal isotropic elements arranged with circular symmetry in  $M$  different rings grouped in  $N$  different spokes in the  $xy$ -plane is considered. This type of symmetry ensures unique radiation characteristics, including a well-defined illuminated spot and uniform behaviour across all vertical planes. To implement the time-modulated scheme, ideal switches (one for each antenna) are used to modulate the RF signal with a train of square pulses at a pulse repetition frequency  $f_p = \frac{1}{T_p}$ , in the MHz range. The signal radiated by the  $mn - th$  element can be cast as:

$$x_{mn}(t) = \sum_{h=-\infty}^{\infty} C_h^{mn} e^{j2\pi(f_0 + hf_p)(t - \tau_{mn})} \quad (26)$$

where  $C_h^{mn} = Ad_{mn} \text{sinc}(hd_{mn})$  is the Fourier coefficient of order  $h$  of the  $mn - th$  element, with  $A = 1$ ,  $d_{mn}$  and  $\tau_{mn}$  the duty cycle and the delay of the  $mn - th$  square pulse, respectively. The overall signal radiated in a generic far field position can finally be expressed as (recurring to (6) to compute the far-field distance):

$$x(t) = \sum_{m=0}^{M-1} \sum_{n=0}^{N-1} \sum_{h=-\infty}^{\infty} C_h^{mn} e^{\{j2\pi(f_0 + hf_p)(- \tau_{mn} - \frac{r_{mn}}{c})\}} \quad (27)$$

From the equation above, the well-known multi-harmonic radiation of TMAs can be identified, obeying to the following well-known rules [57]:

- The fundamental frequency ( $h = 0$ ) is unaffected by the delay values and will always radiate in a broadside direction. Its amplitude is determined solely by the duty cycle values.
- The higher harmonics ( $h \neq 0$ ) include a phase component that depends on the delay values, allowing for the steering of their radiation in any direction. Their amplitudes also depend on the duty cycle values.

Time modulation allows great flexibility in the radiation process: multi-harmonic radiation is possible, with each harmonic component characterized by different pointing direction and directivity. The TMA architecture is much simpler than the other array



topologies such as phased arrays. For instance, the beam steering with TMA can be realized with basic switches that are much cheaper than the phase shifters used in phased arrays, and than the SDR needed to create the multitone signals of FDAs. On the other hand, for highly-directive applications using the TMA as a smart radiator for WPT purposes [69], the control of the  $M \times N$  switches in the radial layout, or in a more conventional rectangular planar array layout, becomes rather impractically complex for feeding networks.

To deal with this practical problem, the proposed approach arranges the radiating elements into  $N$  groups of  $M$  elements, aligned along the  $n - th$  spoke, each forming one series-fed antenna array as shown in the radial layout. This will enable each spoke to be controlled by a single RF switch with several advantages including:

- the use of highly symmetric layout
- the inclusion of a large number of antennas
- a significant reduction in control network complexity
- a simpler feeding network design compared to an equally directive rectangular planar array.

It results, however, compared with the ideal but impracticable individual switching system, in a reduced number of degrees of freedom (ON duration and rise time of each switch) in the optimization of the radiation mechanism. This work shall illustrate how this trade-off leads to a feasible, but precise and highly reconfigurable radiator.

From the analytical point of view, the proposed arrangement is equivalent to consider just a single ring ( $M = 1$ ) in (27), and each element of the ring replaced by the embedded full-wave description of a series-fed array composed by  $M$  patch antennas, showed in Fig. 19(b).

To test the versatility of the proposed concept, a simple optimization was performed by using the MATLAB Optimization Tool. Since different design approaches have already been adopted with success for synthesizing TMA radiation properties, this work will not be focused on the optimization strategy itself. On the contrary, this activity aims at demonstrating how real-time reconfigurability in the case of high-directivity 2D beam steering of the desired harmonics can be easily achieved in the case of a practical and easy-to-implement circular topology.

The optimization goals are set for obtaining:

- a maximum of the first harmonic ( $h = 1$ ) only 4  $dB$  less than the fundamental one ( $h = 0$ )
- the steering of the first harmonic in the direction ( $\theta_t = 20^\circ, \phi_t = 0^\circ$ ). It is noteworthy that any direction in the 2D scanning plane ( $-60^\circ \leq \theta \leq 60, 0 \leq \phi \leq 360$ ) is available.
- The reduction of the amplitude of the higher harmonics ( $h \geq 2$ ) of at least 10  $dB$  in terms of power with respect to the first one.

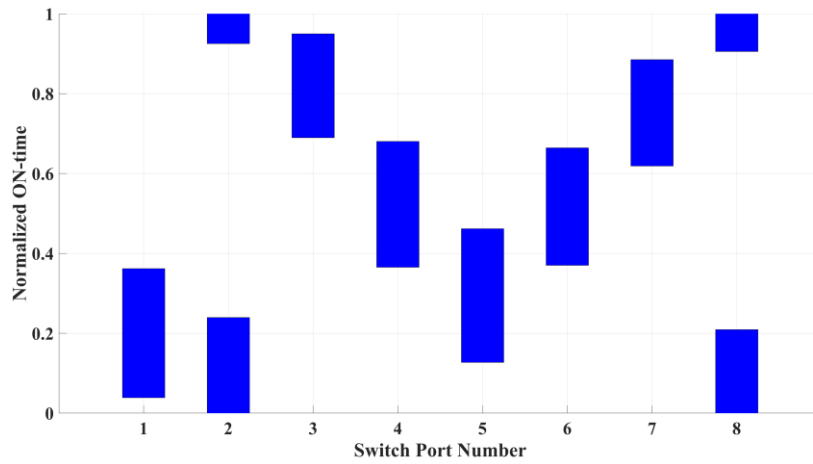


Fig. 38. Optimized control sequence.

The optimized duty cycles and delay values of the 8 switches, generating the excitation sequences shown in Fig. 38 satisfy the constraints, as witnessed by Figs. 39 and 40. In particular, the first harmonic points in the desired direction with a directivity equal to 13.02  $dB$ , that is only 3.72  $dB$  less with respect to the fundamental, as shown in Fig. 39. Also, the symmetric harmonic ( $h = -1$ ) is shown. As well-known from the literature this symmetric radiation can be suppressed at the cost of more complex waveform shaping [73].

Fig. 40 shows the maximum directivity (in  $dB$ ) of the first five harmonics, each radiating in a different direction. Notably, in the case of the second harmonic, there is a reduction of about 10  $dB$  with respect to the first harmonic and 14  $dB$  with respect to the fundamental. This difference further improves for harmonics higher than the second. It must be underlined

that the shape of the excitation pulse can be freely designed according to the application needs, depending on whether higher harmonics are to be employed.

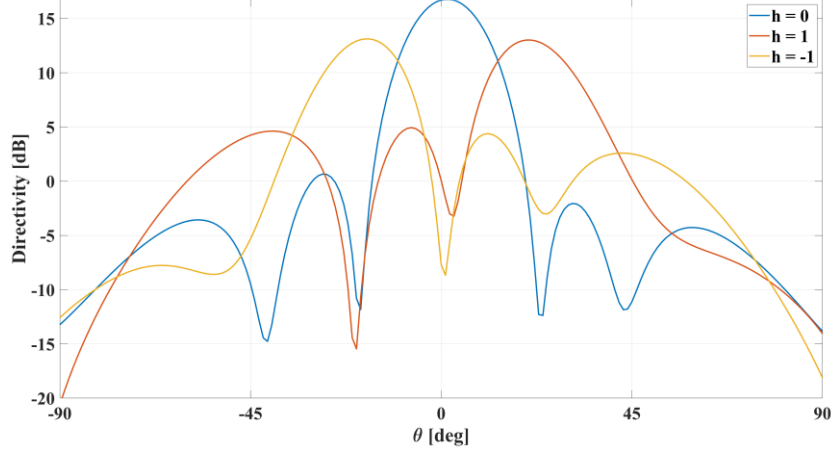


Fig. 39. Directivity in the  $\phi_t = 0^\circ$  plane for the fundamental and the first harmonics.



Fig. 39. Maximum directivity at different harmonics.

As already discussed, the optimization tool and the definition of the objective function are not necessarily the optimum ones; indeed, more effective design methods have been developed aiming at maximizing the duty cycles for granting higher values of the average directivity of the array over the modulation period [74]. However, the preliminary comparison hereafter reported gives an idea of the potential of the proposed radial topology when

combined with a time-modulation approach. This shows that effective and selective 2D steering in any pointing direction is possible, despite the limited degrees of freedom.

Note that, due to the circular symmetry, a rotation of the order of switch ports in the sequence represented in Fig. 38 scans the first harmonic beam to the same elevation angle ( $\theta = 20^\circ$ ), but in a new azimuthal plane ( $\phi = 45^\circ$ ). Similarly, any sequence which picks out a pointing direction  $(\theta_t, \phi_t)$  can be modified to point in a new direction,  $(\theta_t, \phi_t + p * 45^\circ)$  where  $p$  is the number of positions exchanged in the circular permutation. This represents another merit of the proposed layout with respect to a comparable TMA architecture with parallel series-fed antenna fingers, where one switch per finger is enough for radiation control. Hence an 8-fold reduction of optimized control sequences, which must be preloaded into the microcontroller driving the switches, is possible due to the use of the circular permutation rule [75].

As a conclusion, the arrangement of planar patch antennas in radial layout realizes a very directive array whose management is straightforward thanks to time-modulation techniques. This represents the first demonstration of a radial TMA realization: the circular symmetry facilitates the optimization procedure of the control sequences if compared with an equivalent multi-finger layout endowed with comparable complexity. Moreover, the provided result is obtained by means of a reduced number of active control switches (this improves the feasibility of the solution herein proposed) while keeping high reconfigurability and accuracy.

The goal of this work is to assess advanced capabilities of a specific, sophisticated array architecture relative to traditional linear arrays. Ideal switches with infinitesimal switch-on and switch-off times have been considered up to now. Further research will be devoted to the design of the architecture for experimental testing of the proposed TMA topology. In this work, these imperfect characteristics of the switches will be taken up and included in successive stages of analysis to study the whole performance.

### ***3.3 Agile Target Localization Via Time-modulation***

Following high reconfigurability for the radial topology using a time-modulated approach, an exploration on its usage is provided for localization purposes. A few of the advantages of a TMA system in radar-based localization are that it reduces hardware complexity and avoids the need for precise phase control, which usually is one of the issues in phased array systems. Even with such hardware improvements coupled with cost, the potential of TMA in these localization applications remains unexploited. Most of the previous works have been restricted to static array configurations for 1-D beamforming [75]. Innovations in 2D scanning and dynamic localization techniques remain open. This work explores the use of TMA in real time for target localization through exploiting its unique capabilities in harmonic beam steering and dynamic pattern shaping. A new radar-oriented application will be developed based on the recently introduced TMA architecture. This contribution will study different algorithms in developing a more complete framework for high-precision detections by using time-modulated signals. Simulations and experimental results will be provided showing the efficacy of TMA for target localization.

The decision to develop a TMA architecture for localization using a radial layout with a circular arrangement of radiating elements is driven by two key advantages:

- i) the use of a circularly symmetric layout ensures that the radiation pattern remains nearly unchanged across all azimuthal planes.
- ii) the control network's complexity is significantly reduced, thanks to the series-fed connection of the elements within each spoke.

The array design, shown in Fig. 18, consists of  $N = 8$  spokes, each with  $M = 3$  series-fed patch antennas operating at  $f_0 = 2.45 \text{ GHz}$ . The eight ports of the device are numbered as illustrated in Fig. 18(a).

In [62], the initial theoretical proposal for a TMA used for localization is introduced. This proposal leverages the radar mono-pulse principle and utilizes a linear array of closely spaced monopoles to minimize side-lobe effects during the localization process. In the current work, this concept has been extended and experimentally validated for a two-dimensional (radial) TMA, enabling a 2D localization process through an innovative approach based on power spectrum analysis. As described in [62], the localization process forms the first stage

of a two-step procedure. In the second stage, power transmission is carried out using the full antenna array to precisely target the previously localized tags.

This part of the research activity focuses exclusively on the localization phase. In this phase, the TMA transmits harmonic components of the input signal, with each harmonic potentially producing a different beam pattern. The localization algorithms, which are described later in this section, rely on comparing the beam patterns of the first-order harmonics to the one at the fundamental frequency. For a meaningful comparison, it is essential to have a stable and uniform radiation pattern (i.e., a broad half-power beamwidth) at the carrier frequency,  $f_0$ , which serves as a reference over a wide angular range where the target must be localized. Therefore, a low-directivity transmission pattern is required. This is achieved by using only two out of the eight spokes in the array configuration. The selection of which two elements to use for transmission is determined by the goal of producing a beam pattern that aligns with the system's objectives. It has been shown that combining adjacent elements results in a relatively flat beam pattern with minimal side lobes, which is well-suited for localization. This can be explained by the fact that adjacent elements ensure minimal spacing between their phase centers.

Referring to the coordinate system shown in Fig. 18, the antenna is placed in the  $xy$ -plane, and the localization system can scan a specific azimuthal plane ( $\phi$ -plane) due to the properties of the TMA. Furthermore, the advanced geometry of the array allows for scanning different planes by dynamically and selectively adjusting which of the eight time-controlled ports are activated for transmission. For now, the localization study is limited to a single plane. Specifically, ports P1 and P2 have been chosen, making the working plane the  $\phi = 0^\circ$  plane. However, it can be easily demonstrated that the scanning process can also be carried out in the  $\phi = 90^\circ$  plane by using a combination of two ports rotated by  $90^\circ$  (identified as P3 and P4).

At this stage, the two input ports are fed with an RF signal at a frequency of  $f_0 = 2.45 \text{ GHz}$ , time-modulated with a square pulse train with a pulse repetition frequency  $F_p = 5 \text{ MHz}$ . Under these conditions, the signal transmitted by the  $n$ th element can be described using Fourier series expansion:

$$x_n(t) = \sum_{h=-\infty}^{\infty} C_h^n \exp(j2\pi(f_0 + hF_p)(t - \tau_n)) \quad (28)$$

where  $C_h^n = Ad_n \text{sinc}(hd_n)$  is the Fourier coefficient of order  $h$ , with  $A = 1$  and  $d_n$  and  $\tau_n$  represents duty cycle and the delay of the  $n - th$  spoke, respectively. The total signal radiated by the array of 2 spokes can be written as:

$$x(t) = x_1(t) + x_2(t) \quad (29)$$

In accordance with the pulse settings outlined in [62], the ON-time of the sequences controlling the two ports is set to  $\frac{T_p}{2}$ , being  $T_p = \frac{1}{F_p}$ . In this way the total modulated signal  $x(t)$  consists of the fundamental frequency, which always transmits in broadside ( $\theta = 0^\circ$ ), and only the odd-order harmonics. The relative delay applied between the two pulses sets the pointing direction of the harmonic patterns (for  $h > 0$ ), and it is defined as:

$$\Delta\tau = |\tau_1 - \tau_2| \quad (30)$$

As an example, two complementary sequences have been selected with respect to the periodicity  $T_p$ , where  $\tau_1 = 0$  and  $\tau_2 = \frac{T_p}{2}$  ( $\Delta\tau = \frac{T_p}{2}$ ). A numerical simulation of the transmitted beam pattern  $BP = |x^2(t)|$ , which incorporates the embedded radiation patterns from the full-wave design of the radial TMA, is shown in Fig. 40(a).

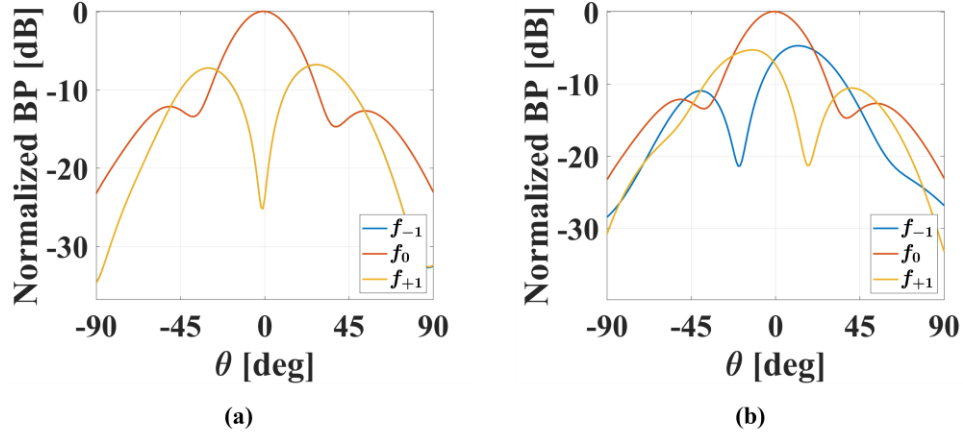


Fig. 40. Normalized BP on the plane  $\phi = 0^\circ$ : (a)  $\tau_1 = 0$  and  $\tau_2 = \frac{T_p}{2}$ , (b)  $\tau_1 = 0$  and  $\tau_2 = \frac{T_p}{4}$ .

It was expected that the fundamental harmonic (at  $f_0$ ) radiates in the broadside direction while the two first-order harmonics at  $f_0 \pm F_p$  have nulls in the same direction. This null in the radiation will be denoted as a "notch" henceforth.

Further analysis of this simulated model has brought out aspects which play a crucial role in the development of the localization algorithm. The notches of the positive and negative first-order harmonics are shifted in different directions by changing the relative delay  $\Delta\tau$  between the two pulsed signals. Moreover, the two notches are mirrored respect to  $\theta = 0^\circ$  (if the notch of the harmonic  $h = 1$  points at  $\theta = 30^\circ$ , the notch of the  $h = -1$  will point  $\theta = -30^\circ$ ). This characteristic allows the choice of a mutual delay between the two transmitted signals such that, for each  $\theta$ —direction, a different distribution of harmonic power across frequencies within the bandwidth of interest is retrieved and results very useful for localization purposes. As a general example, the results of the BP simulation for  $\tau_1 = 0$  and  $\tau_2 = T_p/4$  are presented in Fig. 40(b). Moreover, the simulated and measured amplitude spectra of the complete signal  $x(t)$  corresponding to various observation directions are shown in Fig. 41.



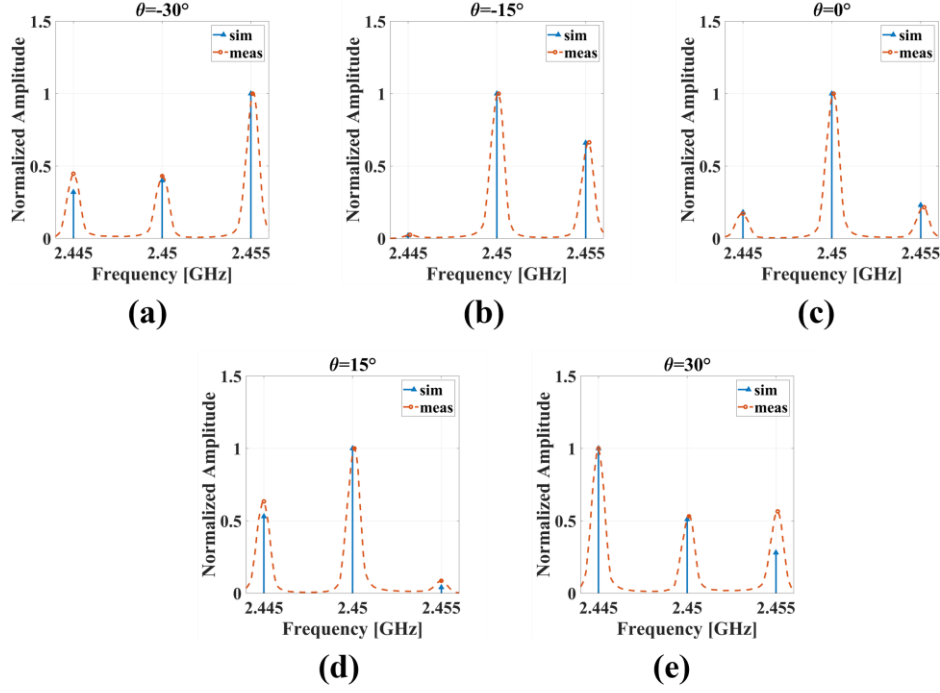


Fig. 41. Simulated and measured normalized amplitude spectrum on the plane  $\phi = 0^\circ$  in different directions

Measuring the amplitude contributions of the transmitted harmonics for different angles  $\theta$  in the plane of interest  $\phi = 0$ , each position corresponds to a distinct and unique spectrum. This confirms that localization algorithms capable of determining the position of an object based on the signal scattered by the target itself are potentially developable.

To ensure a unique correlation between signal parameters and target position  $\theta_t$ , two possible algorithms are proposed in the following sub-sections. These algorithms are based on the power ratio between the harmonic components of the received signal, requiring an estimation of the power levels at the relevant frequencies.

#### A. “Fixed Notch” Power Ratio

The first proposed algorithm operates on a single transmission of the TMA signal, which contains all the necessary information to determine the target's position. By analyzing the spectral components of the signal, two key quantities can be defined as:

$$\Delta_- = \frac{P_{-1}}{P_0} \quad (31)$$

$$\Delta_+ = \frac{P_1}{P_0} \quad (32)$$

$\Delta_-$  represents the ratio between the power of the first-order negative harmonic ( $P_{-1}$ ) and the power of the fundamental frequency  $P_0$ , while  $\Delta_+$  defines the ratio between the power of the first-order positive harmonic  $P_1$  and  $P_0$ . A numerical simulation was conducted where the notch of the pattern at  $f_0 - F_p$  was set at  $\theta = -20^\circ$  (while the notch at  $f_0 + F_p$  was positioned at  $\theta = 20^\circ$ ) setting  $\Delta\tau = \frac{T_p}{4}$ . The resulting  $\Delta_-$  and  $\Delta_+$  values have been calculated and plotted in Fig. 42. As can be evinced from the figure, the negative peaks of the power ratios are very sharp, and this can be favourably exploited for localization purposes.

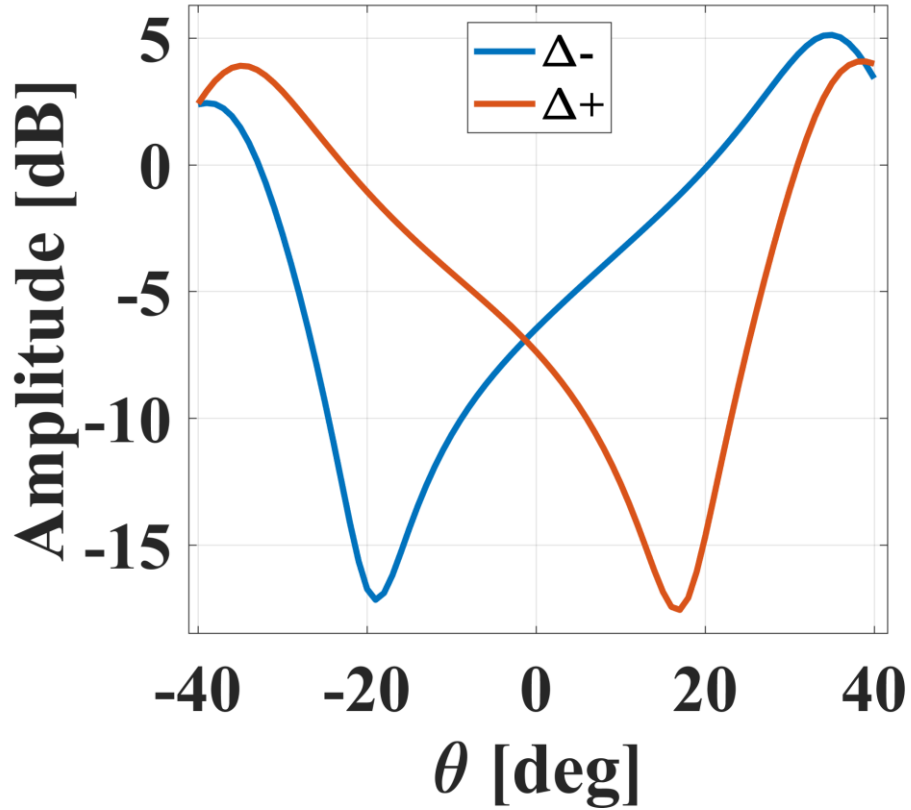


Fig. 42.  $\Delta_-$  pattern and  $\Delta_+$  pattern

From these curves, it can be noticed that the dominance of one delta pattern over the other is a function of the angle of observation: for negative  $\theta$ -angles, the  $\Delta_+$  curve dominates, and for positive  $\theta$ -angles, the  $\Delta_-$  curve becomes the reference for target detection. Fig. 42 shows that there is a unique correspondence between the amplitude and the direction in an angular range from approximately  $-35^\circ$  to  $35^\circ$  without ambiguity. It allows, in this way, to deduce with precision the angular coordinate of a target, having at disposal the exact values of the delta patterns. It is important to highlight that the precise values of these delta patterns can uniquely determine the target's coordinate, as they represent specific characteristics of the received signal. The narrow frequency spacing between the harmonic tones ensures that all three frequencies undergo similar attenuation and reflection, maintaining consistent ratios and allowing for accurate position determination. Consequently, the impact of AWGN noise on the power ratios used in the localization process is minimal.

The two  $x_n$  signals used in this algorithm require a constant relative time shift  $\Delta\tau$  between  $\frac{T_p}{2}$  and  $\frac{T_p}{8}$ , leading to a trade-off between the number of angles that can be scanned without ambiguity and the magnitude of the two deltas. When the time shift approaches  $\frac{T_p}{2}$ , the range of angles where the target's position can be accurately reconstructed is reduced. Conversely, if the relative delay approaches  $\frac{T_p}{8}$ , the delta curves become flatter, meaning they show less variation with changing observation angles, which makes the position detection more sensitive to noise and interference. These different scenarios will be discussed in the next section.

The main advantage of this algorithm is its ability to perform fast detection, making it especially useful for tracking moving objects. However, in harsh environments with narrowband interference, the expected correlation between power ratio values and position can be disrupted. To address this, an initial calibration of the environment could be necessary, and repeated measurements could be introduced to improve the accuracy of the localization process.

### B. “Moving Notch” Power Ratio

This algorithm is based on a set of measurements for which there are different delays  $\tau_1$  and  $\tau_2$ , such that the difference  $\Delta\tau$  ranges in the interval from  $\frac{T_p}{8}$  to  $\frac{T_p}{2}$ . For each measurement, a pair of deltas ( $\Delta_-$  and  $\Delta_+$ ) are computed, considering that notches of the first-order harmonics shift depending on the selected delays. When a notch falls into alignment with the target's position, that harmonic's contribution will be very close to zero and yield a minimum in the delta pattern. In this way, the system can uniquely determine the target's position, with this type of detection relying on identifying the minimum of a specific harmonic component. Contrary to the previous approach, the localization of negative  $\theta$  –angles makes use of the  $h = -1$  term, whereas for the positive  $\theta$  –angles, the term  $h = 1$  is used.

In practice, not all angles can be singularly scanned given the huge amount of computational time. An iterative methodology might be used where several sectors are scanned and, in real time, the harmonic levels are monitored. Once a minimum in a specific harmonic has been detected, further iterations around that position can refine the exact position of the target. This approach, while leading to longer localization times, takes full advantage of the possibility given by the TMA of shifting the notch and is more accurate than the previously described algorithm. However, this very accuracy could also turn out to be a problem since moving objects can give inconsistent data. However, the localization capability of the proposed TMA in this work for a fixed target position can be validated and future works can address all those complexities that might arise when tracking a moving object.

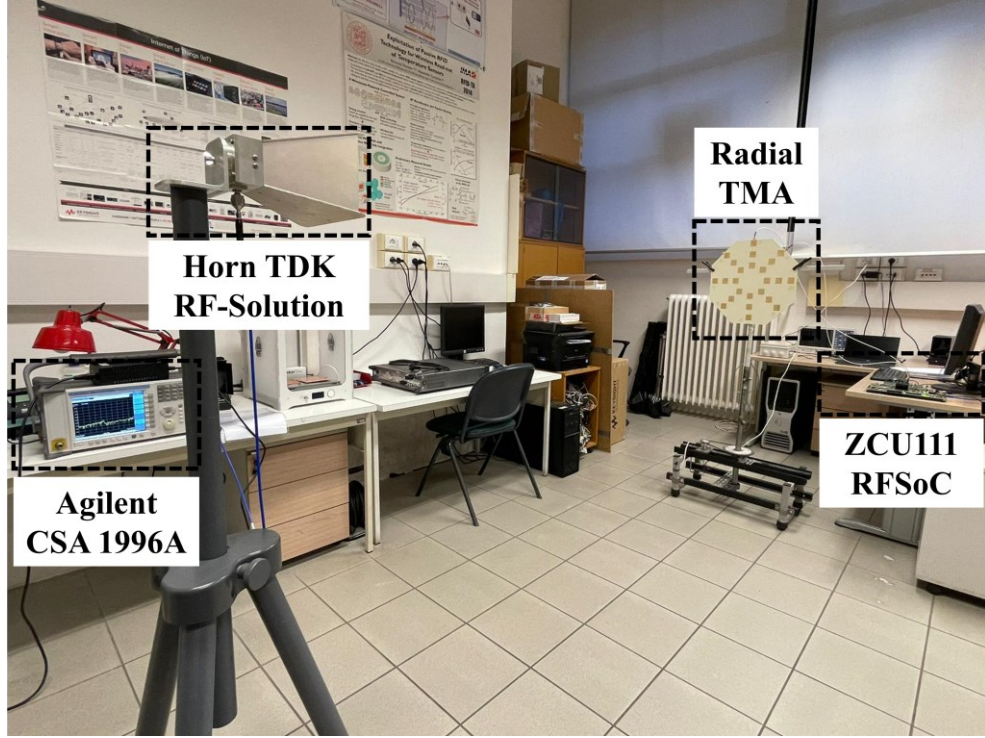


Fig. 43. Measurement set-up

In the indoor laboratory environment, the proof-of-concept of the TMA localization system has been demonstrated. The measurement setup is shown in Fig. 43. The two RF signals were generated by using a Xilinx RFSoc ZCU111 software-defined radio. These signals were fed into ports P1 and P2 of the transmitting array. The receive setup was completed with a TDK RF Solutions HRM-0118 horn antenna connected to an Agilent CSA Spectrum Analyzer N1996A with resolution bandwidth of 200 kHz.

Table 3

Use case	Duty cycle $d_n$	Relative delay $\Delta\tau$	Notch position
a	50 %	$\frac{T_p}{2}$	$\theta = 0^\circ$
b	50 %	$\frac{T_p}{4}$	$\theta = \pm 20^\circ$
c	50 %	$\frac{T_p}{8}$	$\theta = \pm 30^\circ$

Power distribution was measured over the three frequencies  $f_0 - F_p = 2.445 \text{ GHz}$ ,  $f_0 + F_p = 2.455 \text{ GHz}$  and  $f_0 = 2.45 \text{ GHz}$ , in the plane  $\phi = 0^\circ$  for the experimental derivation of  $\Delta_-$  and  $\Delta_+$  curves. Three different use cases summarized in Table 3 are considered, corresponding to a specific relative delay between the transmitted signals. Good agreements between simulated and measured curves have been obtained in all cases, as shown in Fig. 44.

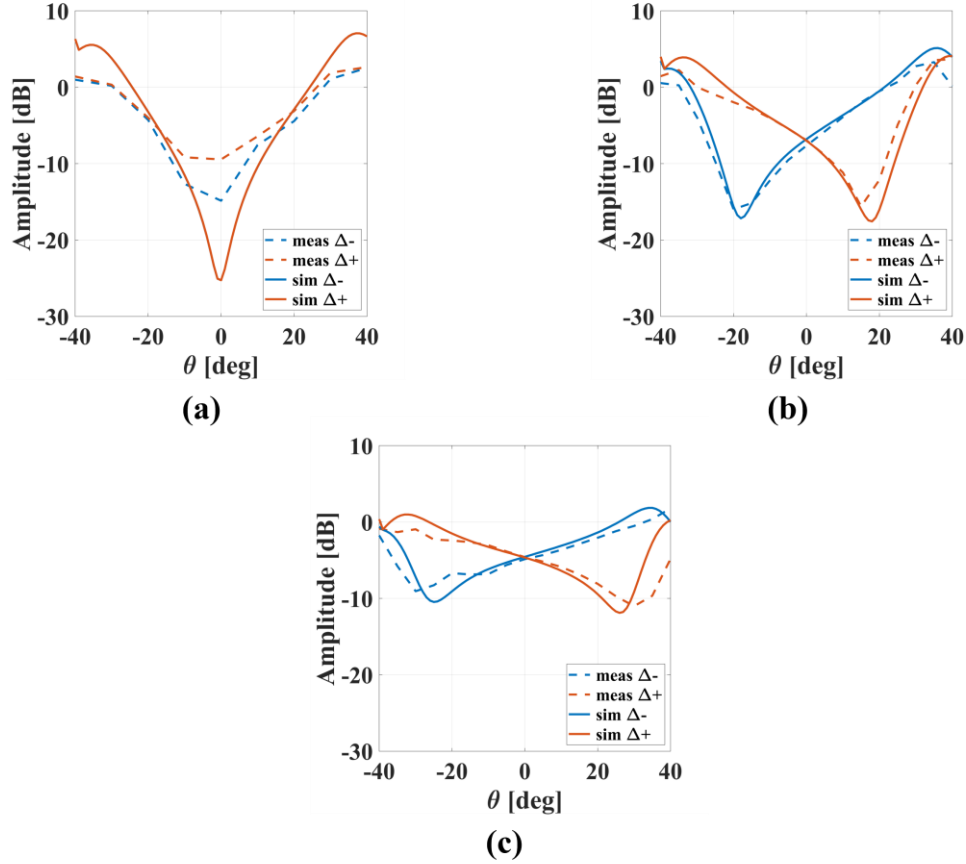


Fig. 44. (blue continuous line) simulated  $\Delta_-$  pattern, (blue dashed line) measured  $\Delta_-$  pattern, (red continuous line) simulated  $\Delta_+$  pattern, (red dashed line) measured  $\Delta_+$  pattern measured for (a)  $\Delta\tau = 100 \text{ ns}$ , (b)  $\Delta\tau = 50 \text{ ns}$  and (c)  $\Delta\tau = 25 \text{ ns}$

From the received spectrum and the consequently derived curves, it is possible to estimate the target position exploiting the two algorithms previously presented. In the “Fixed Notch” Power Ratio case only one transmission takes place and from the scattered signals the target direction can be computed thanks to its unique relation with deltas. On the other hand,

a collection of data moving the notches can be retrieved for improving the accuracy exploiting “Moving Notch” Power Ratio algorithm.

As a summary, the first algorithm offers a very fast detection and find a crucial rule for real-time localization of moving objects, while the second demonstrates superior accuracy by exploiting the full reconfigurability of the TMA, resulting also more insensitive to interference issues. Further research is needed to explore the multi-dimensional scanning capabilities of the array and to deal with the scattering from a real target. Overall, this work lays the groundwork for advancing TMA-based localization, with opportunities for future improvements and innovative systems based on the presented approach.

## 4. Railway Signaling and Positioning System

This chapter is based on the following publications:

*G. Paolini, E. Fazzini, S. Trovarello, D. Amato, D. Masotti and A. Costanzo, "A 2.4 GHz Modular Antenna System for Train Integrity and Localization Purposes," 2023 IEEE 13th International Conference on RFID Technology and Applications (RFID-TA), Aveiro, Portugal, 2023, pp. 221-224. © 2023, IEEE*

*G. Paolini, E. Fazzini, S. Trovarello, D. Amato, D. Masotti and A. Costanzo, "An Innovative Multi-Port LoRa-Based Wireless Node for Railway Signaling and Positioning," in IEEE Journal of Radio Frequency Identification, vol. 8, pp. 618-626, 2024. © 2024, IEEE*

### 3.4 Introduction

Since the dawn of time, railway security and monitoring have formed part of the most complex challenges in the transport sector. Nowadays, innovative solutions using wireless technologies for train integrity and localization are being explored to provide more agile and secure methods. Some recent examples are the GNSS already tested to detect virtual balises [76] and the ERTMS, shown in Fig. 45. It can enable all trains to continuously and reliably monitor themselves by broadcasting data regarding their integrity [77], [78] and real-time positioning [79], [80]. Recently, it has also been shown that another application of the GNSS system could be realized by combining satellite communication with real-time data from RTK sensors of the train, such as its velocity [81].



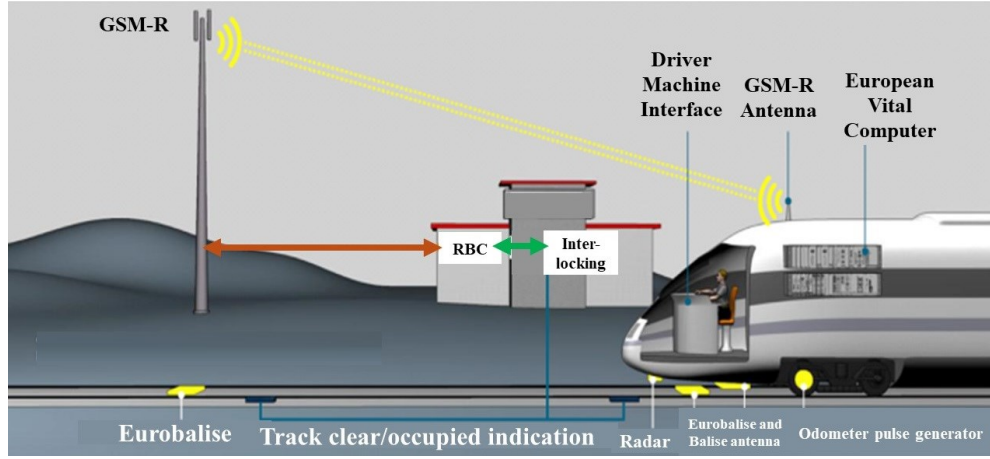


Fig. 45. Current scenario for high-speed networks for railway signaling and positioning following the European railway traffic management system/European train control system (ERTMS ETCS), denoting with GSM-R the global system for mobile communication in railways, and with RBC the radio block center. © 2024, IEEE

Other promising methods for increasing the efficiency, reliability, and safety of GNSS-based train localization systems are presented in [82], [83]. These works propose an architecture to incorporate GNSS data with inertial navigation systems to attain redundancy and improve positioning accuracy by using GNSS signal errors. Beyond satellite communication, solutions provided by the vehicle-to-everything (V2X) domain are also applicable to the railway environment for the purpose of locating and monitoring the integrity of trains. Various research groups have studied different wireless communication technologies such as Long Range (LoRa), Zigbee, Wi-Max, and 4G to consider an appropriate architecture that will provide a stable connection regarding V2X communication applications. Among these protocols, LoRa has been highlighted as the most promising one for smart transportation because of its long-range and low-power consumption features. Even if LoRa is extensively studied, up to now its performance in V2X communication scenarios has been seldom explored. In [84], various LoRa schemes with different parameter settings were simulated in typical V2X communication conditions for BER performance, showing that it has the potential to meet the increasing connectivity demands of vehicular networks. The work in [85] tested LoRa in a real-world scenario by proposing a low-power, reliable architecture for mobile vehicles. Of greater importance, [86] adapted LoRa to the railway

sector, proving that it can establish high-speed communication channels between moving LoRa gateways on trains and sensors along the railway.

LoRa is performing well under conditions considered unfavorable, like during movements of the devices. Research works [87] and [88] validate the feasibility of LoRa for V2X communications; those have a great potential for improving traffic safety, vehicle networking, and network control. Additionally, its hardware is very cheap, so this can be a scaling solution. Considering that devices are placed outdoors, effects of weather on the 2.4 GHz radio link should be considered too. Research [89] investigates the impact of meteorological conditions on the performance of 2.4 GHz networks from which can be concluded that with respect to this radio link, in terms of weather, frequency 2.4 GHz results a good competitor if compared to more traditional frequencies (433 or 868 MHz). Recently, LoRa was also shown to support broadcasting of real-time kinematic (RTK) messages for multiple devices, which can perform high-precision localization with very low power consumption [90].

## ***4.2 An Innovative Multi-Port LoRa-Based Wireless Node for Railway Signaling and Positioning***

As a side activity of the thesis work, the experience made in the design of radiating systems has been exploited for the design and realization of a new system with three co-located antennas to be adopted as part of a new wireless network architecture for wagon-to-wagon and wayside railway communication, in the framework of a regional project for the safety improvement of secondary railway lines POR-FESR 2014–2020. The present system is aimed at proposing simple, low-cost, and accurate solutions for monitoring the integrity of trains and their position in secondary railway systems when GNSS and ERTMS infrastructure are not available. Additionally, this work outlines the network architecture and relevant scenarios, describing in detail both the numerical and the experimental analysis of the three-element antenna system, tested in free space and under more realistic conditions, including the presence of large metallic obstacles like train wagons. The characterization of the LoRa

network will be provided, presenting results of real measurements performed with a running train along a secondary railway line.

Presently, in the case of Italy, only about 4.8% of the entire rail network, consists of high-speed lines employing the ERTMS ETCS Level 2 system fitted with a radio block center for the purpose of train spacing. The limited spread of these systems is mainly due to the high cost involved for installation, management and maintenance. The lack of cost-effective and robust solutions increasingly heightens the need for monitoring and preserving lower-traffic, secondary railway lines to ensure reliable train localization and spacing on these routes.

The primary goal of the project will be to develop a simple and low-cost architecture for a network able to achieve precise tracking of the trains on the secondary lines while their integrity is monitored. The envisaged solution consists of low-power, low-cost sensor nodes installed on each train wagon and on intelligent poles placed every 250 meters along single-track railways. The current design (Fig. 46 and Fig. 47) focuses on convoys from one to four wagons (future studies will be devoted to longer trains of up to ten wagons). The section of railway considered in this study is about 30 km long, with the route having around 120 intelligent poles distributed for localization, equipped with the same node technology as the wagons. In this way several trains could be managed on secondary railways at the same time, whereas hitherto it has been seriously restricted due to lack of precise localization data.

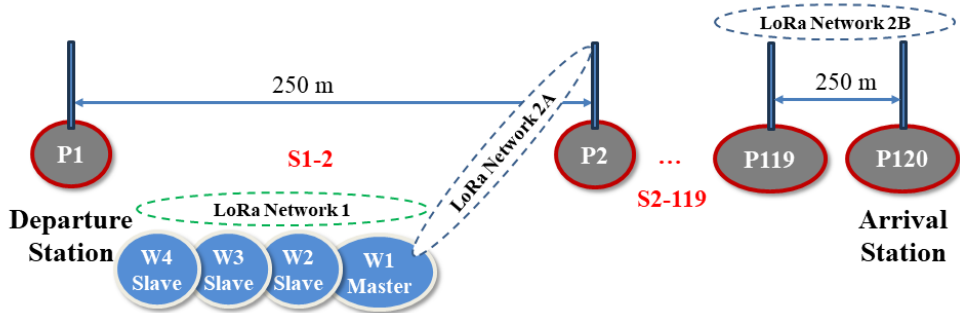


Fig. 46. Schematic diagram for the architecture of Network 1, 2A, and 2B in normal conditions. © 2024, IEEE

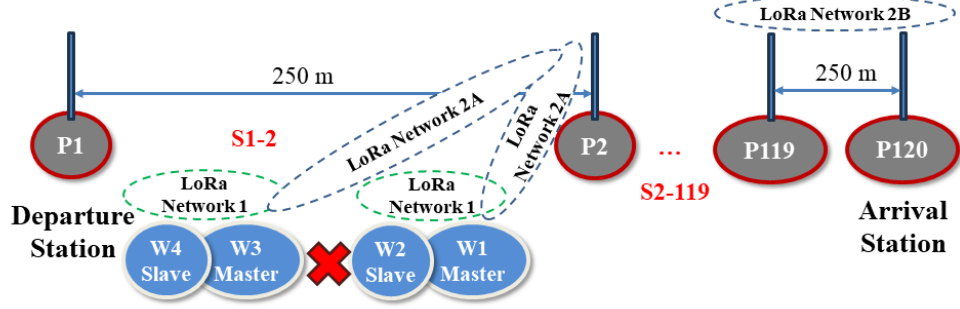


Fig. 47. Schematic diagram for the architecture of Network 1, 2A, and 2B in case of train integrity loss between W2 and W3, with consequent generation of a new Network 2A with two Masters. © 2024, IEEE

For the purpose of this study, LoRa protocol working at  $2.4\text{ GHz}$  has been chosen to support both communications for train integrity (Network 1) and for localization (Networks 2A and 2B), as it is a protocol characterized by low-power consumption, robustness, and high sensitivity (up to  $-129\text{ dBm}$  input signal). Network 1, shown in Fig. 2, establishes the communication of the wagons of a train, in which the first wagon will be defined as the "Master" and all the rest of the wagons as the "Slaves." This communication is made using the industrial, scientific and medical (ISM) band at  $2.4\text{ GHz}$ , chosen to minimize the size of the radiating elements. Although electromagnetic waves at this frequency experience higher path loss compared to lower frequencies such as  $433$  or  $868\text{ MHz}$ , the signal-to-noise ratio (SNR) of this application is predicted to be as high as  $30\text{ dB}$ , sufficient to ensure successful signal demodulation.

In Network 1, each wagon is equipped with two horizontally polarized directive patch antennas, called WWDAs (Wagon-Wagon Directive Antennas), in which one antenna is used for communication with the preceding wagon and another with the following one. These antennas can either be installed inside or outside the train.

Network 2A involves the communication between the "Master" device in the train and the LoRa nodes equipped in type-A intelligent poles for the train localization. As the direction of the train cannot be known beforehand, omnidirectional antenna needs to be installed on both the train and poles (Port P1 in Fig. 48(b)) to provide good enough communications, maintaining the BER less than  $10^{-3}$ . For this purpose, a vertically polarized (and cross-

polarized with respect to WWDAs) monopole antenna is assumed here and named as WPOA (Wagon-Pole Omnidirectional Antenna).

If integrity loss of the train happens, the first wagon of the detached section will become the new "Master" in contact with the intelligent pole. If, for example, wagon W3 and W4 detach from W1, W3 will be the "Master" for the detached section and will be in communication with the Type A poles, as depicted in Fig.47.

Finally, Network 2B allows type-A and type-B intelligent poles to communicate. In this link, omnidirectional antennas are used for type-A poles, while type-B poles use directive antennas since they must collect information coming from several type-A poles and are normally placed near the stations. These type-B poles can communicate directly with the train wagons when the train is at a station, and they result the nearest to the convoy.

Copper	(L1)	Thickness: 0.035 mm
Rogers RO4350B	(Inner Layer #1)	Thickness: 1.52 mm
Copper	(L2)	Thickness: 0.035 mm
FR4	(Prepreg)	Thickness: 0.035 mm
Copper	(L3)	Thickness: 0.035 mm
Rogers RO4350B	(Inner Layer #2)	Thickness: 1.52 mm
Copper	(L4)	Thickness: 0.035 mm

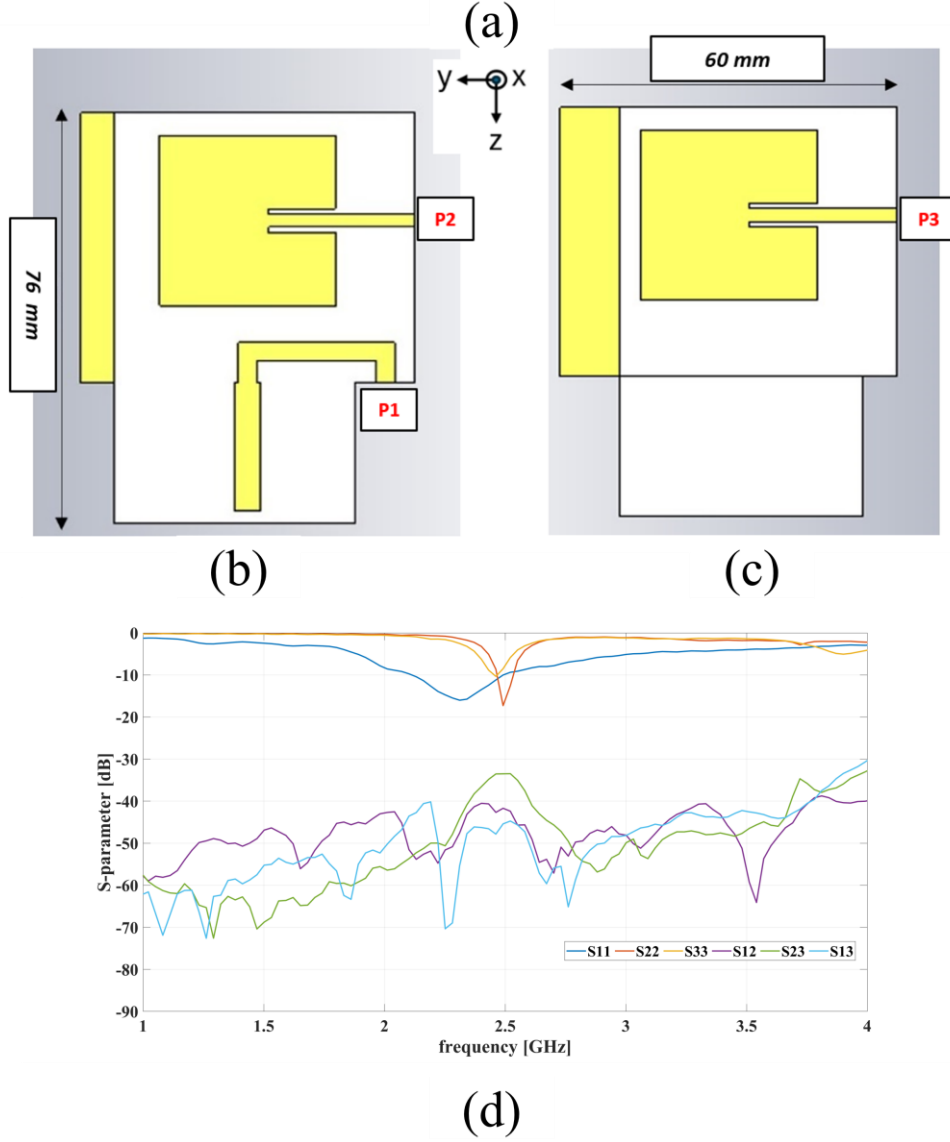


Fig. 48. (a) Stack-up of the prototype; layout of the (b) front and (c) back layers; (d) measured S-parameters of the multi-antenna prototype in free space. © 2024, IEEE

The main challenge of this design is the co-localization of the antennas in a small footprint by guaranteeing good enough radiation performance and isolation. In order to meet these requirements, the adopted choices are described in the following.

The multi-port LoRa transceiver was designed on Rogers RO4350B substrate, whose dielectric constant is 3.66 and thickness equals  $1.52\text{ mm}$ , and the double-layer stack-up had an overall dimension of  $76\text{ mm} \times 60\text{ mm}$  as illustrated in Fig. 48(a). As a matter of fact, the two layers are exploited to host the radiating elements: on the top layer, there is the WPOA (monopole antenna, Port 1: P1) and the first WWDA (patch antenna, Port 2: P2), while on the bottom layer the second WWDA (patch antenna, Port 3: P3) is placed. In Figs. 48(b) and 48(c), the front and the bottom views are shown, respectively. The two Rogers laminates were joint together by using an FR4 prepreg for bonding, thickness  $35\text{ }\mu\text{m}$ .

S-parameters characterization and radiation pattern measurements were performed in free space to validate the design and simulations were carried out using the CST Microwave Studio software. It is relevant to mention that the back-to-back configuration of the two patch antennas P2 and P3 has been chosen to optimize the decoupling between the two horizontally polarized antennas operating at the same frequency. The maximum measured value of the  $S_{23}$  transmission coefficient was  $-33\text{ dB}$  at  $2.46\text{ GHz}$  as shown in Fig. 48(d).

Due to the application, the radiating structure must be simulated in a realistic environment to consider unwanted effects or degradation in performance. As expected, the tri-port module operating at  $2.45\text{ GHz}$  with the LoRa protocol is intended for operation outside a moving train to grant the best line-of-sight to both Network 1 and Network 2. However, the performance of the module considerably depends on the environment in which it is placed. The main factor interfering with the ideal operation of the radiating elements is the presence of the metallic plates representing the train's wagons. Due to its ungrounded nature, the most affected antenna is expected to be the monopole. In contrast, the patch antennas should be less influenced by the wagon walls because their metallic ground acts like a shield.

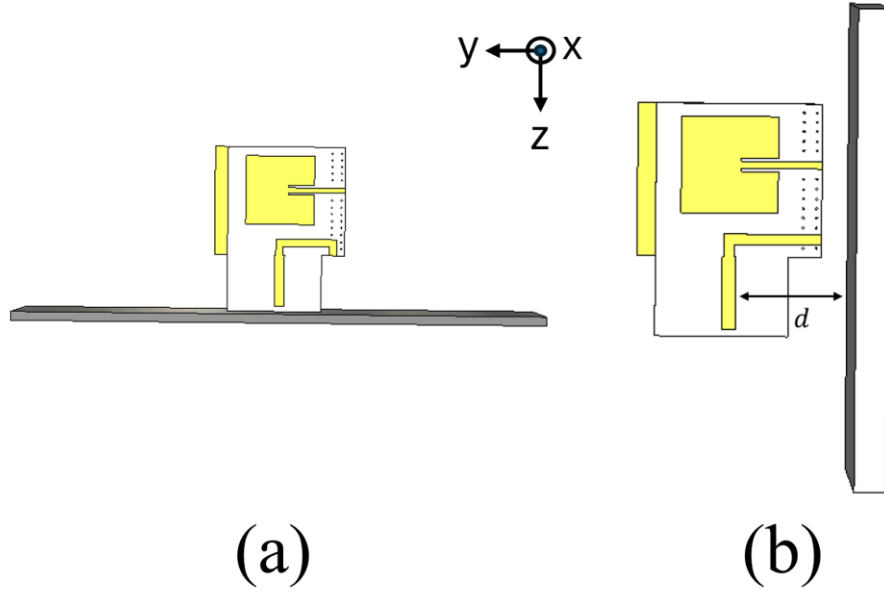


Fig. 49. (a) Simulation setup with the module on the top of the wagon; (b) simulation setup with the module next to the wagon. © 2024, IEEE

To quantify and evaluate such an effect, simulations of the tri-port antenna module including metallic layers emulating the wagon walls have been performed. A  $120 \times 120 \times 4 \text{ mm}^3$  PEC plate has been modelled in two scenarios as depicted in Figs. 49: in the first one the module is placed on the top of the wagon with the plate beneath it, as showed in Fig. 49(a), while in the second one the module is fixed on the side wall of the wagon with the plate beside it, as depicted Fig. 49(b).



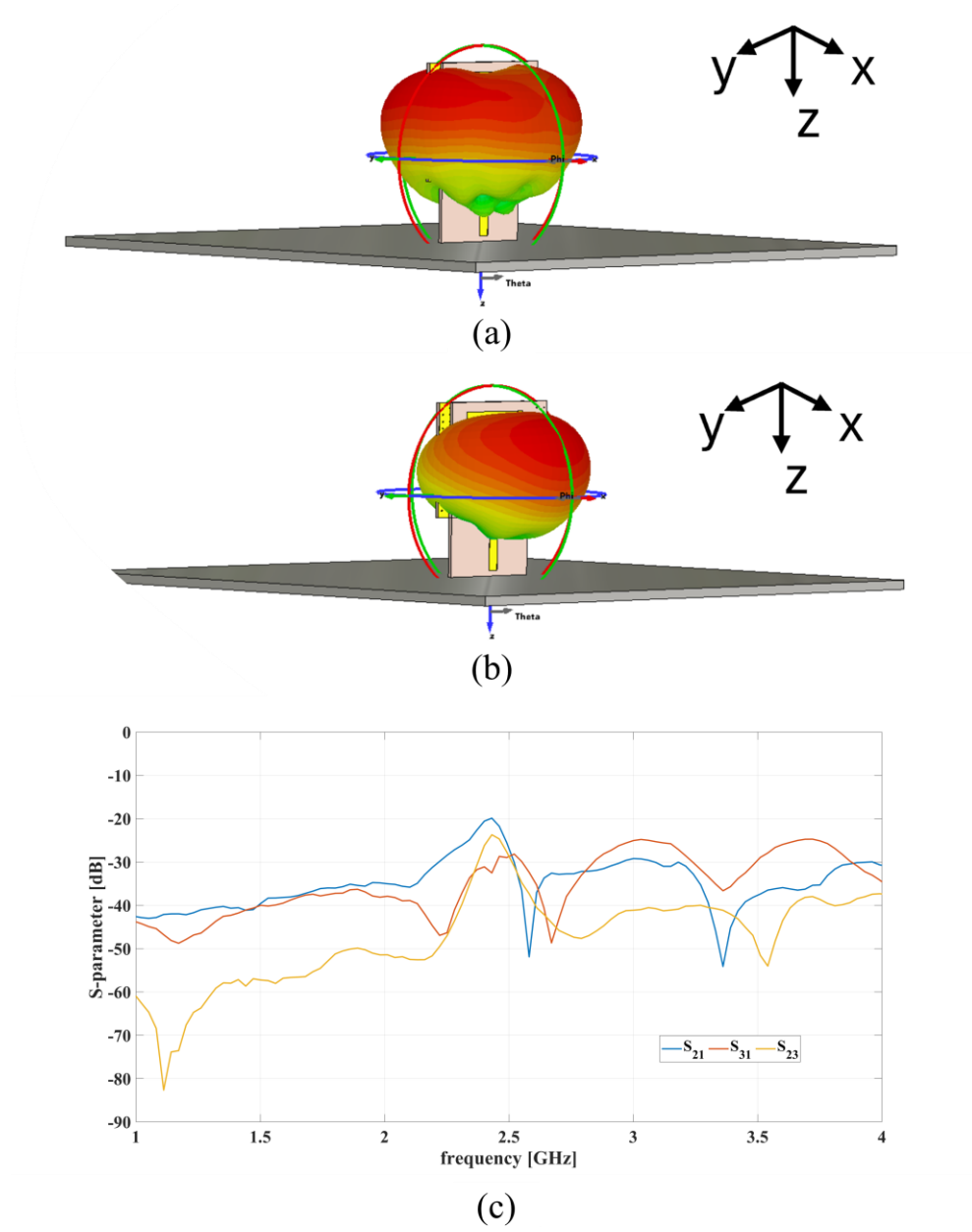


Fig. 50. (a) Tridimensional radiation surfaces (realized gain) of (a) P1 and (b) P2, and (c) measured transmission coefficients for the prototype placed on the top of the metal plate. © 2024, IEEE

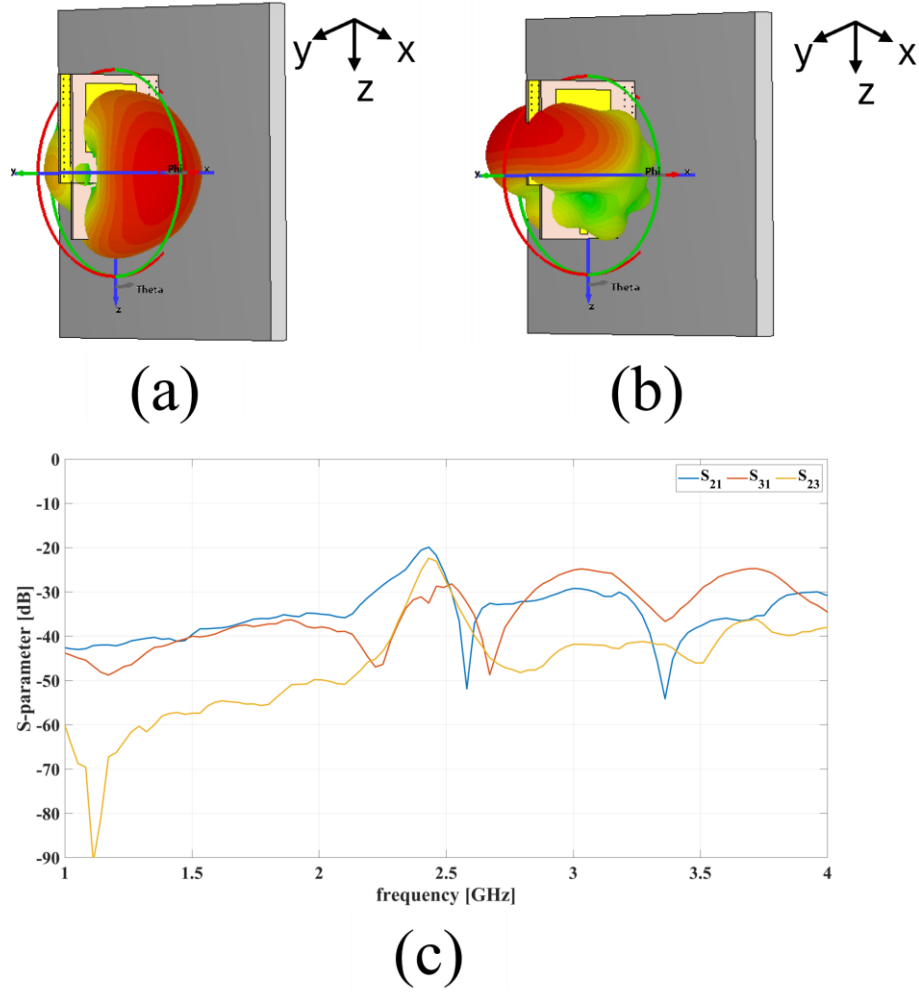


Fig. 51. (a) Tridimensional radiation surfaces (realized gain) of (a) P2 and (b) P1, and (c) measured transmission coefficients for the prototype placed alongside the metal plate. © 2024, IEEE

For the first scenario, the simulation results of the patch antennas (WWDAs) of Network 1 show that the radiation surface has a deflection of  $30^\circ$  in elevation away from the metal plate due to PEC plate, as seen in Fig. 50(a). The maximum obtained gain was  $8 \text{ dBi}$  with an HPBW of  $50^\circ$  and accordingly this resulted in an effective solution for train integrity. On the other hand, the presence of the PEC layer has strongly affected the performance of the monopole antenna, since it suppresses radiation in the half-space below the plate. Correspondingly, the maximum realized gain was  $5.7 \text{ dBi}$  for an elevation deflection of  $40^\circ$  while the HPBW became  $43^\circ$ . This is still a quite good solution, since the antenna will provide

communication with intelligent poles which are normally higher than the top of the wagons. Fig. 50(b) presents the radiation surface obtained for WPOA.

For the second scenario, several configurations have been tested changing the distance  $d$  of the module from the wagon's side wall. For the monopole antenna, in particular, the presence of a PEC plate parallel to its vertical axis could cause serious interference if not correctly placed. From electromagnetic theory, it was confirmed that the optimal performance occurs when this distance is set to a quarter of the wavelength ( $d = \frac{\lambda}{4}$ ), since the wall behaves as an ideal reflector and helps to focus the radiation pattern of the WPOA toward the desired half-space of the intended link. It can be observed from Fig. 51(a) that this setup provides  $30^\circ$  deviation in the elevation plane, while offering the maximum gain of  $8.8 \text{ dBi}$  and HPBW of  $44^\circ$ . From the results of simulation of the patch antennas of Network 1, PEC plane does not strongly impact their 3D radiation pattern. They feature a typical radiation orthogonal to the patch plane with a maximum gain of  $6.3 \text{ dBi}$  and HPBW equal to  $97^\circ$  shown in Fig. 51(b).

By comparing the above two configurations, a preliminary conclusion can be drawn. WWDAs are responsible for the integrity of the train and use two patch antennas oriented face-to-face. In this case, the optimal configuration was placing the module laterally on the wagon wall. In fact, this configuration provides higher gain with broadside radiation. In the case of the WPOA, which provided communications with intelligent poles positioned higher than the wagon, both scenarios worked effectively. The first configuration is more flexible because communications can be made in either half-space w.r.t. the direction of the train, while the second configuration restricts communication in one half-space. However, the second setup was chosen due to easier installation, and some corresponding field measurements will be discussed later in this chapter.

Since antennas are installed outdoors, environmental conditions such as rain, dust, and ice will be disadvantageous to their performance, degrading the matching between the antennas and LoRa device or disrupt the radiating patterns of the modular tri-antenna system. As protection, a plastic enclosure has been considered. The case is fabricated using polylactic acid PLA, the common feedstock material in 3-D printing. The electromagnetic properties of the case were characterized using the T-resonator technique in the frequency range between  $10 \text{ kHz}$  and  $6 \text{ GHz}$ . The matching between simulations and measurements revealed that the

case electromagnetic performance are  $\epsilon_r$  of 2.64 and a  $\tan(\delta)$  of 0.018 at 2.4 GHz. In designing the case, consideration was given to housing the 3-port antenna system; thus, different PLA thicknesses were analysed. A thickness of 3 mm was opted due to the sufficient mechanical strength with minimal detuning effect on the radiation characteristic of the antennas. The case is designed with interlocking joints for ease of assembly and presents three holes for RF cable connections to the LoRa device.

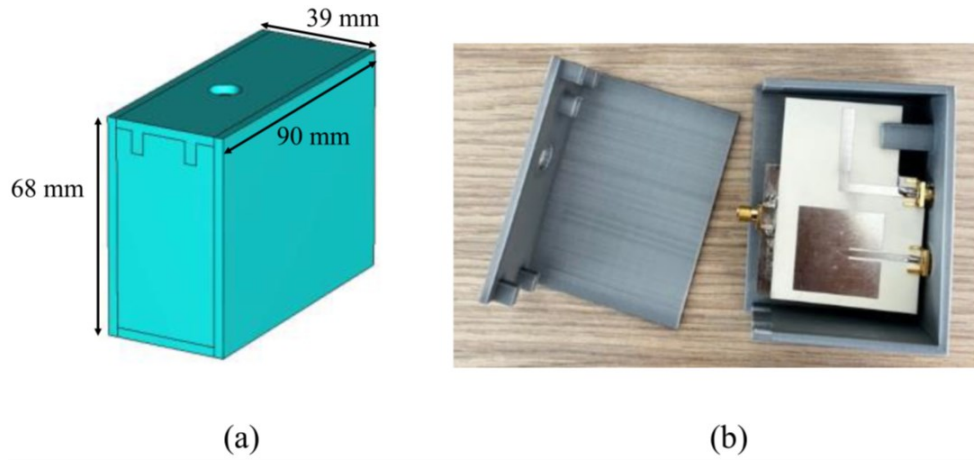


Fig. 52. (a) 3D view of the simulated case with its dimensions, and (b) photo of take apart fabricated prototype. © 2024, IEEE

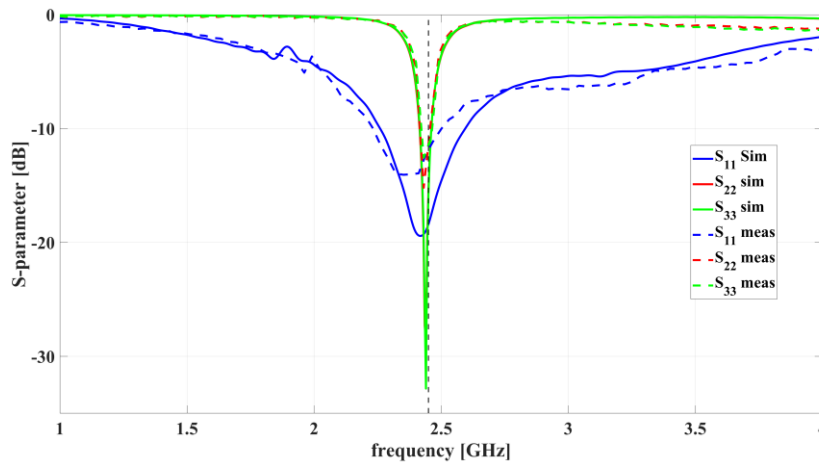


Fig. 53. Comparison between simulated and measured reflection parameters of the tri-port antenna system protected by the PLA-case. © 2024, IEEE

Fig. 52 present the 3D simulation next to the real 3D-printed PLA case, with a size of  $68 \times 90 \times 39 \text{ mm}^3$ , and guarantees antenna protection without compromising system performance. The antenna in the case was measured with the Agilent N9923A FieldFox VNA. As shown in Fig. 53, EM-simulated results are compared with the measurement: just a difference in the deepness of the reflection coefficient peak was retrieved. The monopole antenna resulted to be more influenced: the peak of the reflection coefficient shifted about 140 MHz, although return loss remained higher than 10 dB in the intended frequency band. Due to brevity, analysis of tri-port transmission coefficients is not included here, but it was observed that a small reduction in gain was obtained in the antennas, approximately 0.2 dB and 0.4 dB for the WPOA and WWDA antennas, respectively.

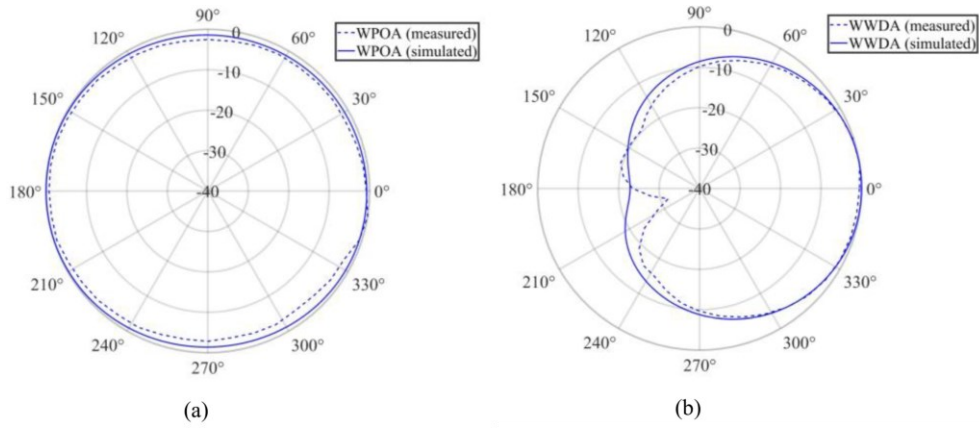
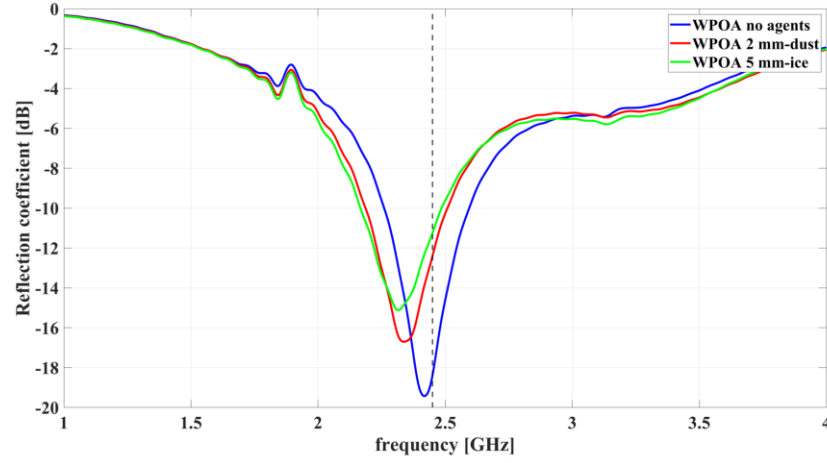
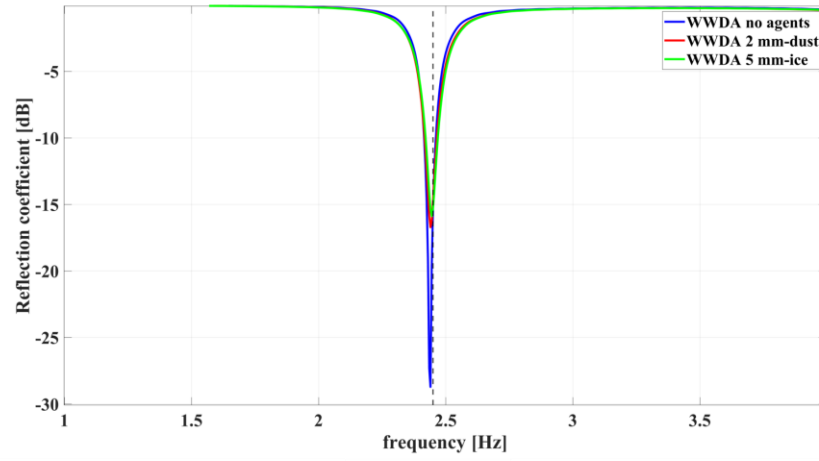


Fig. 54. Comparison between simulated and measured reflection parameters of the tri-port antenna system protected by the PLA-case. © 2024, IEEE

Measured normalized radiation patterns of the antennas in free space are shown for WPOA, Port 1, and WWDA, Port 2, in Fig. 54, together with simulated data. The maximum realized gain for the WPOA was 4.2 dBi at an elevation angle of 25° and for the WWDA it was 5.4 dBi in the broadside direction.



(a)



(b)

Fig. 55. Reflection coefficient of the monopole antenna and the patch antennas, whether there are dust or ice agents deposited on the surface of the case. © 2024, IEEE

This analysis assumes that the modular tri-antenna system in the plastic case will operate either when the dust settles on the device or when several millimeters of ice are formed during winter. Dust and fresh ice electrical properties employed in the simulations were retrieved from the literature [91, 92], where dust permittivity at  $2.45\text{ GHz}$  was  $4.4-j0.204$ , while for ice was  $3.31-j0.11$ . Simulations shown in Fig. 55 illustrate the system performance with and without dust or ice. The layer of dust was set to  $2\text{ mm}$ , while the ice layer was set to  $5\text{ mm}$  to create realistic conditions for outdoor deployment. The results show how the case minimizes

the performance degradation due to atmospheric factors. The return loss peak, in case of the omnidirectional antenna, shifted from  $2.42\text{ GHz}$  to  $2.37\text{ GHz}$  in the worst case, i.e., for a 5 mm ice layer, while maintaining good matching conditions (reflection coefficient of approximately  $-15\text{ dB}$  at  $2.45\text{ GHz}$ ). Patch antennas are more robust against perturbations due to impurities deposited on the casing surface. The frequency detuning is still relatively small, while the minimum reflection coefficient deteriorates significantly from  $-28\text{ dB}$  to  $-15\text{ dB}$  at the operational frequency of  $2.45\text{ GHz}$ . Similarly, as in the previous case, a study could be performed for the tri-port transmission coefficients too, but these are not presented here for conciseness. Regarding the gain performance, there is a slight reduction when the snow or ice layer increases in thickness. In the case of accumulation of 5 mm of ice, it can be seen by simulation that the main lobe gain is reduced of about  $0.52\text{ dB}$ , compared to situations when there was no weather-related build-up on the case of the antenna.

After the design and simulation phases, an experimental testing campaign was performed in the track Modena-Sassuolo by using the tri-port module for two networks: Network 1 for Wagon-to-Wagon and Network 2 for Type A Intelligent Pole-to-Train communication. The test setup considered the developed prototypes (equipped with LoRa modules) both as transmitter and receiver devices for both networks: one was used as an end-device and the other as Gateway for measuring the values of received signal strength indicator (RSSI) in various conditions of distance and environment.



Fig. 56. Positioning of the 2.45 GHz antenna module with PLA case outside the cockpit. © 2024, IEEE

Tests have been carried out on the railway track Modena-Sassuolo, in the section Modena-Formigine. The test train used in this study was the "Pop" model manufactured by Alstom Ferroviaria, an electric train composed of 3 wagons in a row for a length of about 75 meters. For the test of Network 1 link, during the first Modena-Formigine run, two prototypes (equipped with the PLA case) were installed outside the front and rear cockpits (Fig. 56) to simulate the worst case for a train integrity (3 wagons about 75 meters long). These devices were fed continuously with a DC power supply provided by the train.

The measurements showed the feasibility of this connection: in the 29-minute test, 276 packets were intercepted with an average RSSI of  $-69.1$  dBm, with only 3 lost packets.



The first return trip from Formigine to Modena was devoted to the test of communication between the wagons inside the compartments, even in the presence of passengers. Three different scenarios have been tested to ensure the integrity of the train: the first one involved the connection considering a distance of 3 wagons, with a time of measurement of 260 s for receiving 49 packets with an average RSSI of  $-84.8 \text{ dBm}$ . For this link 2 packets have been lost. Successively, a distance of 2 wagons have been considered, receiving 50 packets with an average RSSI of  $-77.2 \text{ dBm}$  in 198 s. Finally, the shorter distance of 1 wagon have been considered, with 51 detected packets with an average RSSI of  $-58.3 \text{ dBm}$  in 197 s.

The installation aimed at checking the Network 2 communication performance during the second Formigine-Modena trip tested the 2.45 GHz antenna module acting as a Gateway placed outside the front cockpit window, while the end-device equipped with the antennas was attached on a pole, at a height of 2 m from the ground at Baggiovara station. This configuration tested the capability of the train to exchange messages with an in-field type-A intelligent pole. The measurements confirmed successful reception of packets broadcast by the Gateway up to a distance of about 350 meters between the train's driving cab and the pole at the station. Minimum RSSI received while moving away and towards the station was  $-86 \text{ dBm}$ , while the average RSSI was recorded at  $-58.9 \text{ dBm}$  and  $-56.7 \text{ dBm}$ . All the measured results are listed in Table 4, considering the packet error rate (PER) and bit error rate (BER), computed as:

$$BER = 1 - (1 - PER^{1/n}) \quad (28)$$

where  $n$  is the number of bits per packet (192 in this case). Each packet includes a 4-byte payload and an overhead due to addressing (12 bytes), preamble, and LoRa synchronism. In this case (spreading factor: 12; bandwidth: 200 kHz; coding rate: 4/5), time on air for each packet resulted to be 690.64 ms. Moreover, in Table 4 the SNR values for the presented measurements are reported, considering a typical noise floor of  $-120 \text{ dBm}$  for the employed device (Semtech SX1280).

Table 4 © 2024, IEEE

<b>Communication Link</b>	<b>Antennas Position</b>	<b>Average RSSI (dBm)</b>	<b>SNR (dB)</b>	<b>PER</b>	<b>BER</b>
<b>Network 1 (3 wagons)</b>	Outside Train	− 69.1	50.9	0.0109	$5.69 \times 10^{-5}$
<b>Network 1 (3 wagons)</b>	Inside Train	− 84.8	35.2	0.0392	$2.08 \times 10^{-4}$
<b>Network 1 (2 wagons)</b>	Inside Train	−77.2	42.8	0	0
<b>Network 1 (1 wagons)</b>	Inside Train	−68.3	61.7	0	0

The entire journey was completely flat. The top speed went up to 59 *km/h*, and the average speed, considering only the parts where the train is in movement, was 21.8 *km/h*. Since three environments have been considered in this journey (urban, rural, and tunnel) Fig. 57 presents the RSSI values recorded across them during the first run with the antennas placed outside the train at a 3-wagon distance.

The performed measurements confirm that this solution represents an effective setup for train integrity, as it will stabilize the connection between wagons without significant data loss, regardless of the antenna module placement, inside or outside the train. Moreover, LoRa's range at 2.4 *GHz* will be enough to guarantee the communication for Network 2, between the train and intelligent poles, to keep the connection alive whenever pole spacing is 250 meters, in order to precisely localize a convoy within a secondary line and to preview the possibility of locating more trains along the same railway.

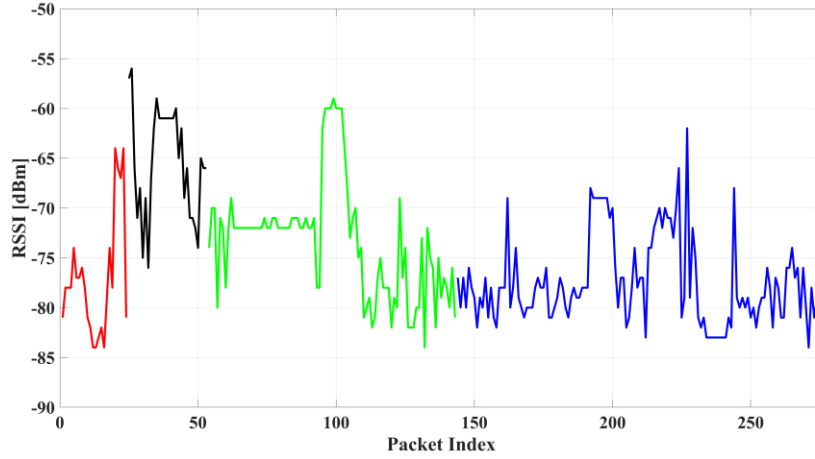


Fig. 57. Retrieved RSSI with respect to the different environments that have been crossed by the train, with the two modules placed outside it at a distance of about 75 m. © 2024, IEEE

This analysis illustrated the architecture of Network 1 for train Integrity and Network 2 for localization purposes. Such a modular system was developed and tested. It provides communication of every wagon with the first/last one and between the train and the intelligent poles up to 350 meters of distance.

# Conclusion

The activities described in this thesis have been dedicated to the conception, the theoretical and numerical design and the realization of novel RF wireless systems, to be exploited for WPT and localization applications.

In particular, chapter 2 and chapter 3 are related to the so-called smart radiating architectures, i.e, transmitters able to enhance the link efficiency, the bottleneck of the WPT efficiency, focusing the power without wasting it where it is not needed.

In chapter 2 the complete theory about FDAs has been developed, highlighting their basic radiation properties given by the multi-frequency excitation and proposing innovative designs that overcome the limitations of existing literature, which is often confined to theoretical aspects without addressing practical challenges. A deep investigation on its uniform linear configuration has been provided, bringing out the unique characteristic of a beam pattern function of the range, the angle and time variables. As a first contribution of this work, deep research on the topologies able to make the FDA feasible for powering applications have been provided, highlighting the 2D topologies involving circular symmetry as the best candidates for their improved beam spot dimension. In this sense, several architectures have been proposed, simulated and measured for the first time as the rectangular FDA, the CCFDA and the RFDA. Successively, the TCFDA, able to improve the accuracy of the FDA radiation exploiting the simplest linear array topology introducing RF switches, has been investigated for powering application for the first time. It has been demonstrated how this solution represents one of the best in terms of performance and cost, offering an accurate radiative system with an unseen, low-cost and easy-to-implement beam-steering capability. Additionally, through a measurement campaign, it has been demonstrated that the harmonic generation due to the time modulation of the RF signals can be favorably exploited for WPT applications by means of the dynamic control of the design parameters of the pulse and by setting its periodicity coincident with that one of the FDA radiation phenomena. Finally, an analytical and experimental characterization of the flexible beam steering capability of TCFDAs has been provided, demonstrating how the system can beam power in different directions simultaneously, with the possibility of creating, dynamically in real-time, single-

or multi-beam pattern, suitable for the smart energization of battery-less sensors, showing also that the high PAPR pulsed multi-tone powering signal results fruitful at the rectenna side.

In chapter 3, the TMAs have been investigated for their unique properties of creating multi-harmonic beampatterns that can be favorably exploited for powering and localization purposes. This section has tried to fill the gap of the literature, where most of the works related to TMAs regards optimization algorithms able to enhance the radiation properties of linear architectures made of isotropic radiators, proposing 2D topology that can be easily realized even if a high number of radiators is involved. It has been demonstrated that the arrangement of planar patch antennas in a radial layout allows to have highly-directive arrays that can be easily controlled by the time-modulation technique. Finally, despite the reduced number of controlling switches, which makes the proposed solution a feasible one, the high level of reconfigurability and precision is still guaranteed.

Successively, the same radial solution has been investigated for localization purposes: thanks to its circular symmetry, this radiator offers the interesting capability to behave in the same way by rotating it, and this is advantageous both when it is exploited for the first phase of localization and for the subsequent powering phase. In this context, two possible algorithms have been presented to validate the performance of the system: a monopulse-based algorithm, which relies on a single transmission, proved to be effective for real-time localization of moving targets, offering a very fast detection; then a scanning-based algorithm, which utilizes multiple steps in transmission, demonstrating superior accuracy by exploiting the full reconfigurability of the TMA and more robustness against interference issues. The numerical results have been validated by a measurement campaign that perfectly agrees with the theoretical analysis. Further research is needed to explore the multi-dimensional scanning capabilities of the array and to deal with the scattering from a real target.

In chapter 4 an analysis on the design and characterization of an innovative and low-cost architecture designed for equipped secondary railway lines based on the LoRa protocol for train signaling and positioning purposes has been presented. The overall architecture of Networks 1 and 2 have been presented, intended for train integrity and localization purposes, respectively, and a modular, compact system comprising of three different close antennas has been conceived and realized. This allows each wagon to communicate with the previous and

the following one(s), as well as to establish a connection between the train and the intelligent poles up to a distance of 350 m. Additionally, several weather conditions have been considered, and for this purpose, an ad-hoc case in plastic 3D printable material has been conceived and realized to protect the antenna module against harsh environmental conditions.

# References

- [1] <https://www.emergenresearch.com/industry-report/wireless-power-transmission-market>
- [2] A. Costanzo, D. Masotti, M. Fantuzzi and M. Del Prete, "Co-Design Strategies for Energy-Efficient UWB and UHF Wireless Systems," in IEEE Transactions on Microwave Theory and Techniques, vol. 65, no. 5, pp. 1852-1863, May 2017.
- [3] E. Kwiatkowski, J. A. Estrada, A. López-Yela and Z. Popović, "Broadband RF Energy-Harvesting Arrays," in Proceedings of the IEEE, vol. 110, no. 1, pp. 74-88, Jan. 2022.
- [4] A. Costanzo et al., "Energy Autonomous UWB Localization," in IEEE Journal of Radio Frequency Identification, vol. 1, no. 3, pp. 228-244, Sept. 2017.
- [5] A. Costanzo et al., "Electromagnetic Energy Harvesting and Wireless Power Transmission: A Unified Approach," in Proceedings of the IEEE, vol. 102, no. 11, pp. 1692-1711, Nov. 2014.
- [6] M. Thian, A. Barakat, and V. Fusco, "High-Efficiency Harmonic-Peaking Class-EF Power Amplifiers With Enhanced Maximum Operating Frequency," IEEE Transactions on Microwave Theory and Techniques, vol. 63, no. 2, pp. 659-671, Feb. 2015.
- [7] J. A. Estrada, J. R. Montejó-Garai, P. de Paco, D. Psychogiou and Z. Popović, "Power Amplifiers With Frequency-Selective Matching Networks," in IEEE Transactions on Microwave Theory and Techniques, vol. 69, no. 1, pp. 697-708, Jan. 2021.
- [8] C. Song et al., "Matching Network Elimination in Broadband Rectennas for High-Efficiency Wireless Power Transfer and Energy Harvesting," IEEE Transactions on Industrial Electronics, vol. 64, no. 5, pp. 3950-3961, May 2017.
- [9] E. L. Chuma, L. d. I. T. Rodríguez, Y. Iano, L. L. B. Roger and M. Sanchez-Soriano, "Compact rectenna based on a fractal geometry with a high conversion energy efficiency per area," IET Microwaves, Antennas & Propagation, vol. 12, no. 2, pp. 173-178, 7 2 2018.

- [10] Braun, Karl Ferdinand (1967) [Delivered 11 December 1909]. "Electrical Oscillations and Wireless Telegraphy". Nobel Lectures, Physics 1901-1921.
- [11] J. E. Stailey and K. D. Hondl, "Multifunction Phased Array Radar for Aircraft and Weather Surveillance," in Proceedings of the IEEE, vol. 104, no. 3, pp. 649-659, March 2016.
- [12] C. F. du Toit et al., "Smart multibeam phased array antenna for GSM, GPRS and EDGE," IEEE International Symposium on Phased Array Systems and Technology, 2003., Boston, MA, USA, 2003, pp. 146-151
- [13] Y. Li and V. Jandhyala, "Design of Retrodirective Antenna Arrays for Short-Range Wireless Power Transmission," in IEEE Transactions on Antennas and Propagation, vol. 60, no. 1, pp. 206-211, Jan. 2012.
- [14] R. Perez and N. K. Das, "Leaky Wave Radiation in a Linear Array of Capacitively Loaded Conducting Loops," in IEEE Transactions on Antennas and Propagation, vol. 63, no. 11, pp. 5093-5097, Nov. 2015.
- [15] W. H. Kummer, A. T. Villeneuve, T. S. Fong, F. G. Terrio, "Ultra-low sidelobes from time-modulated arrays," IEEE Trans. Antennas Propag., vol. AP-11, no. 6, pp. 633-639, Nov. 1963.
- [16] P. Antonik, M. C. Wicks, H. D. Griffiths, and C. J. Baker, "Frequency diverse array radars," in 2006 IEEE Conference on Radar, Verona, NY, USA, 2006, pp. 3 pp.-..
- [17] W. -Q. Wang and H. C. So, "Transmit Subaperturing for Range and Angle Estimation in Frequency Diverse Array Radar," IEEE Trans. Signal Process., vol. 62, no. 8, pp. 2000-2011, April 2014.
- [18] J. Xu, G. Liao, S. Zhu, L. Huang and H. C. So, "Joint Range and Angle Estimation Using MIMO Radar With Frequency Diverse Array," IEEE Trans. Signal Process., vol. 63, no. 13, pp. 3396-3410, July 2015.
- [19] S. Spinsante and C. Stallo, "Hybridized-GNSS Approaches to Train Positioning: Challenges and Open Issues on Uncertainty," Sensors, vol. 20, no. 7, p. 1885, Mar. 2020.
- [20] O. G. Crespillo et al., "Local GNSS Threat Detection Methods for Virtual Balise Placement in Railway Applications," 2018 16th International Conference on



- Intelligent Transportation Systems Telecommunications (ITST), Lisboa, Portugal, 2018, pp. 1-7.
- [21] P. Mayer, M. Magno, A. Berger, and L. Benini, "RTK-LoRa: High Precision, Long-Range, and Energy-Efficient Localization for Mobile IoT Devices," *IEEE Transactions on Instrumentation and Measurement*, vol. 70, pp. 1-11, 2021.
- [22] P. Antonik, M. C. Wicks, H. D. Griffiths and C. J. Baker, "Range-dependent beamforming using element level waveform diversity," *2006 International Waveform Diversity & Design Conference*, Lihue, HI, USA, 2006, pp. 1-6.
- [23] P. M. Corbell, M. A. Temple and T. B. Hale, "Forward-Looking Planar Array 3D-STAP using Space Time Illumination Patterns (STIP)," *Fourth IEEE Workshop on Sensor Array and Multichannel Processing, 2006.*, Waltham, MA, USA, 2006, pp. 602-606.
- [24] W. -Q. Wang, "Range-Angle Dependent Transmit Beampattern Synthesis for Linear Frequency Diverse Arrays," in *IEEE Transactions on Antennas and Propagation*, vol. 61, no. 8, pp. 4073-4081, Aug. 2013.
- [25] M. Secmen, S. Demir, A. Hizal and T. Eker, "Frequency Diverse Array Antenna with Periodic Time Modulated Pattern in Range and Angle," *2007 IEEE Radar Conference*, Waltham, MA, USA, 2007, pp. 427-430.
- [26] Jingjing Huang, Kin-Fai Tong and C. J. Baker, "Frequency diverse array with beam scanning feature," *2008 IEEE Antennas and Propagation Society International Symposium*, San Diego, CA, USA, 2008, pp. 1-4.
- [27] W. Khan, I. M. Qureshi and S. Saeed, "Frequency Diverse Array Radar With Logarithmically Increasing Frequency Offset," in *IEEE Antennas and Wireless Propagation Letters*, vol. 14, pp. 499-502, 2015.
- [28] H. Shao, J. Dai, J. Xiong, H. Chen and W. -Q. Wang, "Dot-Shaped Range-Angle Beampattern Synthesis for Frequency Diverse Array," in *IEEE Antennas and Wireless Propagation Letters*, vol. 15, pp. 1703-1706, 2016.
- [29] A. M. Jones and B. D. Rigling, "Planar frequency diverse array receiver architecture," *2012 IEEE Radar Conference*, Atlanta, GA, USA, 2012, pp. 0145-0150.

- [30] A. Akkoç, E. Afacan and E. Yazgan, "Investigation of Planar Frequency Diverse Array Antenna in Concentric Circular Geometry," *2019 11th International Conference on Electrical and Electronics Engineering (ELECO)*, Bursa, Turkey, 2019, pp. 651-654.
- [31] Y. Xu, X. Shi, J. Xu and P. Li, "Range-Angle-Dependent Beamforming of Pulsed Frequency Diverse Array," in *IEEE Transactions on Antennas and Propagation*, vol. 63, no. 7, pp. 3262-3267, July 2015.
- [32] A. -M. Yao, P. Rocca, W. Wu and A. Massa, "On the design of frequency diverse arrays for wireless power transmission," *2017 11th European Conference on Antennas and Propagation (EUCAP)*, Paris, France, 2017, pp. 900-903.
- [33] A. -M. Yao, N. Anselmi and P. Rocca, "A novel planar frequency diverse array design approach for far-field wireless power transmission," *2017 IEEE International Symposium on Antennas and Propagation & USNC/URSI National Radio Science Meeting*, San Diego, CA, USA, 2017, pp. 1807-1808.
- [34] D. Masotti, M. Shanawani and A. Costanzo, "Energy Focusing through Layout-based Frequency-Diverse Arrays," *2019 IEEE Wireless Power Transfer Conference (WPTC)*, London, UK, 2019, pp. 312-315.
- [35] Y. -S. Cui, H. Chen and W. -Q. Wang, "Frequency Diverse Array Focusing Beampattern Synthesis With Constrained Nonlinear Programming Frequency Offsets," *2019 27th European Signal Processing Conference (EUSIPCO)*, A Coruna, Spain, 2019, pp. 1-5.
- [36] X. Mengxuan et al., "Frequency Diverse Array Beampattern Synthesis with Joint Optimization of Frequency Offset and Carrier," *2022 International Conference on Microwave and Millimeter Wave Technology (ICMMT)*, Harbin, China, 2022, pp. 1-3.
- [37] T. Yuan, N. Yuan and L. -W. Li, "A Novel Series-Fed Taper Antenna Array Design," in *IEEE Antennas and Wireless Propagation Letters*, vol. 7, pp. 362-365, 2008.
- [38] S. Mohammad-Ali-Nezhad and A. Mallahzadeh, "Periodic Ridged Leaky-Wave Antenna Design Based on SIW Technology," in *IEEE Antennas and Wireless Propagation Letters*, vol. 14, pp. 354-357, 2015.

- [39] D. Masotti, A. Costanzo, P. Francia, M. Filippi, and A. Romani, "A load-modulated rectifier for RF micropower harvesting with start-up strategies," *IEEE Trans. Microw. Theory Tech.*, vol. 62, no. 4, pp. 994-1004, Apr. 2014.
- [40] M. Del Prete, A. Costanzo, M. Magno, D. Masotti and L. Benini, "Optimum excitations for a dual-band microwatt wake-up radio," *IEEE Trans. Microw. Theory Tech.*, vol. 64, no. 12, pp. 4731-4739, Dec. 2016.
- [41] D. Masotti, A. Costanzo, M. Del Prete and V. Rizzoli, "Time-Modulation of Linear Arrays for Real-Time Reconfigurable Wireless Power Transmission," *IEEE Trans. Microw. Theory Techn.*, vol. 64, no. 2, pp. 331-342, Feb. 2016.
- [42] A. -M. Yao, W. Wu and D. -G. Fang, "Single-Sideband Time-Modulated Phased Array," *IEEE Trans. Antennas and Propag.*, vol. 63, no. 5, pp. 1957-1968, May 2015.
- [43] N. Jastram and D. S. Filipovic, "Wideband multibeam millimeter wave arrays," in *2014 IEEE Antennas and Propagation Society International Symposium (APSURSI)*, Memphis, TN, USA, 2014, pp. 741-742.
- [44] A. Boaventura, D. Belo, R. Fernandes, A. Collado, A. Georgiadis and N. B. Carvalho, "Boosting the Efficiency: Unconventional Waveform Design for Efficient Wireless Power Transfer," in *IEEE Microwave Magazine*, vol. 16, no. 3, pp. 87-96, April 2015.
- [45] M. Pinuela, P. D. Mitcheson, and S. Lucyszyn, "Ambient RF energy harvesting in urban and semi-urban environments," *IEEE Trans. Microw. Theory Techn.*, vol. 61, no. 7, pp. 2715–2726, Jul. 2013.
- [46] D. Masotti, A. Costanzo, M. Del Prete, and V. Rizzoli, "A genetic-based design of a tetra-band high-efficiency RF energy harvesting system," *IET Microw. Antennas Propag.*, vol. 7, no. 15, pp. 1254–1263, 2013.
- [47] J. A. Hagerty, F. B. Helmbrecht, W. H. McCalpin, R. Zane, and Z.B. Popovic, "Recycling ambient microwave energy with broad-band rectenna arrays," *IEEE Trans. Microw. Theory Techn.*, vol. 52, no. 3, pp. 1014–1024, Mar. 2004.
- [48] A. Massa, G. Oliveri, F. Viani, and P. Rocca, "Array designs for long distance wireless power transmission: State-of-the-art and innovative solutions," *Proc. IEEE*, vol. 101, no. 6, pp. 1464–1481, Jun. 2013.

- [49] E. Hossain, M. Rasti, H. Tabassum, and A. Abdelnasser, "Evolution toward 5G multi-tier cellular wireless networks: An interference management perspective," *IEEE Wireless Commun.*, vol. 21, no. 3, pp. 118–127, Jun. 2014.
- [50] L. Roselli et al., "Smart surfaces: Large area electronics systems for Internet of Things enabled by energy harvesting," *Proc. IEEE*, vol. 102, no. 11, pp. 1723–1746, Nov. 2014.
- [51] M. M. Tentzeris et al., "Inkjet-printed 'zero-power' wireless sensor and power management nodes for IoT and "smart skin" applications," in 20th Int. MIKON Conf., Jun. 2014, pp. 1–7.
- [52] J. A. Hagerty, F. B. Helmbrecht, W. H. McCalpin, R. Zane, and Z. B. Popovic, "Recycling ambient microwave energy with broad-band rectenna arrays," *IEEE Trans. Microw. Theory Techn.*, vol. 52, no. 3, pp. 1014–1024, Mar. 2004.
- [53] A. Boaventura, D. Belo, R. Fernandes, A. Collado, A. Georgiadis, and N. B. Carvalho, "Boosting the efficiency: Unconventional waveform design for efficient wireless power transfer," *IEEE Microw. Mag.*, vol. 16, no. 3, pp. 87–96, Apr. 2015.
- [54] S. Yoshida, N. Hasegawa, and S. Kawasaki, "Experimental demonstration of microwave power transmission and wireless communication within a prototype reusable spacecraft," *IEEE Microw. Wireless Compon. Lett.*, vol. 25, no. 8, pp. 556–558, Aug. 2015.
- [55] A. Costanzo et al., "Electromagnetic energy harvesting and wireless power transmission: A unified approach," *Proc. IEEE*, vol. 102, no. 11, pp. 1692–1711, Nov. 2014.
- [56] H. E. Shanks and R. W. Bickmore, "Four dimensional electromagnetic radiators," *Canadian J. Phys.*, vol. 37, no. 3, pp. 263–275, 1959.
- [57] W. H. Kummer, A. T. Villeneuve, T. S. Fong, and F. G. Terrio, "Ultra-low sidelobes from time-modulated arrays," *IEEE Trans. Antennas Propag.*, vol. AP-11, no. 6, pp. 633–639, Nov. 1963.
- [58] S. Yang, Y. B. Gan, and A. Qing, "Sideband suppression in timemodulated linear arrays by the differential evolution algorithm," *IEEE Antennas Wireless Propag. Lett.*, vol. 1, no. 1, pp. 173–175, 2002.

- [59] G. Li, S. Yang, Y. Chen, and Z. Nie, "An adaptive beamforming in time modulated antenna arrays," in Proc. 8th Int. Symp. Antennas, Propag. EM Theory (ISAPE), Nov. 2008, pp. 166–169.
- [60] L. Poli, P. Rocca, G. Oliveri, and A. Massa, "Harmonic beamforming in time-modulated linear arrays through particle swarm optimization," IEEE Trans. Antennas Propag., vol. 59, no. 7, pp. 2538–2545, Jul. 2011.
- [61] A. Tennante and B. Chambers, "A two-element time-modulated array with direction-finding properties," IEEE Antennas Wireless Propag. Lett., vol. 6, pp. 64–65, 2007.
- [62] G. Li, S. Yang, and Z. Nie, "Direction of arrival estimation in time modulated antenna arrays with unidirectional phase center motion," IEEE Trans. Antennas Propag., vol. 58, no. 4, pp. 1105–1111, Apr. 2010.
- [63] L. Poli, P. Rocca, G. Oliveri, and E. A. Massa, "Adaptive nulling in time modulated linear arrays with minimum power losses," IET Microw., Antennas Propag., vol. 5, no. 2, pp. 157–166, 2011.
- [64] Y. Chen, S. Yang, G. Li, and Z. Nie, "Adaptive nulling with timemodulated antenna arrays using a hybrid differential evolution strategy," Electromagnetics, vol. 30, no. 7, pp. 574–588, Sept. 2010.
- [65] Y. Tong and A. Tennant, "Simultaneous control of sidelobe level and harmonic beam steering in time-modulated linear arrays," Electron. Lett., vol. 46, no. 3, pp. 201–202, Feb. 2010.
- [66] G. Li, S. Yang, Y. Chen, and Z. Nie, "A novel electronic beam steering technique time modulated antenna arrays," Progr. Electromag. Res., vol. 97, pp. 391–405, 2009.
- [67] W. H. Kummer, A. T. Villeneuve, T. S. Fong, and F. G. Terrio, "Ultra-low sidelobes from time-modulated arrays," IEEE Trans. Antennas Propag., vol. AP-11, no. 6, pp. 633–639, Nov. 1963.
- [68] S. Yang, Y. B. Gan, A. Qing, and P. K. Tan, "Design of a uniform amplitude time-modulated linear array with optimized time sequences," IEEE Trans. Antennas Propag., vol. 53, no. 7, pp. 2337–2339, Jul. 2005.

- [69] L. Poli, P. Rocca, L. Manica, and A. Massa, "Pattern synthesis in time-modulated linear arrays through pulse shifting," *IET Microw., Antennas Propag.*, vol. 4, no. 9, pp. 1157–1164, Sep. 2010.
- [70] Q. Zhu, S. Yang, L. Zheng, and Z. Nie, "Design of a low sidelobe time modulated linear array with uniform amplitude and sub-sectional optimized time steps," *IEEE Trans. Antennas Propag.*, vol. 60, no. 9, pp. 4436–4439, Sep. 2012.
- [71] J. Fondevila, J. C. Brégains, F. Ares, and E. Moreno, "Optimizing uniformly excited linear arrays through time modulation," *IEEE Antennas Wireless Propag. Lett.*, vol. 3, no. 1, pp. 298–301, 2004.
- [72] D. Masotti, A. Costanzo, M. Del Prete and V. Rizzoli, "Time-Modulation of Linear Arrays for Real-Time Reconfigurable Wireless Power Transmission", *IEEE Trans. Microw. Theory Techn.*, vol. 64, no. 2, pp. 331-342, Feb. 2016.
- [73] Q. Chen, J. -D. Zhang, W. Wu and D. -G. Fang, "Enhanced Single-Sideband Time-Modulated Phased Array With Lower Sideband Level and Loss," in *IEEE Transactions on Antennas and Propagation*, vol. 68, no. 1, pp. 275-286, Jan. 2020.
- [74] D. Masotti, L. Poli, M. Salucci, P. Rocca and A. Costanzo, "An Effective Procedure for Nonlinear Dynamic Optimization of Time-Modulated Arrays," *IEEE Antennas Wirel. Propag. Lett.*, vol. 18, no. 10, pp. 2204-2208, Oct. 2019.
- [75] D. Masotti, A. Costanzo, M. Del Prete and V. Rizzoli, "Time-Modulation of Linear Arrays for Real-Time Reconfigurable Wireless Power Transmission", *IEEE Trans. Microw. Theory Techn.*, vol. 64, no. 2, pp. 331-342, Feb. 2016.
- [76] O. G. Crespillo et al., "Local GNSS threat detection methods for virtual balise placement in railway applications," in *Proc. 16th ITST*, 2018, pp. 1–7.
- [77] J. Mendizabal, J. Goya, G. De Miguel, L. Valdivia, S. Arrizabalaga, and I. Adin, "Virtual testing of the on-board ETCS with GNSS based Train integrity determination," in *Proc. 15th ITST*, 2017, pp. 1–7.
- [78] S. Oh, Y. Yoon, K. Kim, and Y. Kim, "Design of train integrity monitoring system for radio based train control system," in *Proc. 12<sup>th</sup> ICCAS*, Jeju, South Korea, 2012, pp. 1237–1240.

- [79] J. Liu, B. Cai, D. Lu, and J. Wang, “Integrity of GNSS-based Train Positioning: From GNSS to sensor integration,” in *Proc. ENC*, 2017, pp. 48–56.
- [80] S. Spinsante and C. Stallo, “Hybridized-GNSS approaches to train positioning: Challenges and open issues on uncertainty,” *Sensors*, vol. 20, no. 7, p. 1885, Mar. 2020, doi: 10.3390/s20071885.
- [81] D. Mikhaylov et al., “Toward the future generation of railway localization exploiting RTK and GNSS,” *IEEE Trans. Instrum. Meas.*, vol. 72, pp. 1–10, May 2023, doi: 10.1109/TIM.2023.3272048.
- [82] A. Schütz, D. E. Sánchez-Morales, and T. Pany, “Precise positioning through a loosely-coupled sensor fusion of GNSS-RTK, INS and LiDAR for autonomous driving,” in *Proc. IEEE/ION PLANS*, 2020, pp. 219–225.
- [83] Y. Zhou, Q. Chen, and X. Niu, “Kinematic Measurement of the Railway Track Centerline Position by GNSS/INS/Odometer Integration,” *IEEE Access*, vol. 7, pp. 157241–157253, 2019.
- [84] G. Y. Li, S. Han, L. Yang, F.-Y. Wang, and H. Zhang, “LoRa on the move: Performance evaluation of LoRa in V2X communications,” in *Proc. IEEE IV Symp.*, 2018, pp. 1107–1111.
- [85] K. F. Haque, A. Abdelgawad, V. P. Yanambaka, and K. Yelamarthi, “A LoRa based reliable and low power vehicle to everything (V2X) communication architecture,” in *Proc. IEEE iSES*, Chennai, India, 2020, pp. 177–182.
- [86] J. Soares, M. Luís, and S. Sargento, “Mobile LoRa gateway for communication and sensing on the railway,” in *Proc. IEEE ISCC*, Gammarth, Tunisia, 2023, pp. 499–502.
- [87] P. A. Torres, C. B. D. Silva, and H. T. Filho, “An experimental study on the use of LoRa technology in vehicle communication,” *IEEE Access*, vol. 9, pp. 26633–26640, 2021, doi: 10.1109/ACCESS.2021.3057602.
- [88] J. Gozalvez, M. Sepulcre, and R. Bauza, “IEEE 802.11p vehicle to infrastructure communications in urban environments,” *IEEE Commun. Mag.*, vol. 50, no. 5, pp. 176–183, May 2012.

- [89] D. Bri, M. Fernandez-Diego, M. Garcia, F. Ramos, and J. Lloret, “How the weather impacts on the performance of an outdoor WLAN,” *IEEE Commun. Lett.*, vol. 16, no. 8, pp. 1184–1187, Aug. 2012.
- [90] P. Mayer, M. Magno, A. Berger, and L. Benini, “RTK-LoRa: High-Precision, long-range, and energy-efficient localization for mobile IoT devices,” *IEEE Trans. Instrum. Meas.*, vol. 70, pp. 1–11, 2021.
- [91] X.-Y. Dong, H.-Y. Chen, and D.-H. Guo, “Microwave and millimeter-wave attenuation in sand and dust storms,” *IEEE Antennas Wireless Propag. Lett.*, vol. 10, pp. 469–471, 2011.
- [92] A. M. Semmling et al., “Sea-ice permittivity derived from GNSS reflection profiles: Results of the MOSAiC expedition,” *IEEE Trans. Geosci. Remote Sens. Mag.*, vol. 60.